Application of the authigenic 10Be/9Be dating to constrain the age of a long-lived lake and its regression in an isolated intermontane basin: The case of Late Miocene Lake Turiec, Western Carpathians

Michal Šujan, Kishan Aherwar, Rastislav Vojtko, Régis Braucher, Katarína Šarinová, Andrej Chyba, Jozef Hók, Anita Grizelj, Radovan Pipík, Bronislava Lalinská-Voleková, et al.

Global and Planetary Change

Long-lived lake and its regression in an isolated intermontane basin dated by authigenic 10Be/9Be: The Late Miocene Lake Turiec in the Western Carpathians

--Manuscript Draft--

Manuscript Number:	GLOPLACHA-D-22-00680
Article Type:	Research paper
Keywords:	cosmogenic nuclides; authigenic 10Be/9Be dating; facies analysis; lake regression; Western Carpathians; paleoenvironment; endorheic basin
Corresponding Author:	Michal Šujan Comenius University SLOVAKIA
First Author:	Michal Šujan
Order of Authors:	Michal Šujan
	Kishan Aherwar
	Rastislav Vojtko
	Régis Braucher
	Katarína Šarinová
	Andrej Chyba
	Jozef Hók
	Anita Grizelj
	Radovan Pipík
	Bronislava Lalinská - Voleková
	Barbara Rózsová
	Aster Team
Abstract:	The depositional record of intermontane basins provides a valuable archive of the temporal evolution of orogenic belts; their common isolated nature, however, hinders the efficient usage of standard approaches to constrain the age of a basin fill. In this paper the authigenic 10Be/9Be dating method is employed to construct an age model of the existence and regression of Lake Turiec, which appeared during the Late Miocene in the intermontane Turiec Basin, Central Western Carpathians (Central Europe). The sedimentological analysis of outcrops allowed the definition of the facies associations of an alluvial fan, a braided river, a fan delta and an open lake. The distribution of facies associations in the basin fill implies an increase in sediment supply due to the replacement of the open lake environment by the interconnected alluvial fan-braided river-fan delta system. Authigenic 10Be/9Be dating yielded ages of the lacustrine succession reaching ~10.0–8.2 Ma, while the age of the fan delta succession, considered as the timing of the regression, was established to ~6.7 Ma. The deposition of alluvial fans dominated the basin after the regression of the lake, possibly up to ~4.0 Ma. The abrupt increase in sediment supply to the accommodation ratio at ~6.7 Ma was caused by the uplift of the Malá Fatra Mts. at the western margin of the Turiec Basin, which had previously formed a moderate topography. The timing of this process generally coincides with the overall decrease in accommodation rates in the region due to the inversion of the Pannonian Basin System. The endorheic character of the basin before ~6.7 Ma prevented the transport of the sediment denudated from the recently most uplifted parts of the Western Carpathians and carried towards the Pannonian Basin System, while the present-day source-to-sink system could only be formed later. This implies a low sediment supply and restricted denudation rate not only from the morphostructures surrounding the basin, but also from the Tatra Mts. and Nízke Tatry Mts. during the period ~10.0–6.7 Ma. The study involves the analysis of several sites for a determination of the initial authigenic 10Be/9Be ratio, and the selection of the relevant one is based on sedimentological and

Highlights:

- Authigenic $^{10}Be/^{9}Be$ dating resolve history of a long-lived isolated late Miocene lake
- Initial $^{10}Be/^{9}Be$ selected based on validation of paleoenvironmental conditions
- Lake Turiec existed between 10.0–6.7 Ma, then filled by a fan delta-braided river-alluvial fan depositional system
- Regression due to increased sediment supply from mountains uplifting after 7 Ma
- Termination of endorheic character and establishment of the Váh river catchment followed

Long-lived lake and its regression in an isolated intermontane basin dated by authigenic $^{10}Be/^{9}Be$: The Late Miocene Lake Turiec in the Western Carpathians

Michal Šujan[1,*], Kishan Aherwar[1], Rastislav Vojtko[1], Régis Braucher[2], Katarína Šarinová[3], Andrej Chyba[4], Jozef Hók[1], Anita Grizelj[5], Radovan Pipík[6], Bronislava Lalinská - Voleková[7], Barbara Rózsová[1], Aster Team[2]**

1 – Department of Geology and Paleontology, Faculty of Natural Sciences, Comenius University in Bratislava, Ilkovičova 6, 842 15 Bratislava, Slovakia; michal.sujan@uniba.sk

2 – CNRS-IRD-Collège de France-INRAE, CEREGE, Aix-Marseille Univ., 13545 Aix-en-Provence, France; braucher@cerege.fr

3 – Department of Mineralogy, Petrology and Economic Geology, Faculty of Natural Sciences, Comenius University in Bratislava, Ilkovičova 6, 842 15 Bratislava, Slovakia; katarina.sarinova@uniba.sk

4 – Institute of Chemistry, Slovak Academy of Sciences, Dúbravská cesta 9, 845 38 Bratislava, Slovakia; andrej.chyba@savba.sk

5 – Croatian Geological Survey, Sachsova 2, 10 000 Zagreb, Croatia; agrizelj@hgi-cgs.hr

6 – Earth Science Institute, Slovak Academy of Sciences, Ďumbierska 1, 97411 Banská Bystrica, Slovakia; pipik@savbb.sk

7 – SNM-Natural History Museum, Vajanského náb. 2, P.O. BOX 13, 810 06 Bratislava, Slovakia; bronislavalalinska@gmail.com

* – corresponding author

** – AsterTeam: Georges Aumaître, Karim Keddadouche, Fawzi Zaidi

Abstract

The depositional record of intermontane basins provides a valuable archive of the temporal evolution of orogenic belts; their common isolated nature, however, hinders the efficient usage of standard approaches to constrain the age of a basin fill. In this paper the authigenic $^{10}Be/^{9}Be$ dating method is employed to construct an age model of the existence and regression of Lake Turiec, which appeared during the Late Miocene in the intermontane Turiec Basin, Central Western Carpathians (Central Europe). The sedimentological analysis of outcrops allowed the definition of the facies associations of an alluvial fan, a braided river, a fan delta and an open lake. The distribution of facies associations in the basin fill implies an increase in sediment supply due to the replacement of the open lake environment by the interconnected alluvial fan-braided river-fan delta system. Authigenic $^{10}Be/^{9}Be$ dating yielded ages of the lacustrine succession reaching ~10.0–8.2 Ma, while the age of the fan delta succession, considered as the timing of the regression, was established to ~6.7 Ma. The deposition of alluvial fans dominated the basin after the regression of the lake, possibly up to ~4.0 Ma. The abrupt increase in sediment supply to the accommodation ratio at ~6.7 Ma was caused by the uplift of the Malá Fatra Mts. at the western margin of the Turiec Basin, which had previously formed a moderate topography. The timing of this process generally coincides with the overall decrease in accommodation rates in the region due to the inversion of the Pannonian Basin System. The endorheic character of the basin before ~6.7 Ma prevented the transport of the sediment denudated from the recently most uplifted parts of the Western Carpathians and carried towards the Pannonian Basin System, while the present-day source-to-sink system could only be formed later. This implies a low sediment supply and restricted denudation rate not only from the morphostructures surrounding the basin, but also from the Tatra Mts. and Nízke Tatry Mts. during the period ~10.0–6.7 Ma. The study involves the analysis of several sites for a determination of the initial authigenic $^{10}Be/^{9}Be$ ratio, and the selection of the relevant one is

based on sedimentological and geochemical evaluation. The research supports the suitability of intermontane basins for authigenic $^{10}Be/^{9}Be$ dating in a setting of high accommodation rates and limited redeposition of older material.

Keywords: cosmogenic nuclides, authigenic $^{10}Be/^{9}Be$ dating, facies analysis, lake regression, Western Carpathians, paleoenvironment

1. Introduction

Intermontane basins comprise an essential part of the structure of orogenic belts worldwide (e.g., Burbank, 1983; Gibling et al., 1985; Chaimov et al., 1992; Streit et al., 2017; Paknia et al., 2021). Their formation mirrors changes in the geodynamic phases of orogenic belts, which are recorded by the lithology and geometry of the resulting sedimentary fill of the basins. The analysis of such basin fill is therefore potentially the source of a wealth of information for geodynamic, paleogeographic and morphotectonic studies.

A position in the interior of an orogen may lead to the establishment of an endorheic drainage pattern and a decrease in precipitation caused by orographic rainfall barriers (Sobel et al., 2003; Trexler et al., 2012). Hence, the connectivity of an intermontane basin with a drainage network of the orogenic belt and foreland plays an important role in regional paleoclimatic settings. Another major factor related to the role of an intermontane basin in the drainage network of an orogenic belt is the redistribution of sediment and its transient storage. The depositional record of such a basin provides a valuable archive of changes in the drainage of rivers, which in turn affects the switching of provenance in the more distal settings of foredeep and back-arc basins. Moreover, the connectivity of an intermontane basin with the regional drainage network exerts a control factor of the first-order over its accommodation rates, since endorheic periods cause increased sediment storage due to the local base-level rise, while the re-establishment of connectivity is followed by incision and sediment removal (Schildgen et al., 2016; Geurts et

al., 2018; Ballato et al., 2019; Paknia et al., 2021). The variation in base-level and the related thickness of basin fill induces shallow crustal stresses by loading and unloading, further making the resulting pattern of accumulation more complex (Ballato et al., 2019).

Nevertheless, a position within an orogenic belt commonly leads to the isolation of water bodies formed in intermontane basins from the world's oceans, indeed, frequently even from basins in adjacent regions. The freshwater, brackish and occasionally endemic character of the biota complicates the chronostratigraphic constraint of deposition via the use of biostratigraphy (Harzhauser and Mandic, 2008; Pipík et al., 2012; Magyar, 2021). The frequent presence of hiatuses related to base-level changes may obscure the interpretation of magnetostratigraphic records (Langereis et al., 2010).

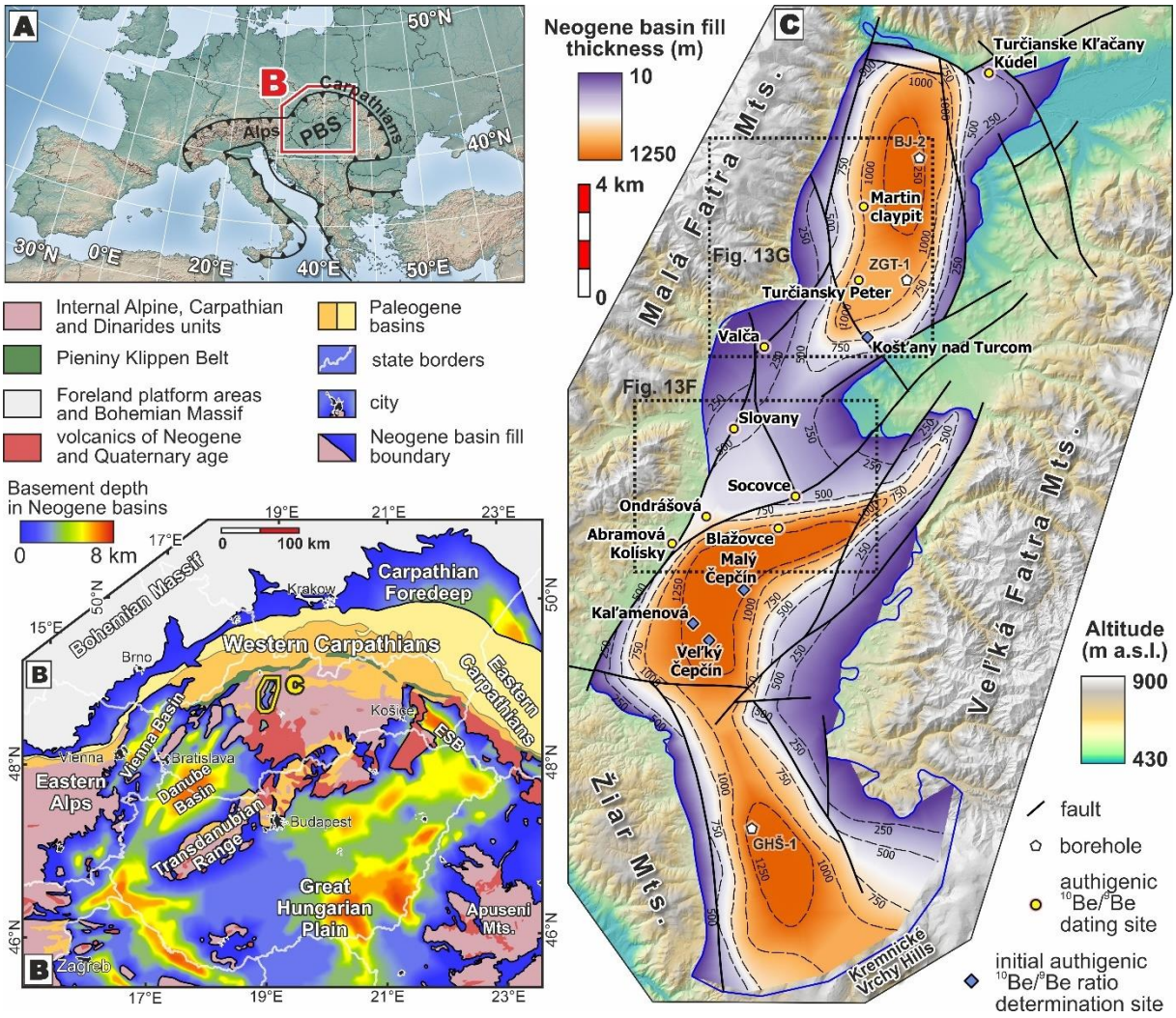

Fig. 1. Location of the Turiec Basin. A: Location within the Alpine-Carpathian orogen in Central Europe. B: The Turiec Basin in the Central Western Carpathians. The map is modified from Šujan et al. (2021b). C: Location of the studied sites of the Turiec Basin together with the thickness of the Neogene basin fill and Lidar DEM topography of the mountains surrounding the basin. Isobaths based on Zbořil et al. (1985). The Lidar DEM data were provided by the Geodesy, Cartography and Cadaster Authority of the Slovak Republic.

This study provides the first geochronological proxies for the fill of the intermontane Turiec Basin in the Western Carpathians (Fig. 1A, B) intending to constrain the existence of long-lived Lake Turiec. Despite the lacustrine deposition of long duration, forming a muddy succession up to 900 m thick, the specific history of this basin in the heart of the Western Carpathians was a puzzle due to the missing geochronological proxies (Kováč et al., 2011). The integration of authigenic $^{10}Be/^{9}Be$ dating, the facies analysis of outcrops, geochemistry and basin analysis shed light on the timing of the existence and regression of the lake, as well as its geodynamic context. Moreover, this study intends to test the applicability of the authigenic $^{10}Be/^{9}Be$ dating method in the conditions of an intermontane basin. A complex approach to the verification of the initial $^{10}Be/^{9}Be$ ratio aims to improve the method's applicability in the interest of its future utilization in comparable settings.

2. Geological setting

2.1 Structure of the intermontane Turiec Basin

The Turiec Basin is located within the Central Western Carpathians (CWC) in Central Europe (Fig. 1A, B). The Western Carpathian mountain range comprises the northernmost segment of the European Alpides (Schmid et al., 2008). Its central part experienced thick- and thin-skinned thrusting in Late Jurassic and Cretaceous times, while the continuously propagating orogen underwent the thrusting and collision of its external zones with the North European Platform until the Late Miocene (Hók et al., 2014; Plašienka, 2018). The Paleogene evolution of the

CWC was determined by the Paleocene-Middle Eocene exhumation and the Late Eocene to Oligocene existence of the fore-arc type Central Carpathian Paleogene Basin (CCPB) (Králiková et al., 2014a; Kováč et al., 2016). Another phase of exhumation and partial denudation of the Paleogene successions followed in the earliest part of the Early Miocene (Aquitanian) (Králiková et al., 2014a; Kováč et al., 2017b). The first transgression of the Central Paratethys Sea towards the CWC appeared in Early-Middle Miocene times (Kováč et al., 2017a; Kováč et al., 2017b), while its specific timing is a matter of ongoing debate and may well prove to be time-transgressive (Kováč et al., 2018). The Miocene areal volcanism in the CWC was associated with the formation of the Central Slovakia–Northern Hungary Volcanic Field (SHVF; Konečný et al., 2002; Pécskay et al., 2006). The crustal stretching due to the upwelling asthenospheric mantle and the activity of the Central Slovak Fault System (CSF) during the Middle-Late Miocene has been considered a cause of the formation of the basin-and-range structure of the CWC (Nemčok and Lexa, 1990; Kováč and Hók, 1993). This process led to the formation of intermontane basins, one of which is the Turiec Basin (Kováč et al., 2011; Pulišová and Hók, 2015; Wysocka et al., 2018).

The Turiec Basin comprises a half-graben, oriented north-south, ca. 40 km long and 10 km wide, and dipping westwards, where it is bounded by the Neogene horsts of the Žiar and Malá Fatra Mts. (Fig. 1C). The Veľká Fatra Mts. form the eastern margin and the Middle Miocene volcanic Kremnické Vrchy Hills (a part of the SHVF) limit the southern portion of the basin. These horsts, as well as the basement of the basin, are composed of the paleo-Alpine nappe stack, including a Variscan crystalline basement and Mesozoic, mostly carbonatic sedimentary cover of the Tatric Unit, overlaid by the Fatric Unit, comprising Triassic to Lower Cretaceous sequences, and by the Hronic nappe system of predominantly Triassic sequences (Plašienka et al., 1997; Plašienka, 2003; Froitzheim et al., 2008; Havrila, 2011). The nappe structure is sealed

by the flysch-type Paleogene sediments, which represent erosive remnants of the CCPB cropping out on the eastern and southern margins of the basin.

The late Cenozoic fill of the Turiec Basin reaches an overall thickness of up to 1250 m (Zbořil et al., 1985; Kilényi and Šefara, 1991) (Fig. 1C). It is present in two main depocenters to the north (boreholes BJ-2 and ZGT-3) and south (borehole GHŠ-1) (Gašparik, 1972; Fendek et al., 1990; Bielik et al., 2013) (Fig. 1C). The lithostratigraphy of the Miocene basin, according to Kováč et al. (2011) and taking into consideration the refinements made in this paper, is depicted on Fig. 2. The volcano-sedimentary andesite complex of the Turček Formation appears in the southern portion of the basin and consists of andesite lava flows, tuffs, tuffite layers, and clays with a tuff admixture. It has been considered to belong to of the Late Badenian (Serravallian) or Pannonian (Tortonian) ages (Konečný et al., 1983; Konečný et al., 1995; Chernyshev et al., 2013; Králiková et al., 2014a). The Turček Formation is overlaid by the Budiš Member, which has a suggested age of lates Middle Miocene to early Late Miocene. It comprises sediments of alluvial fans, with deposition dominated by subaerial gravity flows, and is present only in the southern portion of the basin (Kováč et al., 2011).

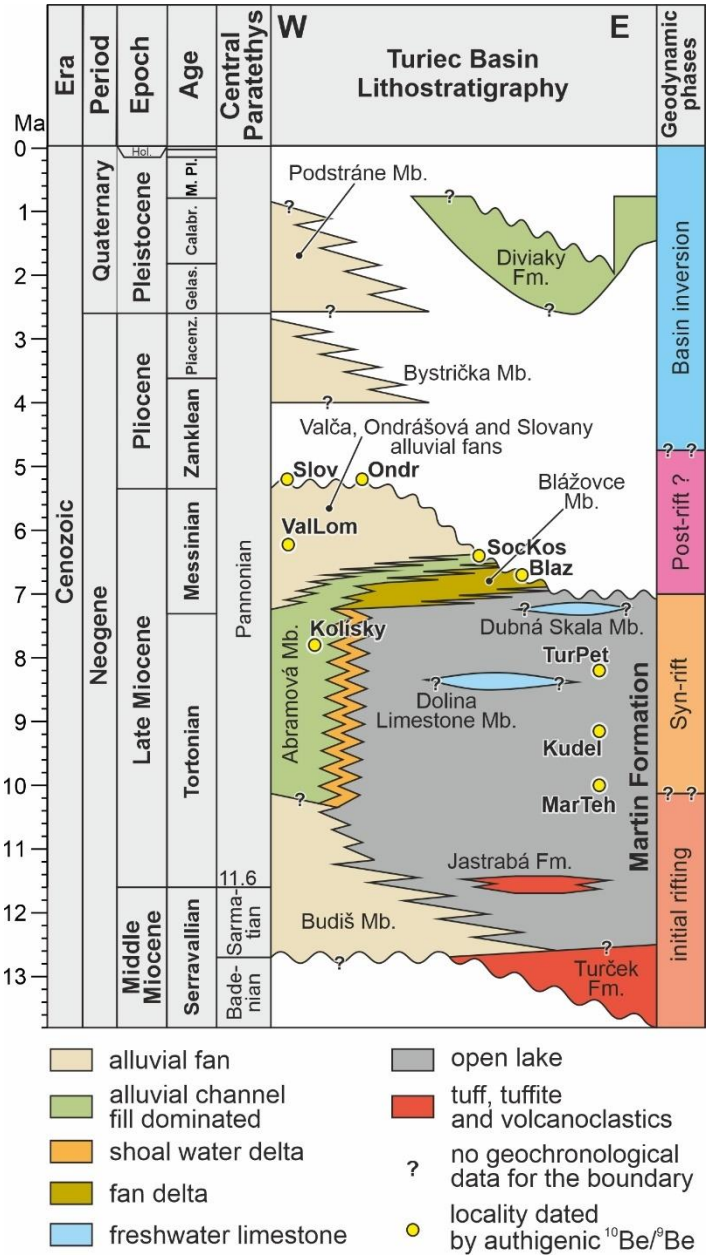

147

148 Fig. 2. Lithostratigraphic scheme of the Turiec Basin according to Kováč et al.
149 (2011) and the refinements presented in this study. The stratigraphic position of the
150 studied sites is shown.

151 The Budiš Member intercalates with the open lacustrine Martin Formation (Fig. 2), with
152 deposition in the long-lived Lake Turiec likely started in the late Middle Miocene (Serravallian)
153 and appeared mostly during the Late Miocene (Tortonian to Messinian) (Pipík, 2002; Kováč et
154 al., 2011; Pipík et al., 2012). The Martin Formation comprises a major part of the syn-rift basin
155 fill reaching a thickness of up to 900 m, and consists predominantly of open lacustrine muds

156 with intercalations of clastics deposited by storm or gravity currents. The diverse shallow to
157 deeper offshore-type nature of the paleolake is implied by the frequent occurrence of coal
158 seams, water plants and plant detritus, by mollusk and ostracod fauna, as well as by the presence
159 of freshwater limestone beds (Fendek et al., 1990; Kováč et al., 2011). The lowermost part of
160 the Martin Formation intercalates with tuffs and tuffites of the Jastrabá Formation, which has
161 been dated to 12.2–11.4 Ma – around the Middle and Late Miocene boundary (Lexa et al., 1998;
162 Chernyshev et al., 2013). The Turčok and Jastrabá fms., together with the Budiš Mb., are
163 considered deposits laid down/deposited in the basin's initial rifting stage (Kováč et al., 2011).

164 The Martin Formation intercalates with the Abramová Member towards the subaerially exposed
165 southwestern margin of the basin (Fig. 2). It includes gravels of subaerial gravity currents and
166 traction currents in shallow channels, sandy beds, as well as muddy overbank deposits. The
167 clast material is derived solely from the Triassic carbonates of the Hronic Unit. The Abramová
168 Member's depositional environment coexisted for an unknown period with the lacustrine
169 environment of Lake Turiec. The Martin Formation also intercalates with the freshwater
170 limestones of the Dolina Limestone and Dubná Skala members (Kováč et al., 2011).

171 The subsequent regression of Lake Turiec is marked by a significant decrease in
172 accommodation rate to sediment supply ratio, which caused the occurrence of newly formed
173 depositional systems of fan deltas and alluvial fans (Fig. 2). These were previously included in
174 a single lithostratigraphic unit of the Blažovce Member (Kováč et al., 2011); however, the
175 observed stratigraphy implies that the riverine environment of the Abramová Member formed
176 a feeder system, transporting material from alluvial fans to fan deltas. The alluvial fans include
177 mostly gravels, intercalations of sands and fine sandy muds of subaerial gravity flow origin.
178 Fan deltas exhibit much more complicated stratigraphy, with a wide range of depositional
179 processes, including subaerial and subaquatic gravity flows, channelized traction currents and

low-density turbidity currents. The clast material is again dominated by the carbonates of the Hronic Unit (Kováč et al., 2011).

The Late Miocene sedimentary fill described here generally represents a complete cycle of tectonic sequence *sensu* Matenco and Haq (2020). It is overlain discordantly by the alluvial fans of the Bystrička Member of a supposed Late Pliocene age, and by the Early Pleistocene Podstráne Member and the Diviaky Formation. The mentioned lithostratigraphic units differ from the fill of the older basin in having a more varied petrographic composition of clasts, including younger Mesozoic lithotypes and rocks derived from the crystalline basement (Buday, 1962; Minár and Bizubová, 1994; Kováč et al., 2011).

The central zones of the mountains surrounding the Turiec Basin include a planation surface, which appears at altitudes from ca. 1500 m a.s.l. (Malá and Veľká Fatra Mts.) to 700 m a.s.l. (Žiar Mts.) (Lukniš, 1962). This surface, originally called the "Mid-Mountain level", was until recently considered a tectoplain (Mazúr, 1963; Minár, 2003); and one might expect it to have been formed concurrently with the fine-grained sedimentation of the Tortonian Martin Formation (Kováč et al., 2011; Minár et al., 2011). The basin fill is deformed by a network of faults with normal to transtensional kinematics, and the faults were active during and/or after the Late Miocene depositional cycle associated with the existence of Lake Turiec (Zbořil et al., 1985; Kováč et al., 2011) (Fig. 1C).

2.2 Paleoenvironments of Lake Turiec

The isolation of long-lived Lake Turiec led to the development of rich endemic ostracod fauna, which has been extensively studied in past decades. An overview of the spatial distribution of various fossil associations allows us to specify the paleoenvironmental conditions of the paleolake.

The earliest existence of a lacustrine environment in the Turiec Basin can be dated to the late Middle Miocene, as may be inferred from the rare ostracod valves of freshwater *Darwinula stevensoni*, *Candona*, *Cypria* and the brackish *Mediocypris* and *Leptocythere* (Kováč et al., 2011). After what was probably a short-lived connection between Lake Turiec with Lake Pannon in the early Late Miocene disappeared, the basin became a freshwater neutral to alkaline lake (Ognjanova-Rumenova and Pipík, 2015). Abundant and diverse endemic fauna and flora from the Upper Miocene beds (Márton et al., 2022), such as pollens, macroflora, ostracods, gastropods, bivalves, fish otoliths, and sponges of the family *Spongillidae*, document a geographically and biologically well-structured terrestrial and aquatic ecosystem and testify to the long-term isolation of the former Lake Turiec. This long isolation led to the evolution of endemic ostracod species, which display a gradual evolution from simple and smooth elongated to variable and ornamented valves; it also permits the relative stratigraphic correlation and reconstruction of paleoecological evolution of the freshwater Turiec Basin fill (Pipík et al., 2012).

The bathymetric differentiation of the freshwater Lake Turiec is possible due to the ostracod fauna. Shallow environments classified as littoral prevailed in the north, while the central and southern parts of the basin were dominated by a deep-water zone. The hydrological regime can be defined by the main input of water from the north, by the river(s) carrying mostly fine-grained clayey sediment (Kováč et al., 2011).

The shallow lacustrine and littoral deposits of the Martin Formation, which occupy the entire northern part of the basin and isolated patches on the east and south-west basin margins, display a broad diversity of ecological conditions and biotope richness (Pipík, 2002; Pipík, 2004; Pipík, 2005). The shallow lacustrine environments in the northern depocenter included marshes with slowly flowing water (ostracod *Ilyocypris*) covered by water plants (*Nelumbium*, *Potamogeton*, and *Myrica*) and coastal humid forest (gastropods *Carychium*, *Succinea*, *Goniodiscus*, and

228 *Vertigo*), oxbows (ostracod *Vestalenula*), and a temporary water milieu in inland. The humid
229 forest growing around a swampy stagnant bay was a feature of the eastern margin. The
230 southwestern margin formed a shallow, littoral zone with the input of gravel from the southwest.
231 The coast was covered by wetland passing into forest, with thermophilic trees and highland
232 vegetation further inland (Kováč et al., 2011; Pipík et al., 2012). The $^{87}Sr/^{86}Sr$ isotopic ratios of
233 faunal shells (bivalves and ostracods) from the northern part of the Turiec Basin are higher and
234 more variable ($^{87}Sr/^{86}Sr \approx 0.708169 \pm 0.000009$ to 0.708320 ± 0.000016) compared to the
235 southern part, and reflect the lithological diversity of the exposed rocks, including
236 metamorphosed Paleozoic basement, Upper Devonian to Lower Carboniferous granites,
237 Mesozoic carbonates, and Paleogene flysch-like deposits (Pipík et al., 2012).

238 The deep water grey calcareous muds of the Martin Formation, which contain various amounts
239 of sand, silt, and organic matter intercalations concentrated in thin layers, were deposited in a
240 stable, cold environment below the thermocline, without significant ecological variation and
241 annual fluctuations in temperature. This biotope was characterized by an endemic, species-rich
242 ostracod association dominated by benthic *Candoninae* (Pipík and Bodergat, 2007). The degree
243 of diversity in the benthic ostracods suggests oxidizing conditions at the water-sediment
244 interface. Shells from the southern part of the Turiec Basin exhibit low and homogeneous
245 isotopic ratios ($^{87}Sr/^{86}Sr \approx 0.708011 \pm 0.000015$ to 0.708093 ± 0.000010), influenced by the
246 sediment provenance of Mesozoic carbonates and Miocene volcanic rocks. The occasional
247 higher strontium isotopic ratios of the lake waters reflect a change in drainage, potentially
248 caused by a tectonic event or an extension of lake circulation during a significant flooding event
249 (Pipík et al., 2012).

3. Methods

Detailed description of the material and methods is available in Šujan et al. (submitted). Raw datasets are included in (Šujan et al., 2022).

3.1 Facies analysis and stratigraphy

The standard facies analysis of clastic sediments includes a description of grain size, structure, texture, the geometry and size of the strata, and a visualization of information gained in logs and schemes (Stow, 2005; Miall, 2006). This facies analysis was applied to nine outcrops. The granulometry and rounding of clasts of gravelly facies were analysed by sieving eight samples from the Blažovce, Ondrašová, Valča, and Slovany outcrops, while the granulometry of muddy facies was investigated in eight samples from the Blažovce site using laser diffraction with a Malvern Mastersizer 3000 facility.

The correlation of the facies associations determined on outcrops was performed using the lithological profiles of 45 boreholes. The orientation of the geological sections was selected taking into consideration the best possible representation of the geological structure in the area of studied outcrops in terms of the availability of borehole data. These data were obtained from documents located in the Geofond archive of the State Geological Survey of Dionýz Štúr, and are listed in Table 1 of Šujan et al. (submitted). The lithology was unified using a code of 15 lithological classes, including a distinction between subaerial and subaquatic muddy lithotypes (Fig. 2 in Šujan et al., submitted). The precision of the lithological log descriptions generally permitted us to distinguish units up to a thickness of 0.5 m, while thinner strata are identified only occasionally. The criteria used to distinguish the facies associations defined in the outcrops and used for correlation in borehole geological sections are included in Table 2 of Šujan et al. (submitted). The fault network disrupting the basin fill indicated by Zbořil et al. (1985) was considered during correlation (Fig. 1C). While the generalized geological sections are presented

in the paper, the detailed lithological profiles of the borehole logs are included in Figs. 3–5 of Šujan et al. (submitted).

3.2 Authigenic $^{10}Be/^{9}Be$ dating

3.2.1 Principles of the method

The cosmogenic nuclide ^{10}Be is produced in the atmosphere by the interaction of cosmic rays with nuclides of oxygen and nitrogen. The stable isotope of beryllium, ^{9}Be, is derived from parent rock by the decomposition of primary minerals by chemical weathering (Measures and Edmond, 1983; Brown et al., 1992). Meteoric ^{10}Be is transferred to the Earth's surface in soluble form by precipitation (Raisbeck et al., 1981), and ^{9}Be is dissolved in a water column of the hydrosphere (Measures and Edmond, 1983; Brown et al., 1992). Authigenic rims form around sediment particles during their transport in a water column, predominantly composed of oxi-hydroxides of iron and manganese (Bourles et al., 1989; Willenbring and von Blanckenburg, 2010; Wittmann et al., 2012). This authigenic phase is the main carrier of isotopes ^{9}Be and ^{10}Be, and is where the authigenic $^{10}Be/^{9}Be$ ratio forms. The continuous growth of authigenic rims has been suggested for sedimentary particles during their transport (Wittmann et al., 2012). Hence, the authigenic phase records changes in the $^{10}Be/^{9}Be$ ratio of a water column of shifting depositional environments, through which a particle is carried. In general, the inner authigenic rim precipitated in riverine and deltaic environments preserves the $^{10}Be/^{9}Be$ characteristics of continental erosion (higher input of ^{9}Be), whereas the outer rim incorporates a ratio with an open-ocean composition (lower input of ^{9}Be). The effect of different water masses mixing on the water column on the $^{10}Be/^{9}Be$ ratio was recently observed in the Pear River Estuary (Kong et al., 2021).

The development of the leaching procedure by Bourles et al. (1989) to extract the authigenic phase of beryllium isotopes from sediments has already been in use for several decades. The

method, initially developed for dating marine sediment, is also applicable to continental environments, as well, and with promising results (Lebatard et al., 2008; Lebatard et al., 2010; Novello et al., 2015; Šujan et al., 2016; Simon et al., 2020; Šujan et al., 2020). The principle for age calculation is based on the radioactive decay of ^{10}Be, and this is given by the equation $N = N_0 \times e^{-\lambda t}$, where N is the authigenic ^{10}Be/^{9}Be ratio measured in the sample to be dated, N_0 is the initial authigenic ^{10}Be/^{9}Be ratio during deposition, λ is the radioactive decay constant of ^{10}Be and t is the time elapsed since deposition. Determination of the initial ratio is thus essential to obtain reliable depositional ages, but the difference in sources of both isotopes adds complexity to this requirement. Initial authigenic ratios vary significantly in recent continental sediments, between 3.5×10^{-8} and 1.55×10^{-10} (Brown et al., 1992; Graham et al., 2001; Wittmann et al., 2012), and in the case of oceanic sediments, values range between 0.5×10^{-8} and 30×10^{-8} (Yokoyama et al., 1978; Krishnaswami et al., 1982; Ku et al., 1982; Measures and Edmond, 1982; Sharma and Somayajulu, 1982; Inoue et al., 1983; Kusakabe et al., 1987; Sharma et al., 1987; Bourles et al., 1989; Henken-Mellies et al., 1990; Ku et al., 1990; Kusakabe et al., 1991; Brown et al., 1992; Measures et al., 1996; von Blanckenburg et al., 1996; Carcaillet et al., 2004; Lachner et al., 2013; von Blanckenburg and Bouchez, 2014). It is thus necessary to determine regional authigenic N_0 linked to a given deposited sediment. Then the radioactive decay of ^{10}Be can be used to calculate the age of the deposits – if two conditions are met: (1) the initial authigenic ratio N_0 is determined accurately, and (2) the samples selected must have remained closed to the entry or loss of both isotopes, that is, excepting the radioactive decay of ^{10}Be. Two approaches which aim to determine a robust initial ratio are (1) by measuring recent sediment samples which are deposited in a similar environment and drainage basin as the sediment to be dated, or (2) by the analysis of independently dated samples representing a similar depositional environment and drainage basin as the samples to be dated. Changes in

other aspects such as sediment provenance, climate and denudation rate should certainly be considered.

3.2.2 Strategy for the initial $^{10}Be/^{9}Be$ ratio determination

It has been suggested that, considering the half-life of ^{10}Be, a depositional record with an age of < 200 ka is suitable for the determination of the initial ratio (e.g, Lebatard et al., 2008). The Turiec Basin accumulated various facies during this period. Four sites were selected for determination of the initial authigenic $^{10}Be/^{9}Be$ ratio: (1) the Late Pleistocene alluvial fan Veľký Čepčín (7 Samples), (2) the Late Pleistocene river terrace Malý Čepčín (2 samples), (3) the Holocene river floodplain Košťany (3 samples) and (4) the Holocene river floodplain Kaľamenová (3 samples) (Fig. 1C). The age of the sites had been established by previous research (Gašparík and Halouzka, 1993; Kováč et al., 2011; Holec and Braucher, 2014; Sládek et al., 2022). The sites represent different sediment supply to accommodation rate ratios, with the alluvial fan having the highest sediment supply and rapid burial forming a topographic elevation, while the Holocene floodplain accumulated in a topographically low-lying location with a reduced sediment supply. The aim was to determine the natural authigenic $^{10}Be/^{9}Be$ variability in the basin in different paleoenvironmental conditions of the sites analysed.

3.2.3 Sampling strategy for dating

In total, 31 samples were collected from nine outcrops (Fig. 1C). The outcrops were selected to represent different facies associations (section 4.1) including alluvial fans (the Ondrášová, Valča and Slovany sites), braided rivers (the Socovce and Abramová sites), a fan delta (Blažovce site), and open lakes (the Martin - claypit, Turčiansky Peter and Kúdel sites), to determine the temporal relationship of the depositional systems. Two to seven samples (3 on average) were collected from each site from different layers within an outcrop to discriminate outliers and to find out the degree of paleoenvironmental variability of the beryllium isotopic

ratio. In order to trace this variability, rather than collecting multiple samples from a single layer, sampling several layers in a superposition was preferred.

3.2.4 Sample processing

Sample preparation was performed at the Department of Geology and Paleontology laboratory, Faculty of Natural Sciences, Comenius University in Bratislava, based on (Bourles et al., 1989; Carcaillet et al., 2004) and tested by Šujan et al. (2018) for the facility at the faculty. The samples collected were dried in an oven at a temperature of 60°C and crushed, then the extraction procedure was applied to ~2.25 g of a sample using 0.04 M NH_2OH–HCl in a 25°% acetic acid leaching solution (Bourles et al., 1989). An aliquot of ~2 ml was taken from the leached solution for measurement of ^{9}Be concentration in an ICP-MS, and this was performed at the Institute of Chemistry, at the Slovak Academy of Sciences. To minimize the error in the measurement of ^{9}Be concentration by the matrix effect, the linear regression method was used (Tan and Horlick, 1987). The same aliquot solution also underwent measurements of selected element concentrations. An amount of ~450 µg of beryllium carrier solution was added to the remaining leached solution (Scharlau, 1000 ppm; $^{10}Be/^{9}Be$ ratio of $7–8 \times 10^{-15}$ (Merchel et al., 2021)). Spiked samples were evaporated, and beryllium was separated from other elements in the sample using column chromatography (Merchel and Herpers, 1999). The precipitate that now remained, containing only beryllium, was washed with pH 8 water and left overnight for ageing (Merchel et al., 2019). The final precipitate was dissolved in a few drops of HNO_3, dried and heated at 800 °C for 1 h. The resulting BeO was mixed with niobium powder and pressed into cathodes for accelerator mass spectrometer (AMS) measurements. $^{10}Be/^{9}Be$ isotopic ratios were measured at the French national AMS facility ASTER, CEREGE (Aix-en-Provence, France). The measurements were calibrated directly against the STD11 in-house standard ($^{10}Be/^{9}Be$ value of $(1.191 \pm 0.013) \times 10^{-11}$) (Braucher et al., 2015). Analytical uncertainties

(reported as 1σ) include uncertainties associated with AMS counting statistics, chemical blank measurements and the AMS internal error (0.5%).

Each $^{10}Be/^{9}Be$ sample ratio was corrected using its corresponding chemical blank (one chemical blank was processed every seven analyzed samples). The $^{10}Be/^{9}Be$ blank ratios ranged from 6.61×10^{-15} to 9.62×10^{-15}.

3.3 Geochemistry and mineralogy

3.3.1 Whole rock geochemistry

Whole rock XRF analyses (major oxides) were made from eight samples selected as representative of dating sites (except Slovany), and from four samples selected as representative of Quaternary sites, which were used for calibration of the authigenic $^{9}Be/^{10}Be$ initial ratio. Hence, each sample represents one studied site.

XRF measurements were carried out at the laboratory of the Slovak National Museum in Bratislava, Slovakia, using an ARL Quant'X (Thermo Scientific Inc., USA) EDXRF spectrometer. Excitations rays are produced by an air-cooled X-ray tube and the X-rays emitted are detected by means of a Peltier cooled Si (Li) detector, and a pulse processor. The XRF data were calibrated and matrix-corrected using Uniquant software (Ver 5.46), on the basis of a set of fundamental parameters and unique algorithms. Certified reference materials (NSC DC73043, CRM016-50, BCR-176R and BCR-320R) were also integrated with Uniquant data processing. All the measurements were performed in a vacuum.

Additionally, five whole rock samples from the Blažovce quarry were analyzed using ICP-ES (major oxides) and ICP-MS (trace elements) in the Bureau Veritas mineral laboratories (Canada, Vancouver). The samples were pulverized and dissolved using Lithium Borate Fusion. The content of TOC, C and S was analyzed using the LECO Carbon-Sulfur analyzer. Enrichment factors were calculated as $X_{EF} = (X_{sample}/ Al_{sample})/(X_{UCC}/Al_{UCC})$, where the

394 normalization values UCC follow McLennan (2001). The CIA index (Nesbitt and Young, 1982)
395 was calculated using a simplification developed by McLennan (1993).

396 **3.3.2 Mineralogy of whole rock and clay fraction**

397 Twelve silty mud samples collected from the outcrops were analyzed using the X-ray
398 diffraction (XRD) method at the Croatian Geological Survey, Zagreb. XRD patterns were
399 recorded on random mounts of whole rock samples and oriented mounts of the <2 μm fraction
400 using a PANalytical vertical goniometer (type X`Pert) equipped with a Cu-tube and under the
401 following experimental conditions: 45 kV, 40 mA, PW 3018/00 PIXcel detector, primary beam
402 divergence 1/4° and continuous scan (step 0.02 °2θ/s). Preparation for the XRD analyses
403 included: sample grinding for whole rock analyses, sieving the samples through the 63 μm sieve
404 to remove part of carbonate content and then separation of the <2 μm fraction from the sample
405 by centrifugation (Krumm, 1994) for oriented mounts (glass slides). Oriented samples of the
406 <2 μm fraction were recorded after the treatments described in Šujan et al. (submitted). The
407 identification of clay minerals was performed according to Starkey et al. (1984) and Moore and
408 Reynolds (1997). The X-ray interpretation was performed using High Score Plus (PANalytical,
409 2016) calculation and the database of the International Centre for Diffraction Data (2022).

410 **3.3.3 Authigenic phase ICP-MS of Fe and Mn**

411 The aliquots taken for the analysis of beryllium concentration in all dating samples were subject
412 to the measurement of their iron and manganese concentration using ICP-MS, since these
413 elements are expected to form the major portion of the oxy-hydroxides leached from the
414 authigenic phase (Wittmann et al., 2012). The analyses were performed specifically to observe
415 variations in elemental concentrations in correlation with beryllium and $^{10}Be/^{9}Be$ ratio as a
416 potential indicator of post-depositional growth of the authigenic rims, since this is a possible
417 effect modifying the authigenic $^{10}Be/^{9}Be$ record due to various duration of a soil profile

418 exposure (Tsai et al., 2008; Graly et al., 2010; Willenbring and von Blanckenburg, 2010; Bacon
419 et al., 2012; Dixon et al., 2018).

420 4. Results

421 4.1 Facies associations on outcrops

422 Facies analysis allowed us to distinguish 27 distinct lithofacies, which are listed in Table 1,
423 together with a description and interpretation of the depositional processes in play in each case.
424 The stacking patterns of the observed lithofacies implied their grouping into four facies
425 associations (Table 2), and these are described and interpreted below.

426 Table 1: List of lithofacies documented on the outcrops in the Turiec Basin, their
427 properties and interpreted depositional processes.

Code	Lithology, structure, texture and geometry	Depositional processes
Gm, GSm	massive matrix-supported gravel to gravelly coarse- to medium-grained sand, granules, pebbles and boulders, poorly sorted, angular to subangular, forming tens of centimeters to meters thick, possibly amalgamated bodies	subaerial debris flow (Nemec and Steel, 1984; Pierson and Costa, 1987; Brenna et al., 2020)
Gmg	massive normally graded clast- to matrix-supported gravel, sandy matrix, granules to pebbles, fewer boulders, forming tens of centimeters to meters thick horizontal tabular bodies	hyperconcentrated flow (Pierson and Costa, 1987; Brenna et al., 2020)
Gmgr	massive reverse graded clast- to matrix-supported gravel, sandy matrix, granules to pebbles, fewer boulders, angular to subangular, forming tens of centimeters to meters thick horizontal tabular bodies	subaerial debris flow (Nemec and Steel, 1984; Pierson and Costa, 1987; Brenna et al., 2020)
Gk	massive clast-supported gravel, moderate to well sorted, subangular to rounded, granules and pebbles, forming ~0.5–1.0 m thick amalgamated tabular and lenticular bodies, frequently amalgamated, infrequent muddy-sandy intraclasts	debris flood (Church and Jakob, 2020; Brenna et al., 2020)
Gkg	massive normally graded clast-supported gravel, moderate to well sorted, angular to subangular, matrix almost absent, granules to pebbles, fewer boulders, forming tens of centimeters thick horizontal tabular bodies	hyperconcentrated flow (Church and Jakob, 2020; Brenna et al., 2020)
GFp	clast-supported gravel, poorly imbricated, pebbles, fewer granules, moderate to well sorted in a single bed, subangular to rounded, inclined layers of sandy mud a few centimeters thick forming foreset-like intercalations	shallow traction current, accretion of a bar in poorly topographically defined shallow channel, periodical variation of transport capacity (Šujan et al., 2021)

Gt	clast-supported gravel arranged into inclined beds few centimeters thick, tangential contacts with base, granules to pebbles, moderate to well sorted in a single bed, subangular to rounded, arranged into lenticular bodies few meters thick with a concave erosional base	channelized traction current, accretion of a bar (Boothroyd and Ashley, 1975; Nemec and Postma, 1993; Gobo et al., 2016; Martini et al., 2017)
Gh	clast-supported gravel arranged into subhorizontal beds a few centimeters thick, granules to pebbles, subangular to rounded, forming tens of centimeters thick horizontal tabular bodies	sheet flow (Blikra and Nemec, 1998; North and Davidson, 2012)
Gh-for	clast-supported gravel arranged into planar beds a few centimeters thick, granules to pebbles, forming tens of centimeters thick 10–20° inclined tabular bodies within 5–7 m thick clinoforms	stratified subcritical high-density turbidity current on a fan delta foreset (Postma and Cartigny, 2014)
Gk-for	massive clast-supported gravel, granules to pebbles, less boulders, forming tens of centimeters thick 10–20° inclined tabular bodies within 5–7 m thick clinoforms	grainflow on a fan delta foreset (Lowe, 1976; Nemec and Steel, 1984; Mulder and Alexander, 2001)
Gmg-for	massive normally graded clast- to matrix-supported gravel, granules to pebbles, fewer boulders, forming tens of centimeters thick 10–20° inclined tabular bodies within 5–7 m thick clinoforms	hyperconcentrated flow on a fan delta foreset (Mulder and Alexander, 2001; Tallling et al., 2012)
Gmh	massive clast-supported gravel, granules to pebbles, fewer boulders, forming tens of centimeters thick stacked tabular bodies, shape frequently curved and deformed	stratified subcritical high-density turbidity current on a fan delta bottomset (Postma and Cartigny, 2014) deformed by loading of a prograding delta front (Longhitano, 2008)
Gmm	massive matrix-supported gravel, granules to pebbles, fewer boulders, forming ca. 10 cm thick isolated tabular bodies	hyperconcentrated flow (Mulder and Alexander, 2001) or non-cohesive debris flow (Tallling et al., 2012) on a fan delta bottomset
Sl-for	medium- to coarse-grained sand, in ca. 1 cm thick planar beds with wavy undulations, infrequent granules, strata arranged in tens of centimeters thick 10–20° inclined tabular bodies within 5–7 m thick clinoforms	low-density subcritical turbidity current (Postma and Cartigny, 2014) or hyperpycnal flow (Mulder et al., 2003) on a fan delta foreset
Sw	medium- to coarse-grained sand, forming wavy stratification with concave and convex shapes, in lenses or tabular bodies ca. 5 cm thick, usually in between gravelly bodies	suspension fallout from a supercritical traction current (Fielding, 2006; Cartigny et al., 2014)
Sm	massive medium- to coarse-grained sand, forming tens of centimeters thick tabular bodies or lenses, may contain muddy intraclasts	rapid deposition from a waning flow with high sediment concentration (Mulder and Alexander, 2001; Baas et al., 2016)
Sh	horizontally laminated fine-grained sand, loading-related faulting and deformations appear	low-density subcritical turbidity current (Postma and Cartigny, 2014) or hyperpycnal flow (Mulder et al., 2003) on a fan delta bottomset, deformed by loading of a prograding delta front (Longhitano, 2008)
Sl	medium- to fine-grained sand, in ca. 1 cm thick planar beds, strata arranged in tens of centimeters thick tabular bodies	low-density subcritical turbidity current (Postma and Cartigny, 2014) or hyperpycnal flow (Mulder et al., 2003) on a shallow lake bottom
SFr	unidirectional ripple cross-stratified muddy sand	slow traction current (Allen, 1982; Yawar and Schieber, 2017)

Srw	symmetrical ripple cross-stratified fine- to medium-grained sand	oscillatory traction current (Dumas et al., 2005; Amoudry et al., 2013)
Shc, SFhc	hummocky cross-stratified sand or muddy sand	storm wave oscillatory traction current (Dumas and Arnott, 2006; Jelby et al., 2020)
St	trough cross-stratified fine-grained sand in lenticular bodies	traction current forming 3D dunes (Allen, 1982; Leclair and Bridge, 2001)
SFd	beds of laminated sand and sandy mud, arranged in folds, deformed penecontemporaneously	deformation of sediment due to slumping or loading of a prograding delta front (Longhitano, 2008; Owen et al., 2011)
SFh, FSh	horizontally laminated very fine-grained muddy sand to sandy mud, deformations and loading-related faulting appear	low-density subcritical turbidity current (Postma and Cartigny, 2014) or hyperpycnal flow (Mulder et al., 2003) on a shallow lake bottom
Fl, FSl	laminated light brown to reddish mud or sandy mud	deposition from a slow traction current or suspension in a proximal floodplain or on an alluvial fan (Aslan and Autin, 1999; Yawar and Schieber; 2017)
Fm, FSm	massive light grey, light brown to reddish mud to muddy sand	deposition from a suspension of a high mud-concentrated waning flow in an oxbow lake, on a proximal floodplain or an alluvial fan (Toonen et al., 2011; Baas et al., 2016)
Fh	horizontally laminated grey to blue mud, occasional mollusc shells	slow traction current on a lake bottom (Allen, 1982; Yawar and Schieber, 2017)
Fmb, SFmb	massive dark grey to blue mud, presence of mollusc and trace fossils	primary processes questionable, structures reworked by bioturbation (Scott et al., 2012), deposition likely by suspension settling in a calm water column (Potter et al., 1980, 2005),

4.1.1 FA1: Alluvial fan deposits

Description:

The first facies association was documented on the Valča, Ondrašová, and Slovany outcrops (Fig. 3). Relatively extensive outcrops allow a quantitative evaluation of the lithofacies (Table 4 in Šujan et al., submitted). The lithofacies assemblage is dominated by gravelly or sandy-gravelly tabular bodies, forming 80.3°% (Valča), 89.7°% (Ondrašová) and 80.8°% (Slovany)

435 of the stratigraphic sections. The remaining proportions of the outcrops comprise tabular or
436 lenticular bodies of sandy muds or muds reaching thicknesses of generally < 30 cm.

437 The Valča site consists of the most variable lithofacies (Fig. 3 A1, A2). Massive matrix-
438 supported gravels or gravelly sands with a low level of sorting (Gm, GSm, Sm) alternate with
439 normally or reverse graded gravels (Gmg, Gmgr) and with clast-supported gravel with poorly
440 developed imbrication and foreset-like sandy mud intercalations (GFp). While Gm, GSm, and
441 Sm lithofacies attain only a relatively low average thickness (AT = 0.27 m) and high abundance
442 (16), Gmg, Gmgr, and GFp lithofacies occur much less frequently and with a relatively high
443 average thickness of AT = 0.95–1.41 m. The gravelly units mentioned above are separated by
444 frequent massive sandy muds or muds (FSm. Fm) with AT = 0.18 m and by less frequent
445 laminated sandy muds (FSl) with AT = 0.15 m.

446 The Ondrašová section is less complex, consisting mostly of massive matrix-supported gravels
447 and gravelly sands (GSm, Gm) with AT = 0.98 m, divided by massive sandy muds or muds
448 (FSm, Fm) reaching AT = 0.09 m or by laminated muds (Fl) attaining AT = 0.18 m (Fig. 3B).

449 The Slovany outcrop is predominantly comprised of massive matrix-supported gravel (Gm; AT
450 = 0.63 m) and reverse graded gravel (Gmgr; AT = 1.75 m) (Fig. 3C). The gravelly units are
451 separated by massive sandy muds and muds (FSm, Fm; AT = 0.34 m) and by laminated sandy
452 muds (FSl; AT = 0.19 m). The muddy horizons below the reverse graded gravels exhibit
453 penecontemporaneous deformations resembling flame structures (Fig. 3C).

454 A relatively poorly sorted (3.1-3.3 phi) fraction with a content of 5–10 % muddy to fine-grained
455 sandy is documented in the lithofacies Gm by cumulative granulometric curves seen in Fig.6
456 of Šujan et al. (submitted). The GSm lithofacies contains a significantly higher proportion of
457 fine-grained sand and mud. A bimodal character is implied by the cumulative granulometric
458 curve of the GFp lithofacies, with higher content of medium-grained sand. Following Folk and
459 Ward (1957), the sorting of all samples reaches values of 3.11–3.44 and may therefore be

classified as very poorly sorted (Table 5 in Šujan et al., submitted). Gravels from all three sites exhibit a sub-angular to sub-rounded nature, with a less frequent presence of rounded clasts in the grain size classes between 16 mm and 64 mm (Figs. 7–10 in Šujan et al., submitted). The petrography of the gravel clasts is monotonous on the basis of macroscopic evaluation, with the presence of light and dark limestones, and somewhat less frequent dolomites. Clasts from the Valča site are yellow to reddish in color by secondary precipitation (Fig. 8 in Šujan et al., submitted).

Interpretation:

The most common lithofacies, those with massive matrix-supported gravel to gravelly sand and characterized by poor sorting (Gm, GSm) may be interpreted as subaerial debris flow (Nemec and Steel, 1984; Pierson and Costa, 1987; Brenna et al., 2020). The reverse graded massive clast- to matrix-supported gravel (Gmgr) was also likely formed by the process of subaerial debris flow (Pierson and Costa, 1987; Brenna et al., 2020). On the other hand, the appearance of the massive normally graded clast- to matrix-supported gravel (Gmg) implies its origin as hyperconcentrated flow (Pierson and Costa, 1987; Brenna et al., 2020). A debris flow represents the gravitational movement of a highly-concentrated shearing mixture of debris and water (Van Dine, 1985; Blikra and Nemec, 1998), whereas a hyperconcentrated flow is characterized by a high concentration of sediment transported in suspension and by rapid and intense deposition from suspension fallout (Pierson and Costa, 1987; Pierson, 2005; Church and Jakob, 2020). The GFp lithofacies, composed of clast-supported, poorly imbricated gravel with the presence of foreset-like inclined muddy intercalations may be interpreted as a deposit of a traction current in a shallow channel (Šujan et al., 2021a), as distinct from the gravity flows mentioned above. The overall volumetric dominance of subaerial surge-type flows in the depositional record of FA1 indicates its origin as formed by alluvial fans, with a lower proportion of deposition in shallow channels (Blikra and Nemec, 1998; Plink-Björklund, 2021; Šujan, 2021) (Table 2).

485 Some of the massive matrix-supported gravel units (Gm, GSm) reach considerable thicknesses
486 – up to 3.15 m and are likely composed of several amalgamated depositional events. Massive
487 sandy mud and mud layers (FSm, Fm) represent abrupt suspension fallout deposition from a
488 surge-type flow with a high concentration of fine-grained sediment (Baas et al., 2016), which
489 is likely associated with slopewash processes on the surface of an alluvial fan (Nemec and
490 Kazanci, 1999). The very small proportion of laminated sandy mud or laminated mud layers
491 (FSl, Fl), reaching 3.8–7.0 %, implies minor deposition from slow traction currents or even
492 from suspension in a standing water column (Aslan and Autin, 1999; Yawar and Schieber,
493 2017).

494 Table 2: Facies associations defined based on lithofacies stacking patterns observed
495 on the outcrops in the Turiec Basin.

Facies association	Sedimentary environment	Facies	Processes
FA1	Alluvial fan	Gm, GSm, Gmg, Gmgr, GFp, Sm, FSm, Fm, FSl	unconfined subaerial gravity flows, less frequent channelized episodic floods and traction currents
FA2	Braided river	Gk, Gm, SGm, Gkg, Gh, Sm, Fl	episodic floods and traction currents in shallow channels, overbank well-drained floodplain deposition, less frequent unconfined subaerial gravity flows
FA3	FA3a: Fan delta topset	Gh, Gt, Gmg, Gm, Sw, FSl	channelized traction current or shallow unconfined traction current, less frequently unconfined subaerial gravity flows
	FA3b: Fan delta foreset	Gh-for, Gmg-for, Gk-for, Sl-for	high sediment-concentrated gravity currents on a fan delta slope, mass-wasting and slope processes
	FA3c: Fan delta bottomset	FSh, SFh, Fh, FSd, Fm, Sl, Sw, Gmh, Gmm	high sediment-concentrated gravity currents on the toe of a fan delta slope, low sediment-concentrated turbidity currents in transition to open lake environment, deformations due to loading of the prograding delta
FA4	Open lake	Shc, FShc, FSh, SFh, Fmb, SFmb, FSr, Sm, St	deposition below normal weather wave base, oscillatory storm wave currents alternate with deposition from suspension, slow bottom currents or distal hyperpycnal flows

496

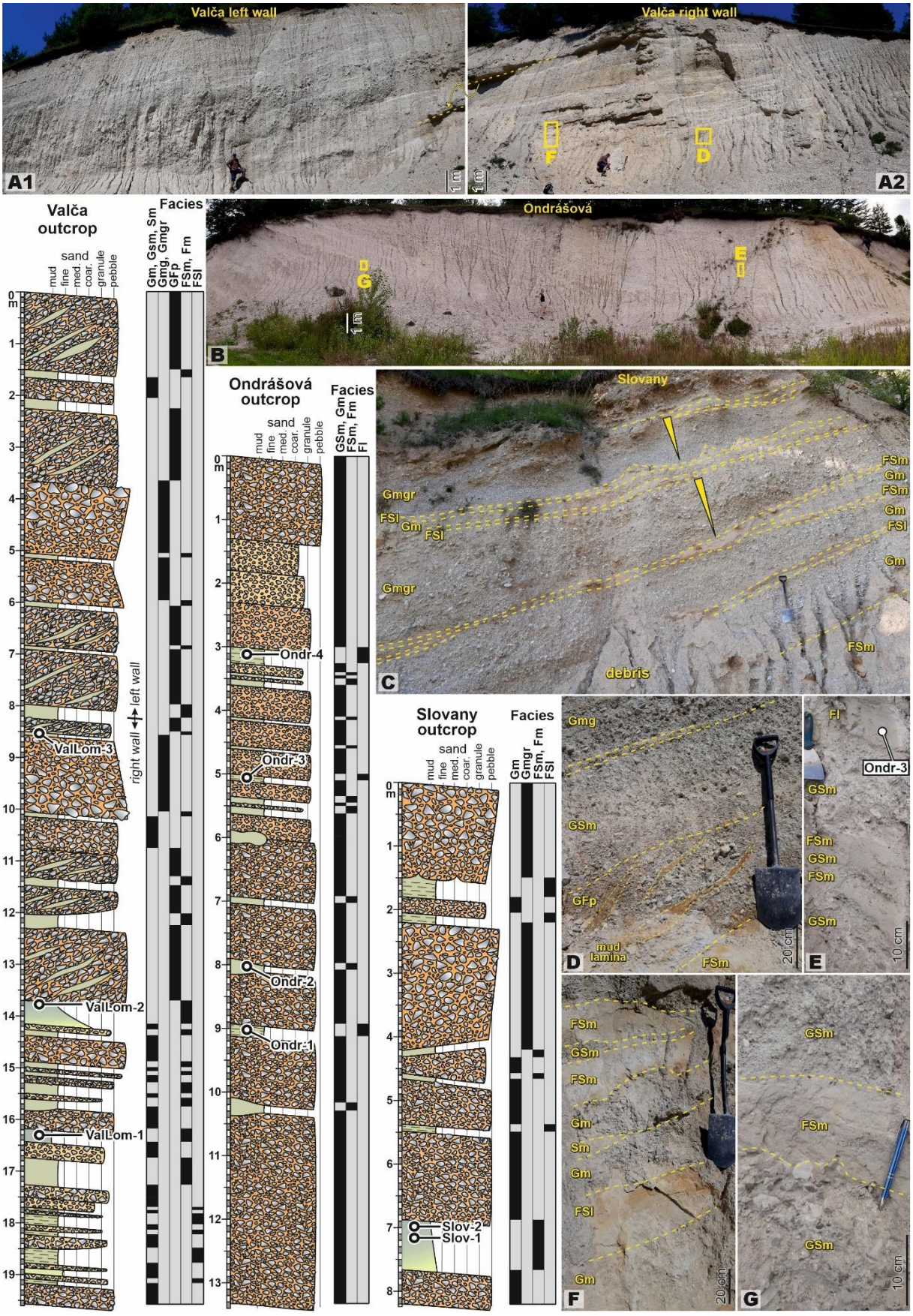
Valča left wall
A1
Valča right wall
A2
F
D
Ondrášová
B
E
G
Valča outcrop
sand
mud
fine
med.
coar.
granule
pebble
Facies
Gm, Gsm, Sm
Gmg, Gmgr
GFp
FSm, Fm
FSl
left wall
right wall
ValLom-3
ValLom-2
ValLom-1
Ondrášová outcrop
Ondr-4
Ondr-3
Ondr-2
Ondr-1
GSm, Gm
FSm, Fm
Fl
Slovany
C
Gmgr
FSl
Gm
FSm
debris
Slovany outcrop
Slov-2
Slov-1
Gm
Gmgr
FSm, Fm
FSl
Gmg
GSm
GFp
mud lamina
D
20 cm
Fl
Ondr-3
E
10 cm
Sm
F
G

497

Fig. 3. Alluvial fan facies association documented on the sites Valča, Ondrašová and Slovany, with photo-documentation of stratal geometry (A–C) and lithofacies (D–G). Lithofacies codes are explained in Table 1.

4.1.2 FA2: Braided river deposits

Description:

Facies association 2 was documented on the Abramová – Kolísky and Socovce sites. The scale and character of the outcrops allow only for a qualitative facies analysis. The Abramová – Kolísky site may be regarded as the type locality of the Abramová Member (Kováč et al., 2011). A major part of the Abramová – Kolísky site consists of massive clast-supported gravel with moderate to well sorting, 20–30 cm thick (Gk), forming amalgamated bodies. The boundaries of individual, likely lenticular bodies can be observed locally by tracing a change in the prevailing grain size (Fig. 4). The Gk facies include deformed sandy-muddy intraclasts in its uppermost portion (Fig. 4D). A significant proportion of the stratigraphic section is formed by massive normally graded clast-supported gravel (Gkg), locally divided by planar beds of clast-supported gravel few centimeters thick (Gh) (Fig. 4D, E). The boundaries of tabular bodies are undulating. On the other hand, laminated light brown to reddish mud (Fl) comprises around one-third of the observed stratigraphic column (Fig. 4C). The transition upwards from gravelly to muddy facies is associated with the presence of 10–20 cm thick massive medium- to coarse-grained sand units (Sm) with an undulating erosional base and lenticular shape (Fig. 4C).

The Socovce site comprises a cliff of significantly lithified gravels reaching a thickness of ~13m (Fig. 5A, C). The lithification makes it difficult to clean the outcrop and carry out quantitative observations, nevertheless, lithofacies of massive matrix-supported gravel (Gm) and massive clast-supported gravel with moderate to well sorting (Gk) prevail (Fig. 5C). A muddy section was observed ca. 1 m above the cliff composed dominantly of laminated light brown to reddish mud (Fl) with occasional layers of massive sand a few centimeters thick (Fig. 5B).

Interpretation:

The sorting and texture of the Gk lithofacies implies its origin as a deposit of debris flood (Brenna et al., 2020; Church and Jakob, 2020). Debris flood is characterized by a water-driven flood with high bedload transport inducing full mobility of almost all grain sizes, usually confined in a steep channel, and by the deposition of bedload-carpet accretion (Manville and White, 2003; Church and Jakob, 2020). It may be contrasted with debris flow associated with the unconfined deposition of a gravity-driven non-Newtonian mixture of water and sediment (Van Dine, 1985). Debris floods are typical of mountain streams with high sediment supply and more frequent flash flood events (Brenna et al., 2020). The presence of the Gkg lithofacies records deposition of fewer frequent hyperconcentrated flows (Brenna et al., 2020; Church and Jakob, 2020). Sheet flow appeared sporadically, as evidenced by the gravelly subhorizontal beds of the Gh lithofacies (Blikra and Nemec, 1998; North and Davidson, 2012). In contrast to the previously mentioned gravelly facies, the frequently present lithofacies Fl indicate sedimentation from very slow traction currents ($<0.25\ m \cdot s^{-1}$) or from a suspension in a standing water column. The massive sand of the Sm lithofacies implies a rapid deposition from a highly sediment-saturated flow (Mulder and Alexander, 2001; Baas et al., 2016). The association of depositional processes points to an alternation of channelized traction current and surge-type flows, unconfined subaerial gravity flows and overbank calm deposition of mud, implying a depositional environment of a proximal braided river with a small catchment prone to significant yearly discharge variability (Miall, 2006; Fielding et al., 2018; Paseban et al., 2018) (Table 2).

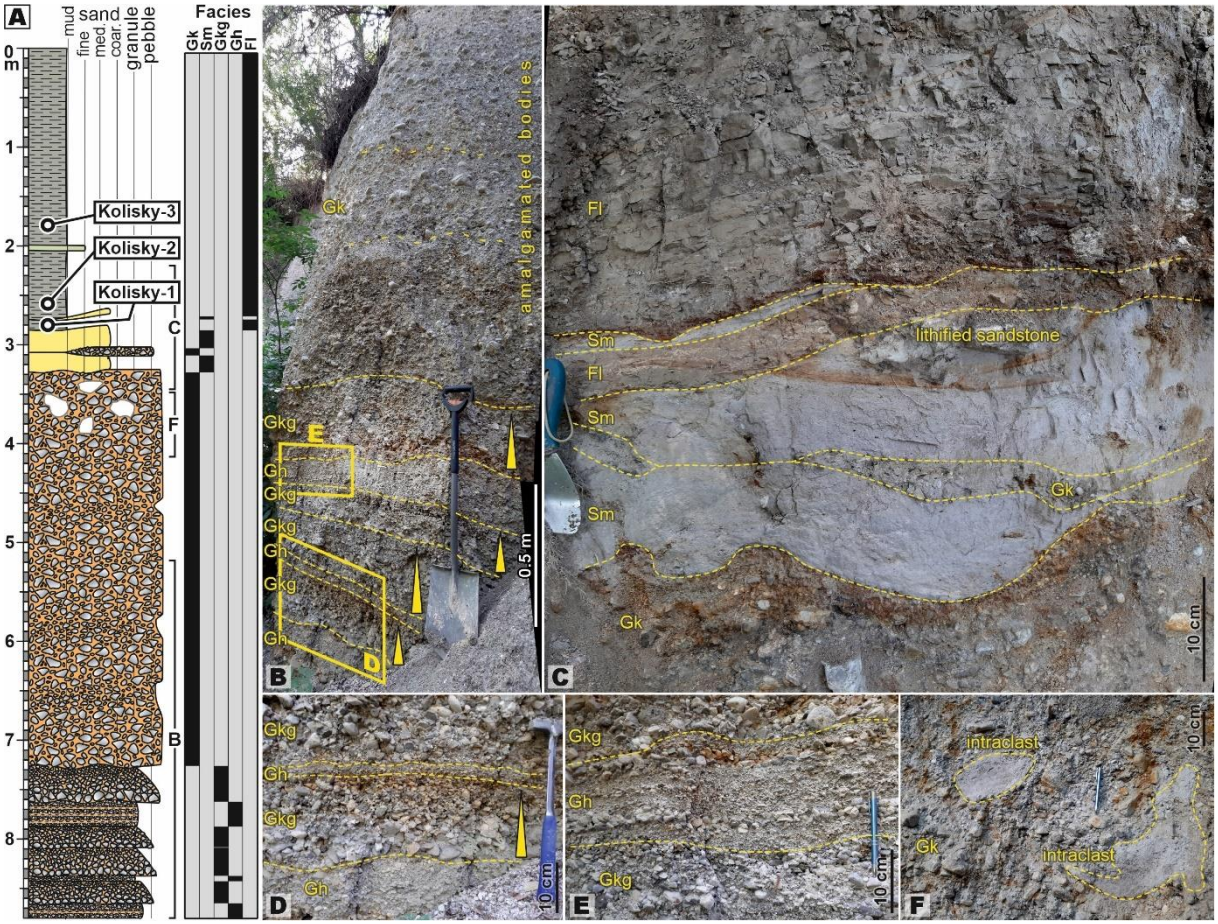

544

545 Fig. 4. Braided river facies association documented on the Abramová – Kolísky site
546 (A), with photo-documentation of stratal geometry (B) and lithofacies (C–F).
547 Lithofacies codes are explained in Table 1.

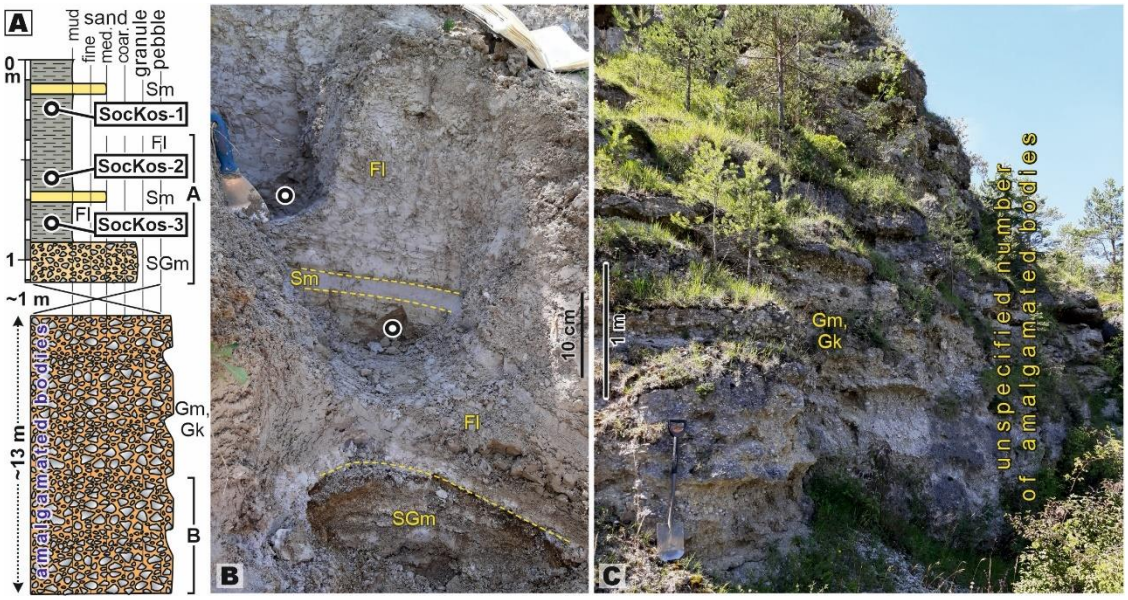

548

549 Fig. 5. Braided river facies association documented on the site Socovce (A), with
550 photo-documentation of the dating sampling point (B) and amalgamated lithofacies

with indistinct boundaries due to intense lithification (C). Lithofacies codes are explained in Table 1.

4.1.3 FA3: Fan delta deposits

Description:

The fan delta facies association was documented at a single site within the Blažovce gravel quarry. The outcropping succession reaches a thickness of 27 m and is exposed continuously on three main levels, with only ca. 2.5 m of covered interval (Fig. 12 in Šujan et al., submitted). The outcrops expose the alternation of three distinct facies sub-associations, marked as FA3a (topset), FA3b (foreset) and FA3c (bottomset) (Table 2). The Blažovce quarry is the type locality of the Blažovce Member (Kováč et al., 2011).

The sub-association FA3a (topset) is dominated by clast-supported gravel arranged into subhorizontal beds a few centimeters thick (Gh) (Fig. 6A–D) and by lenticular bodies a few meters thick with concave bases, which are composed of inclined gravelly beds with tangential contacts towards the base (Gt) (Fig. 6E). Lithofacies of massive normally graded clast- to matrix-supported gravel (Gmg) or massive matrix-supported gravel (Gm) are present less frequently, both up to few tens of centimeters thick (Fig. 7B). Intercalations between the gravelly bodies are formed occasionally by wavy laminated sandy layers a few centimeters thick (Sw) (Fig. 7B) or by laminated sandy mud (FSl) (Fig. 6E, F). The overall geometry of the FA3a strata is subhorizontal.

On the other hand, the strata of facies sub-association FA3b (foreset) are inclined at an angle, ranging between 12–25° (Figs. 7A, 8A, B, Fig. 13 in Šujan et al., submitted). The thickness of the foresets may attain 7 m (Fig. 7A), though some were observed of only 0.5–1.5 m in thickness (Fig. 6A, D). The most frequent facies forming the foresets is clast-supported gravel arranged into planar beds a few centimeters thick (Gh-for) (Figs. 6A, D; 7B), which are less frequently substituted by massive clast-supported gravelly beds some tens of centimeters thick,

usually more coarse-grained (Gk-for) (Fig. 7C). The lower parts of the thicker (>3 m) foresets frequently comprise massive normally graded clast- to matrix-supported gravels (Gmg-for), especially on the transition towards the bottomsets (Fig. 7D). A relatively rare foreset facies is composed of medium- to coarse-grained sand with floating granules and forms ca. 1 cm thick planar beds, which exhibit wavy undulations (Figs. 7C; 8A). The orientation of the foreset inclination exhibits a relatively high degree of variability from west to south-southeast, with a maximum towards southwest (Fig. 13 in Šujan et al., submitted).

The bottomset facies sub-association FA3c attains sub-horizontal bedding (Fig. 8A, C) or very gentle inclination (Fig. 9). The transition from foreset to bottomset is locally tangential with the direct continuation of the beds from inclined to sub-horizontal geometry (Fig. 8A). The most frequently observed lithofacies is composed of horizontally laminated very fine-grained muddy sand to sandy mud with the frequent presence of small-scale blind faults and deformations, and with internal erosional contacts (FSh, SFh) (Figs. 7D; 8C; 9C). These layers are commonly intercalated with: (1) horizontally laminated grey to blue plastic mud (Fh) some centimeters thick(Fig. 9B), (2) tabular bodies of deformed massive clast-supported gravel (Gmh) or massive matrix-supported gravel some tens of centimeters thick (Gmm) (Fig. 9B, C), (3) beds of sand and mud deformed in folds (SFd) (Fig. 7D), or (4) laminated medium- to coarse-grained sand (Sl) (Fig. 9B). The tangential transition from foreset to bottomset is locally associated with stratified wavy sand (Sw) a few centimeters thick (Fig. 7D). An interval of massive light brown mud with reddish bands several meters thick was observed (Fm) onlapping on the slope of underlying foreset facies (Fig. 6C, D). The boundaries of individual beds are frequently undulate and locally exhibit truncation (Fig. 9B, C).

The average grain size of gravelly facies is -0.9 to -2.9 phi (granule to pebble), and exhibits a similar degree of sorting to the alluvial fan deposits, with values of 3.20–3.27 phi (Folk and Ward, 1957), an exception being the topset Gt lithofacies, which reaches 2.37 phi (Table 5, Fig.

6 in Šujan et al., submitted). The proportion of fine sandy to muddy fraction decreases in comparison to the alluvial fan strata. Nevertheless, the rounding of the clasts is similar to the alluvial fan facies, only with a slightly lower proportion of sub-angular specimens in favor of the rounded ones (Fig. 10 in Šujan et al., submitted). A visual evaluation of petrographic composition does not indicate any difference between this and alluvial fan gravel samples (Figs. 7–10 in Šujan et al., submitted). Laser diffraction granulometry of the muddy Fh facies indicates the dominance of fine-grained silt (peak 10–11 μm), with low proportion or absence of fine sand and low proportion of clay fraction (Fig. 11 in Šujan et al., submitted). The percentual proportion of grain sizes of the Fm lithofacies exhibits a very similar pattern, with an increased clay content in the case of two samples. Two samples representing the FSh lithofacies contain different proportions of sand (6.2°% and 20.7°%), and fine- or medium-grained silt comprises the maximum volume (16 μm and 33 μm). All analyzed samples of muddy facies display poor sorting according to Folk and Ward (1957), with values in the range of 1.08–1.61 phi (Table 5 in Šujan et al., submitted).

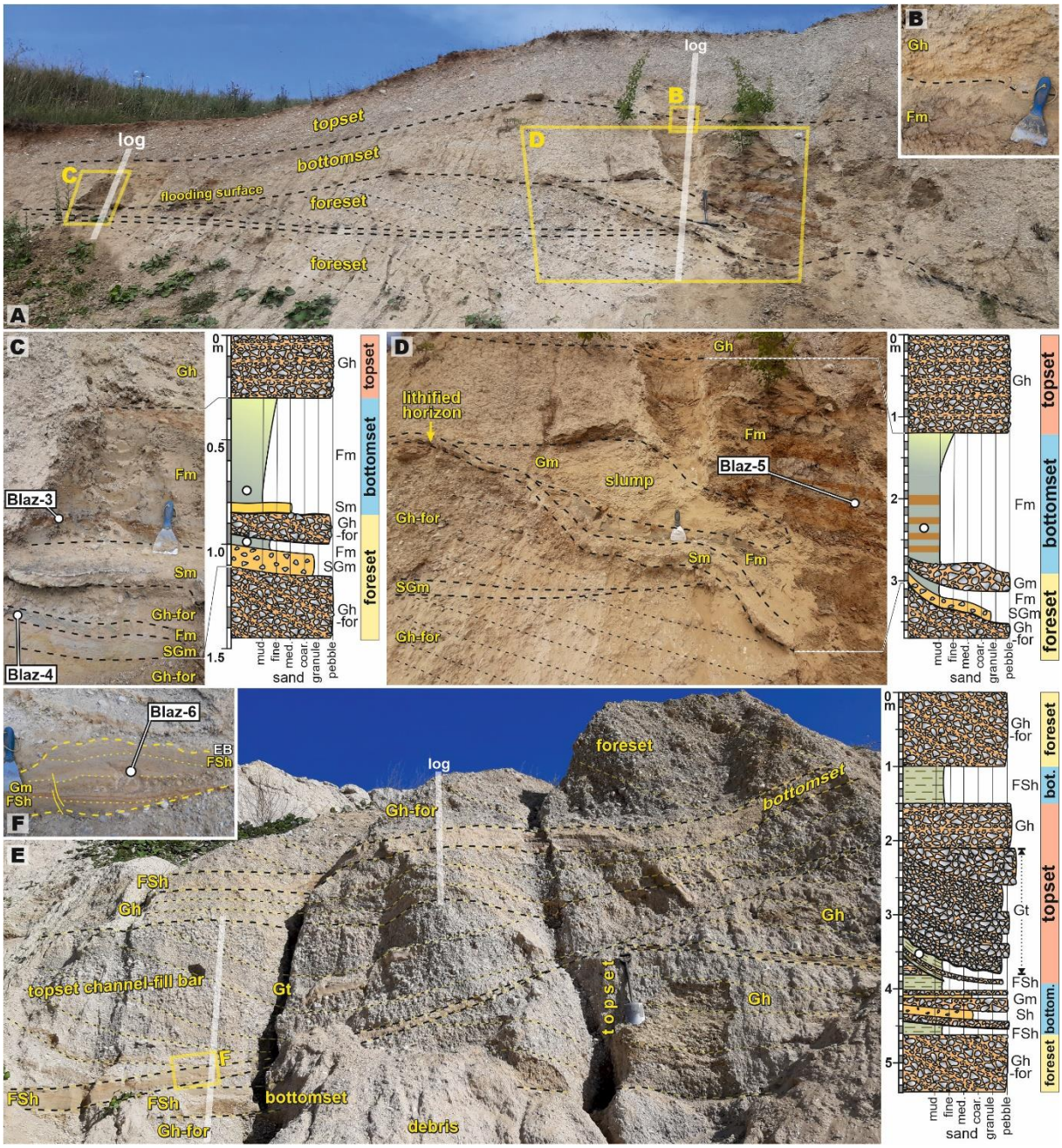

615

616 Fig. 6. Outcrops of the Blažovce site showing FA3a facies sub-associations (topset),
617 FA3b (foreset) and FA3c (bottomset) of a fan delta. (A) The inclined gravelly foreset
618 beds are overlain by massive muds of bottomset facies (C, D), and capped by the
619 subhorizontal gravels of the topset (B). (E) The topset facies commonly include
620 large, concave lenses of tangentially stratified gravels a few meters thick and 10–
621 15 m wide, which may include lenses of sandy mud (E). For location within the
622 quarry, see Fig. 12 in Šujan et al. (submitted).

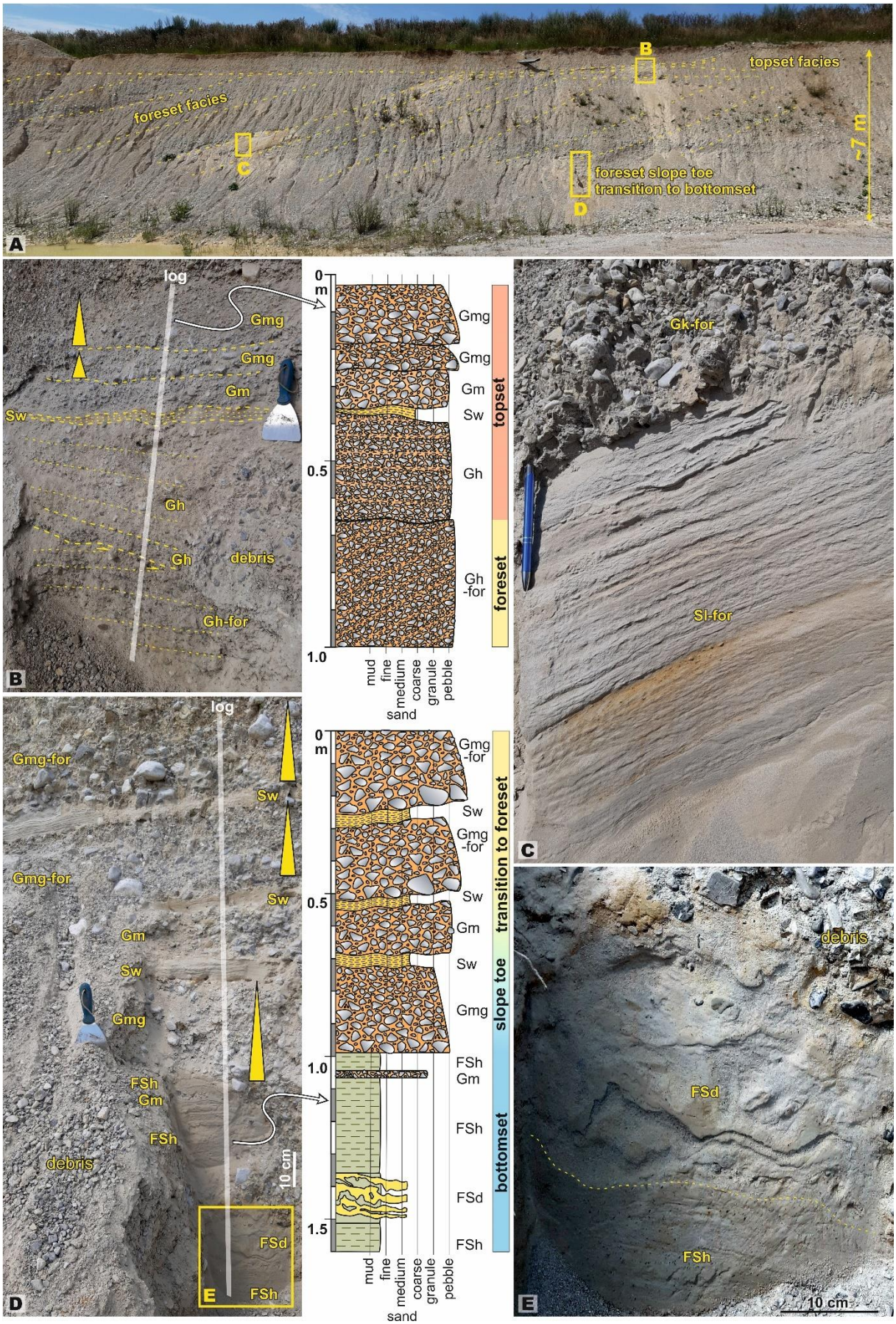
A
B
topset facies
foreset facies
C
foreset slope toe
transition to bottomset
D
~7 m
log
Gmg
Gmg
Gm
Sw
Gh
Gh
debris
Gh-for
B
0
m
0.5
1.0
Gmg
Gmg
Gm
Sw
Gh
Gh
-for
topset
foreset
mud
fine
medium
coarse
granule
pebble
sand
Gk-for
Sl-for
C
log
Gmg-for
Sw
Gmg-for
Sw
Gm
Sw
Gmg
FSh
Gm
FSh
debris
10 cm
FSd
E
FSh
D
0
m
0.5
1.0
1.5
Gmg
-for
Sw
Gmg
-for
Sw
Gm
Sw
Gmg
FSh
Gm
FSh
FSd
FSh
transition to foreset
slope toe
bottomset
mud
fine
medium
coarse
granule
pebble
sand
debris
FSd
FSh
E
10 cm

623

Fig. 7. Outcrops of the Blažovce site showing mainly the facies sub-association FA3b (foreset) of a fan delta. (A, B) Note the transition from subhorizontal topset facies to the below-lying ca. 7 m thick inclined foresets formed by gravels and sands (C), which decrease the slope angle at the point of contact with bottomset sandy and muddy facies (D), including beds deformed by slumping (E). For location within the quarry, see Fig. 12 in Šujan et al. (submitted).

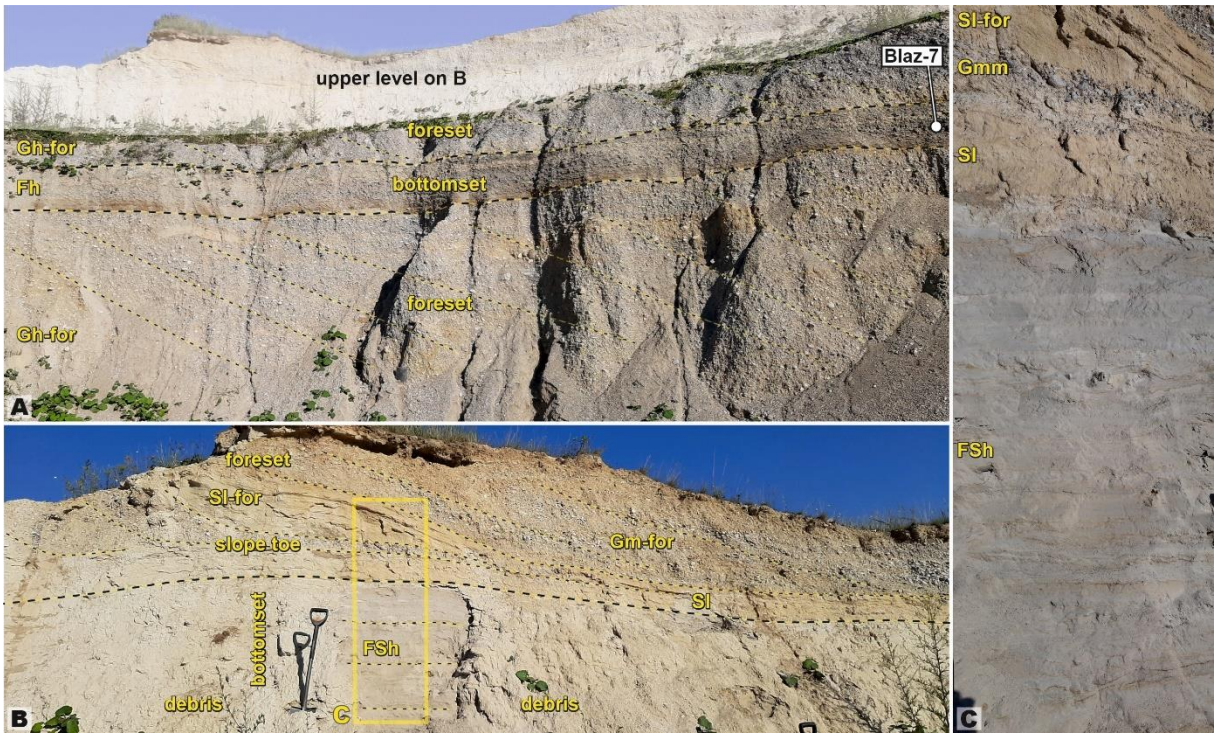

Fig. 8. Outcrops of the Blažovce site showing facies sub-associations FA3b (foreset) and FA3c (bottomset) of a fan delta. (A) Note the sharp angular contact between foreset and bottomset facies. (B) Alternatively, a tangential transition from foreset to bottomset facies was observed. (C) Grain size contrast between bottomset sandy muds and foreset sands and gravels. For location within the quarry, see Fig. 12 in Šujan et al. (submitted).

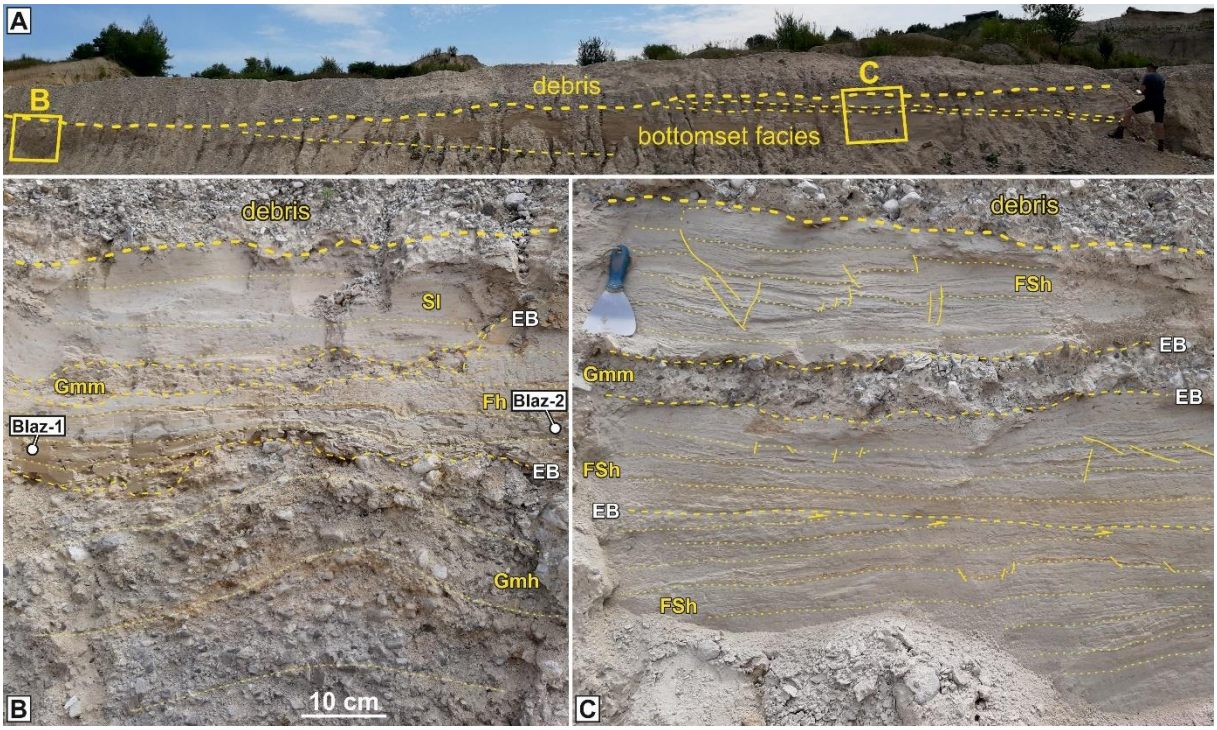

Fig. 9. Outcrops of the Blažovce site showing facies sub-association FA3c (bottomset) of a fan delta. (A) The subhorizontal beds include layers of sands, muddy sands and muds, frequently deformed by compactional small-scale faults associated with loading, which alternate with gravelly layers (B, C). For location within the quarry, see Fig. 12 in Šujan et al. (submitted).

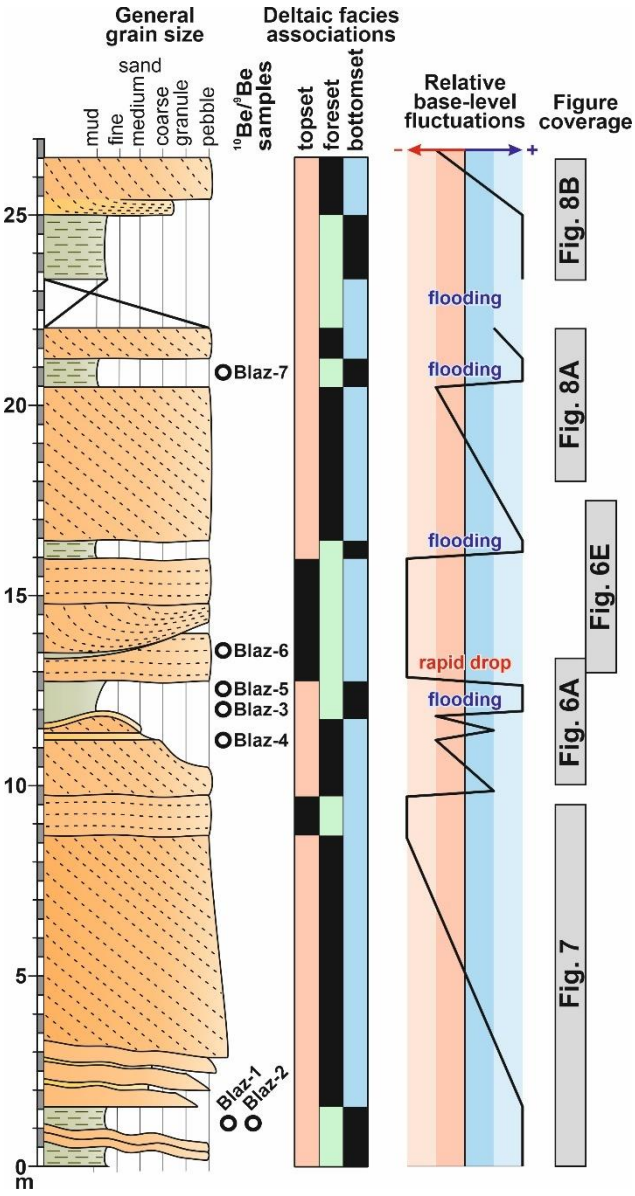

643

644 Fig. 10. Synthetic generalized log of the Blažovce stratigraphic section, including
645 interpretation of the water level changes based on the variation between topset,
646 foreset and bottomset facies, as well as on the thickness of individual foresets.

647 **Interpretation:**

648 The topset facies FA3a are dominated by deposition from (1) a very shallow traction current of
649 sheet flow, forming the horizontal gravelly beds of lithofacies Gh (Blikra and Nemec, 1998;
650 North and Davidson, 2012), and by (2) a bar in a channel a few meters deep, prograding trough
651 deposition from a confined traction current (Boothroyd and Ashley, 1975; Nemec and Postma,
652 1993; Gobo et al., 2015; Martini et al., 2017) (Table 1). Less frequent deposition appeared from

subaerial gravity currents, either as a hyperconcentrated flow forming the Gmg lithofacies (Pierson and Costa, 1987; Brenna et al., 2020), or as a debris flow leading to the accumulation of the Gm lithofacies (Nemec and Steel, 1984; Pierson and Costa, 1987; Brenna et al., 2020). A relatively infrequent deposition appeared as suspension fallout from a supercritical traction current forming the wavy laminated sands of the Sw lithofacies (Fielding, 2006; Cartigny et al., 2014).

The presence of the foreset slope significantly affected the range of depositional processes, which were dominated by gravity currents. The Gh-for lithofacies, composed of inclined gravelly clast-supported beds, represents the result of a stratified high-density turbidity current, while the diagnostic criterion for its subcritical nature is the overall absence of backset (antidune or cyclic step) geometry (Postma and Cartigny, 2014) (Table 1). Increased concentration of clasts in a sediment-water mixture led to the occurrence of hyperconcentrated flows depositing the Gmg-for lithofacies (Mulder and Alexander, 2001; Talling et al., 2012) and grain flows forming the Gk-for lithofacies (Lowe, 1976; Nemec and Steel, 1984; Mulder and Alexander, 2001). Overall, a lower concentration of sediment and prevailing sandy fraction during floods resulted in low-density subcritical turbidity currents (Postma and Cartigny, 2014), or hyperpycnal flows (Mulder et al., 2003), and formed the stratified sands of lithofacies Sl-for.

The transition of the foreset towards the bottomset on the slope-toe comprises a significant reduction of slope angle, which caused a decrease in the inertia of gravity flows. Hence, the high sediment-concentrated gravity flows did not reach far toward the basin floor and formed a significantly lower proportion of the bottomset succession in comparison to the foreset strata. These gravity flows are represented by the stratified subcritical high-density turbidity currents of the Gmh lithofacies (Postma and Cartigny, 2014) as well as the Gmm lithofacies, formed by hyperconcentrated flows (Mulder and Alexander, 2001) or non-cohesive debris flows (Talling et al., 2012) (Table 1). The bottomset succession is dominated by the lithofacies FSh and SFh,

678 associated with low-density subcritical turbidity currents (Postma and Cartigny, 2014) or
679 hyperpycnal flows (Benvenuti, 2003; Mulder et al., 2003), which persisted with much higher
680 inertia after reaching the slope-toe in comparison to the coarse-grained gravity currents and
681 proceeded towards the bottomset (Olariu et al., 2010). The occasional presence of the wavy
682 laminated sands of the Sw lithofacies implies the occurrence of a supercritical low-density
683 turbidity current (Postma and Cartigny, 2014). The massive muds of the Fm lithofacies may
684 reasonably be expected to have been formed by deposition from suspension from a standing
685 water column or a waning flow with a high mud concentration (Baas et al., 2016). Laminated
686 muddy strata (Fh) are considered to be a result of slow traction currents (Allen, 1982; Yawar
687 and Schieber, 2017). The gravity-current origin of the Fh, FSh and Fm muddy lithofacies is also
688 implied by their poor sorting (Table 5 in Šujan et al., submitted).

689 The association of facies described here implies the depositional environment of a fan delta
690 (e.g., Nemec and Steel, 1984; Benvenuti, 2003; Longhitano, 2008; Budai et al., 2021). The
691 depth of the water column changed through time, as illustrated in the synthetic generalized log
692 in Fig. 10, reaching 0.5–7 m according to the clinoform heights. The changes in water level
693 were likely associated with the filling of the accommodation space by a fan delta progradation
694 and repeated floodings, with a base-level rise in the order of 1–5 m, which appeared at least
695 four times in the observed depositional record. Hence, the foresets reaching only 0.5–1.0 m may
696 represent a mouth bar rather than a fully developed fan delta slope (Benvenuti, 2003).
697 Furthermore, a water-level drop was observed in the 12.75 m of the stratigraphic log, recorded
698 by a change from bottomset facies directly to topset (Fig. 10). The gravelly bottomset strata
699 exhibit frequent undulation, while muddy strata are deformed by small-scale blind faults.
700 Additionally, sandy-muddy horizons deformed by slumping were observed. All these features
701 represent the common result of mass wasting on a fan delta foreset-to-bottomset transition and
702 loading related to fan delta progradation (Postma, 1984; McConnico and Bassett, 2007;

703 Longhitano, 2008). Peak discharges during floods were likely associated with foreset deposition
704 from turbidity currents, while grain flow and debris flow processes were perhaps triggered by
705 a delta brink failure (Gobo et al., 2015). The abandonment of the shallow foreset seen in Fig.
706 6A, which is overlaid by massive bottomset muds accumulated by suspension fallout from a
707 calm water column, was likely related to the autogenic lateral migration of a delta lobe (Van
708 Dijk et al., 2009; Paola, 2016; Hajek and Straub, 2017). The clast lithology and rounding of the
709 fan delta facies are very similar to what was observed in the case of alluvial fan facies (Figs. 7–
710 10 in Šujan et al., submitted), implying that these environments once comprised the sediment-
711 feeder components of a single source-to-sink system.

712 **4.1.4 FA4: Open lake deposits**

713 **Description:**

714 The outcrops of the Martin Formation available for study are small exposures providing only a
715 point-like qualitative sedimentological insights. The muddy succession of the Martin Formation
716 was defined based on fossil fauna and observations from the Martin claypit, along with the
717 cores of boreholes drilled in the Turiec Basin (Pipík, 2004; Kováč et al., 2011; Pipík et al.,
718 2012; Neubauer et al., 2015). However, the originally >20 m high outcrop of the claypit is now
719 covered by a landfill, and only a 1.2 m thick section in a nearby gully remains exposed and
720 therefore available to study (Figs. 1C, 11A, Fig. 14 in Šujan et al., submitted). The facies are
721 dominated by mud, sandy mud, and muddy sand. It is most commonly massive, with preserved
722 bioturbation marks, and articulated mollusc shells appear in it (Fmb, SFmb lithofacies) (Fig.
723 11B–D). The sandy mud or muddy sand appears also as horizontally laminated lithofacies, the
724 FSh and SFh. Muddy sand with lamination including concave and convex geometry, forming
725 lenses few centimeters thick divided by erosional surfaces also of concave and convex shapes
726 was observed; this resembles hummocky-cross stratification (SFhc; Fig. 11C). Another horizon
727 of muddy sand includes unidirectional ripple-cross stratification of the lithofacies SFr (Fig.

11B). The lithological boundaries are either smooth and transitional or sharp and bioturbated (Fig. 11B-D). A vertical change along the section from massive to more stratified and more coarse-grained strata is evident (Fig. 11A).

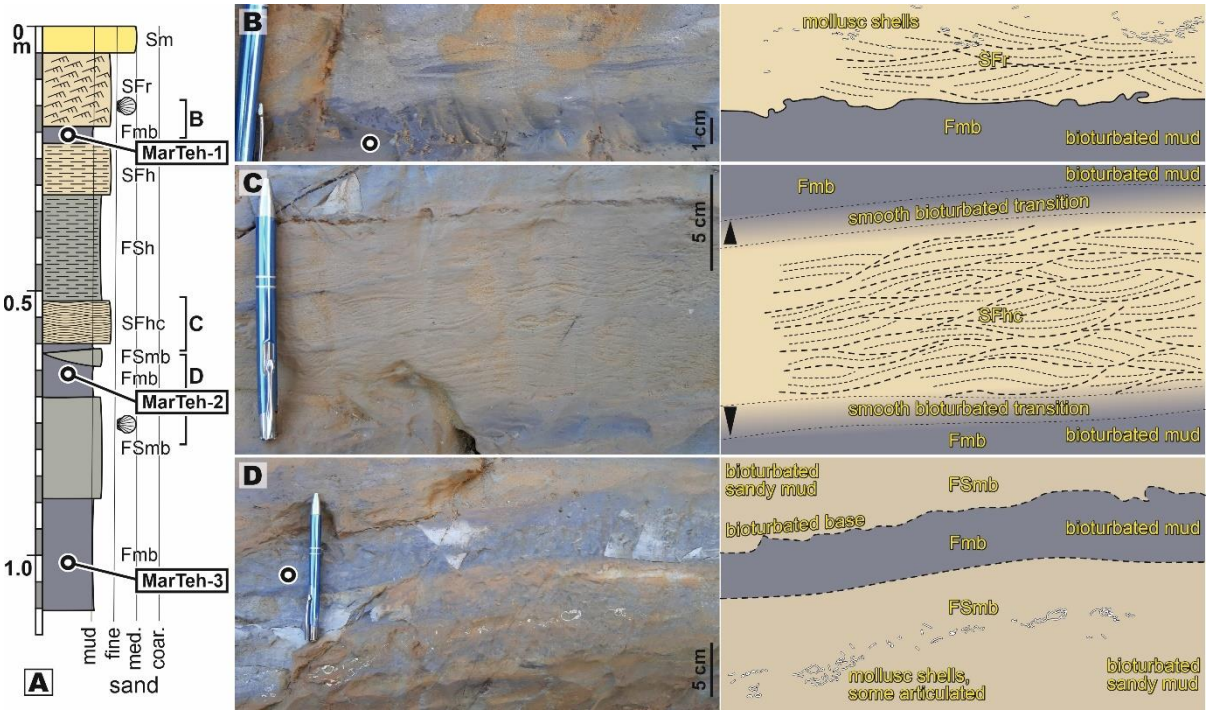

Fig. 11. Outcrop located in a gully nearby the Martin claypit, exposing the open lacustrine facies of the Martin Formation. Correlation to the original section of Pipík (2004) in Fig. 14 of Šujan et al. (submitted). Location in Fig. 1C.

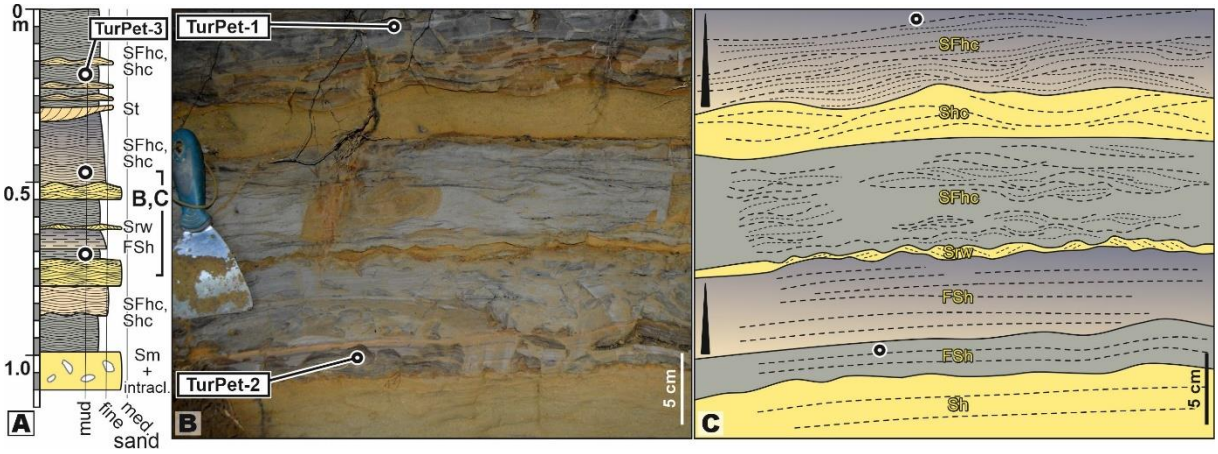

Fig. 12. Outcrop located in a river cut near Turčiansky Peter, exposing the open lacustrine facies of the Martin Formation. Location in Fig. 1C.

Another small area of exposure of the Martin Formation was documented in the cut of the riverbank near Turčiansky Peter (Figs. 1C, 12A). The lithological boundaries of the muddy sand, sandy mud and sandy strata are sharp and erosional. The dominant lithofacies of sand and muddy sand attain concave and convex geometry of lamination with internal erosional surfaces typical of hummocky-cross stratification (SFhc, Shc; Fig. 12B, C). Horizontally laminated sandy mud of the lithofacies FSh appears less frequently, together with occasional symmetrical sandy ripples (Srw) and trough cross-stratified sands (St) (Fig. 12). Massive sand with muddy intraclasts of the Sm lithofacies was also observed.

The last exposure of the Martin Formation included in this study is present in a cut of a small creek called Kúdel near Turčianske Kľačany (Fig. 1C, Fig. 15 in Šujan et al., submitted). The outcrop exposes massive grey mud, covered by a subrecent accumulation from the creek and by recent soil.

Interpretation:

Massive muds of the Fmb lithofacies do not have preserved primary structures, likely due to extensive bioturbation; their deposition by suspension settling from a calm water column (Potter et al., 1980; Potter et al., 2005) or by slowly flowing traction currents could nevertheless be expected (Yawar and Schieber, 2017). Laminated muds and sandy muds of the Fh and FSh lithofacies are interpreted as deposits of slow traction currents (Yawar and Schieber, 2017), hyperpycnal flows (Mulder et al., 2003) or distal low-density turbidity currents (Postma and Cartigny, 2014; Boulesteix et al., 2019). Hummocky cross-stratification is considered to be a result of deposition from storm wave oscillatory traction currents (Dumas and Arnott, 2006; Jelby et al., 2020). Unidirectional traction currents formed a minor proportion of the successions studied, either as ripples (SFr) or as subaqueous dunes of the St lithofacies (Allen, 1982; Leclair and Bridge, 2001). Calm-weather oscillatory flow forming symmetrical ripples also appeared (Dumas et al., 2005; Amoudry et al., 2013). This association of depositional processes implies

763 an open basin environment affected by temporally variable siliciclastic input from a river delta
764 and by wave reworking of sediment (Table 2). The Martin – claypit succession formed under
765 the influence of a much-reduced regime of wave activity compared to the Turčiansky Peter site.

766 4.2 Stratigraphy based on borehole correlation

767 The facies associations (FA) defined on outcrops were correlated using the lithological profiles
768 of boreholes (Fig. 13). The distinguishing criteria included in Table 2 of Šujan et al. (submitted)
769 allowed only the correlation of (1) FA1: Alluvial fan, (2) FA4: Open lake, and (3) FA2 & FA3:
770 In terms of the accuracy of the lithological descriptions, a braided river together with a fan
771 delta, was not detailed enough to distinguish FA2 and FA3 definitively. The blocky pattern of
772 the basin syn- and post-depositional deformation leads to frequent fault contact in FA. The
773 sections show the areas along the southern depocenter and along the northern depocenter
774 separately (Figs. 1C, 13F, G).

775 A clear spatial trend in the FA distribution could be seen in the section along the Slovany and
776 Socovce sites (Fig. 13A), with the transition from alluvial fan deposits occurring in the
777 northwest towards a braided river/fan delta FA, and with the dominance of open lake strata in
778 the main depocenter and the southeast. Section B, across the Abramová site, shows only the
779 first braided river/fan delta deposits, some tens of meters thick, below the present surface (Fig.
780 13B). A lateral transition from FA1 to FA2 & FA3 and finally to FA4 proceeding west to east
781 is documented in section C along the Ondrašová and Blažovce sites (Fig. 13C), similarly to
782 section A (Fig. 13A). The perpendicular section D solely reveals the transition from FA1 to
783 FA2 & FA3 from north to south (Fig. 13D). This spatial pattern implies sourcing of sediment
784 from the northwest towards the southeast.

785 The northern area (Fig. 13G) is investigated by the section E along the Valča, Turčiansky Peter,
786 and Martin – claypit outcrops (Fig. 13E). The spatial distribution of lithotypes shows the

787 dominance of alluvial fan deposits in the south, divided by a fault from an area of patchy
788 presence of the braided river/fan delta FA interfingering with the open lacustrine strata. Section
789 E indicates a southern position for the clastic sediment source.

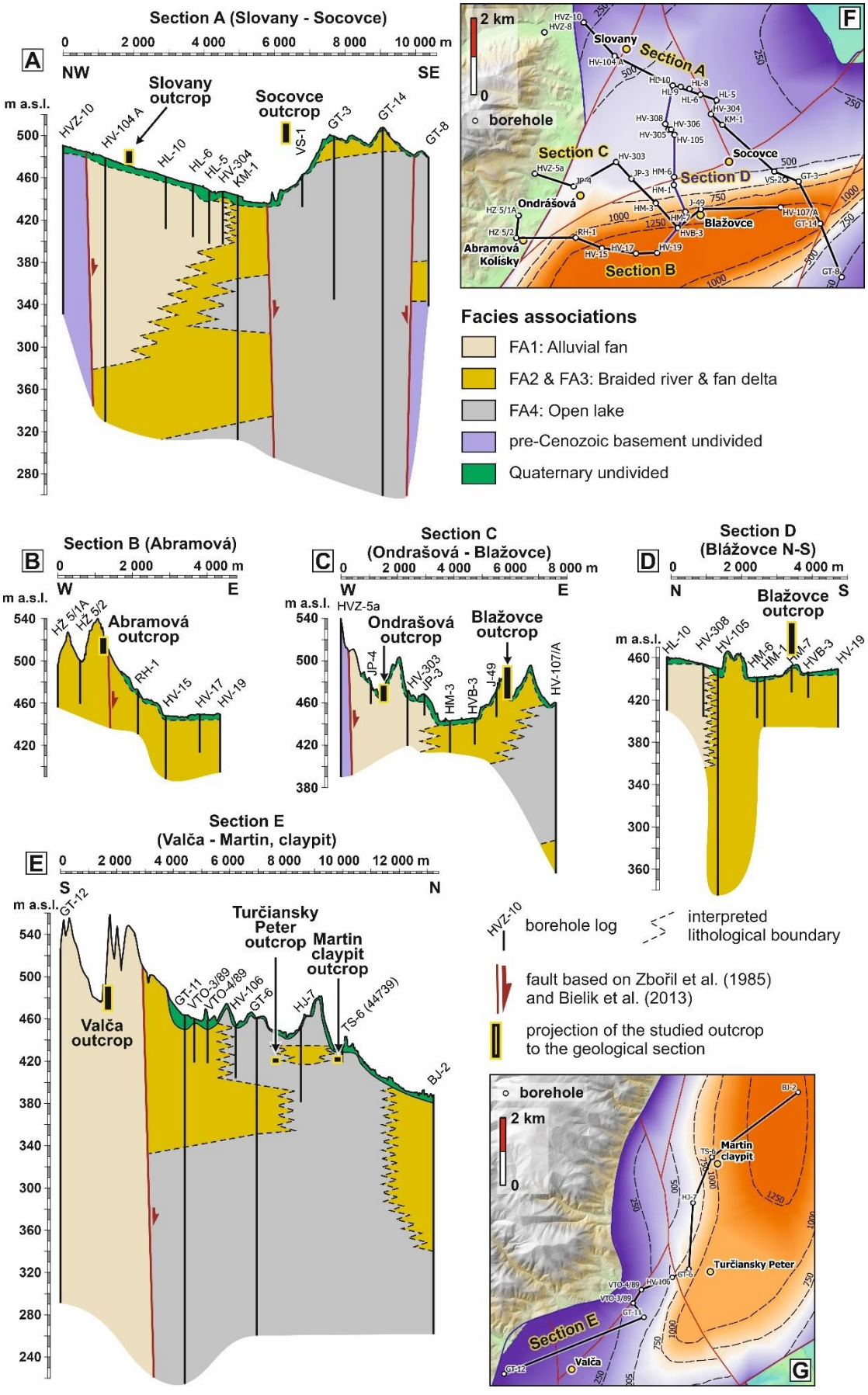
Section A (Slovany - Socovce)
A
NW
SE
m a.s.l.
Slovany outcrop
Socovce outcrop
HVZ-10
HV-104 A
HL-10
HL-6
HL-5
HV-304
KM-1
VS-1
GT-3
GT-14
GT-8
F
2 km
0
borehole
Slovany
Section A
Section C
Section D
Socovce
Ondrášová
Blažovce
Abramová
Kolísky
Section B
Facies associations
FA1: Alluvial fan
FA2 & FA3: Braided river & fan delta
FA4: Open lake
pre-Cenozoic basement undivided
Quaternary undivided
B
Section B (Abramová)
W
E
HZ 5/1A
HZ 5/2
Abramová outcrop
RH-1
HV-15
HV-17
HV-19
C
Section C (Ondrašová - Blažovce)
HVZ-5a
Ondrašová outcrop
Blažovce outcrop
JP-4
HV-303
JP-3
HM-3
HVB-3
J-49
HV-107/A
D
Section D (Blážovce N-S)
N
S
Blažovce outcrop
HL-10
HV-308
HV-105
HM-6
HM-1
HM-7
HVB-3
HV-19
E
Section E (Valča - Martin, claypit)
Valča outcrop
GT-12
GT-11
VTO-3/89
VTO-4/89
HV-106
GT-6
HJ-7
Turčiansky Peter outcrop
Martin claypit outcrop
TS-6 (44739)
BJ-2
borehole log
interpreted lithological boundary
fault based on Zbořil et al. (1985) and Bielik et al. (2013)
projection of the studied outcrop to the geological section
G
Martin claypit
Turčiansky Peter
Section E
Valča

790

Fig. 13. Generalized geological sections showing the distribution of facies associations across the Turiec Basin, as defined on outcrops. The locations on the maps and explanations may be seen in Fig. 1C. Detailed versions of the sections, including borehole lithological logs, are included in Figs. 3–5 of Šujan et al. (submitted). References for the specific borehole data are included in Table 1 of Šujan et al. (submitted).

Temporal trends recorded in vertical changes in FA distribution are less well-imaged due to the restricted thickness of the stratigraphic column penetrated by the boreholes. Nevertheless, a change upwards from FA2 & FA3 to FA1 is shown in borehole HV-104 A (section A), as well as a vertical transition from FA4 to FA2 & FA3 in boreholes KM-1, GT-3 and GT-14 (Fig. 13A). Changes upwards from open lake to braided river/fan delta FA are documented by section E in boreholes GT-11, GT-3, HJ-7 and BJ-2 (Fig. 13E). Generally, the observed pattern of vertical (temporal) changes of FA could be interpreted as a progradation of the alluvial fan-braided river-fan delta depositional system towards the open lake environment, despite the high-frequency fluctuations of the base level observed on the outcrop scale (Fig 10).

4.3 Geochemistry and mineralogy

The XRF whole rock analyses of mud to sandy mud from alluvial fans (ValLom1, Ondr-1) are characterized by a high proportion of CaO (32–37 wt. %), MgO (14 wt. %), and a low oxide sum (63–67 wt. %) (Fig. 14, Table 6 in Šujan et al., submitted). This indicates a high proportion of carbonate minerals in the composition of the mud, and this is further confirmed by XRD analysis, indicating a 77–78 % dominance of dolomite in whole rock composition (Table 3). The low content of silicate minerals is shown by the amount of Al_2O_3 (2.7–5.6 wt. %), and SiO_2 (5.9–11.4 wt. %) (Fig. 14, Table 6 in Šujan et al., submitted). The Si/Al ratio (1.9) and K_2O/Al_2O_3 (0.15–0.18) point to the high content of clay minerals in the silicate fraction. This is consistent with XRD data (Quartz 5°%; phyllosilicates 17–18°%; Table 3), in which the clay fraction in Ondr-1 is dominated by illite, and both samples contain subordinate quantities of

817 smectite and kaolinite. Samples also display a low content of Fe (0.4–0.6 wt.°% Fe_2O_3). The
818 content of Fe is important due to the binding of Be. Considering the whole dataset, the amount
819 of Fe is lowest in alluvial fan samples, although $Fe_{(ef)}$ varies from 0.2–0.7 (Table 7 in Šujan et
820 al., submitted).

821 Samples from braided river mud to sandy mud (Kolísky-3, SocKos-1) document a small
822 increase in the proportion of siliciclastic material (SiO_2 16–18 wt. %; Al_2O_3 6–8 wt. %) (Fig.
823 14, Table 6 in Šujan et al., submitted). The Si/Al (2.4–2.7) and K_2O/Al_2O_3 (0.14–0.21) proxies
824 point to a lower content of clay (so, more silty grains) in the silicate fraction compared to the
825 alluvial fan samples. The content of CaO (33–49 wt. %) and MgO (6 wt. %) shows a slight
826 decrease in carbonate minerals and an increase in the calcite portion in comparison to alluvial
827 fan samples. This agrees with the XRD analysis, which indicates a composition of 56–69 %
828 carbonate minerals; 20–27 % phyllosilicates and 4 % quartz. The clay fraction is dominated by
829 smectite and illite/smectite. The content of Fe_2O_3 is 2.2 wt. %, and that of $Fe_{(ef)}$ is 0.9–1.2 wt. %,
830 which indicates an increase in Fe content compared to the alluvial fan.

831 The fan-delta mud to sandy mud of the Blaz-3 sample, as measured by XRF displays a further
832 continual decreasing of carbonate content (CaO 20.7 wt. %; MgO 5.8 wt. %), accompanied by
833 an increase in the silicate fraction (SiO_2 24.45 wt. %; Al_2O_3 11.8 wt. %) (Fig. 14; Table 6 in
834 Šujan et al., submitted). Si/Al (1.8) and K_2O/Al_2O_3 (0.15) are similar to those in braided rivers
835 (Table 7 in Šujan et al., submitted). In mineral composition, carbonate minerals form only 43 %,
836 with the remainder being made up of phyllosilicates 48 % and quartz 9 % (Table 3). The clay
837 fraction is dominated by smectite.

838 More detailed mud analyses using ICP-MS and ICP ES were performed on the Blažovce section
839 samples taken from several levels (Table 8 in Šujan et al., submitted; Fig. 10). These data
840 document that the Blaz-1,2,3 samples have a lower content of carbonates (CO_2 16.2–17.8
841 wt. %) than the Blaz-5 and Blaz-7 samples (CO_2 22.6–24.3 wt. %). Meanwhile, the silicate

materials display an opposite trend, in which Blaz-1,2,3 yield figures of 29.4–32.6 wt. % SiO_2 and 14.3–17 wt. % Al_2O_3, with Blaz-5 and Blaz-7 on 23.7–28.8 wt. % SiO_2 and 10.4–11.1 wt. % Al_2O_3 (Fig. 14, Table 8 in Šujan et al., submitted). The Si/Al ratio increases from Blaz-1 (1.8) to Blaz-7 (2.2), a phenomenon which pointed to a decrease in the clay proportion from the Blaz-1 to Blaz-7 samples. The lowermost K_2O/Al_2O_3 (illite proxy) is present in Blaz-5 (0.12), and the highest value (0.18) is in found in Blaz-7. These values are confirmed also by the CIA index and Rb (Table 9 in Šujan et al., submitted). This may be explained by a higher content of sandy/silty grains in Blaz-7. The content of Fe_2O_3 is highest in Blaz-1 and 2 (4.2–4.6 wt. %; $Fe_{(ef)}$ 0.9) and in Blaz-3,5,7 decreases from 2.7 to 1.8 wt. % ($Fe_{(ef)}$ 0.6–0.5), respectively.

The open lake mud to muddy sand (MarTeh-1; TurPet-1; Kudel-1) has the lowest proportion of carbonates (CaO = 5.2–8.5 wt. %; MgO 2.0–2.1 wt. %, Fig. 14, Table 6 in Šujan et al., submitted) and the highest proportion of silicate fraction in its composition (SiO_2 33.5–37.4 wt. %; Al_2O_3 8.9–12.4 wt. %). The Si/Al (2.7–3.3) and K_2O/Al_2O_3 (0.22–0.23) ratios imply that the clay mineral proportion in the silicate fraction is relatively low in comparison with the samples previously described. Kudel-1 probably contains the largest portion of sandy grains (Si/Al 3.3) and carbonate minerals (CaO 8.5 wt. %) of any of the open lake sites; the open lake samples contain 2.0–3.2 wt. % Fe_2O_3 ($Fe_{(ef)}$ 0.6–0.8). These data are consistent with the XRF analysis (MarTeh-1; Tur-Pet-1), in which phyllosilicates comprise 52–53 %, quartz 32–35 % and carbonate minerals 8–16 %. The clay fraction contains approximately the same proportion of illite and smectite, together with a subordinate amount of quartz, chlorite, and kaolinite (Table 3). The results of both analyses document that: (1) these mudstones are siliciclastic; and (2) probably contain the highest proportion of sandy/silty grains of all the measured samples.

Table 3. Quantitative mineral composition of whole rock sample and semi-quantitative mineral composition of the <2 μm fraction obtained by XRD. Phyllosilicate content was determined in the <2 μm fraction of insoluble rock residue. Qz – quartz; Pl – plagioclase; Cal – Calcite; Dol – dolomite; L.c.Vrm – low charge vermiculite/high charge smectite; Vrm – vermiculite; Ilt – illite; Sme – smectite; Sme + S-I – smectite and mixed

layer illite-smectite; Kln – kaolinite which does not intercalate with DMSO; KlnD – kaolinite which forms intercalation compounds with DMSO; Chl – chlorite; Chl-S – mixed layer Chlorite – smectite; XXX – dominant (>50 %); XX – abundant (20–50 %); X – subordinate (1–20 %); + - traces (<1%), ? - mineral is probably present in the sample.

sample	Environment	whole rock					fraction < 2 μm										
		Qz	Pl	Cal	Dol	phyllo-silicates	L.c. Vrm	Vrm	Ilt	Sme	Sme + I-S	Kln	KlnD	Chl	Chl-S	Qz	Dol
MarTeh-1	open lake	32		11	5	52			XX	XX		X	-	X		X	
Tur-Pet-1	open lake	39		8		53		X	XX	XX		X	-	X		X	
Blaz-3	fan delta	9		16	27	48			XX	XXX		X	X	X		X	
SocKos-1	braided river	4		34	35	27		X	X		XXX	X	+			+	X
Kolisky-3	braided river	4		60	16	20			X		XXX	X	X			+	
Ondr-1	alluvial fan	5			78	17	X		XXX	+		X	X			?	X
ValLom-1	alluvial fan	5			77	18		X	XX	X		X	X			-	XX
Vel-Cep-2	alluvial fan	26	7			67			XX		XX	X	X		X	X	
Kost-Q-1	floodplain	31	5		38	26			XX		XXX	X	-	X		X	
Kalam-Q-1	floodplain	40	5			55			XX		X	XX	X	X		X	
MalCep-3	river terrace	34	8		35	23			XX	XX		X	-			X	

Four samples taken from initial ratio sites of Late Pleistocene to Holocene age were also analysed using XRF and XRD (MalCep-3; VelCep-2; Kalam-Q-1; Kost-Q-1). The samples vary in their content of carbonate minerals, over a range of 0–35 %, which is offset by an increase in the content of 23–67 % in phyllosilicates and 26–40 % in quartz (Table 3). The content of Fe_2O_3 (3–5 wt. %), $Fe_{(ef)}$ (0.7–1.3), Si/Al (2.2–3.1), and K_2O/Al_2O_3 (0.11–0.19) is similar to open lake samples (Table 7 in Šujan et al., submitted). From these samples, Vel-Cep-2 displayed the highest content of clay fraction (Si/Al 2.22; 67 % phyllosilicates) and $Al_{(UCC)}$ 1.05 (Table 3, Table 7 in Šujan et al., submitted). On the other hand, the clay fraction of VelCep-2 and MalCep-3 consists of approximately the same proportion of illitic material and smectite or mixed layer illite/smectite. KOS-Q-1 is dominated by smectite and illite/smectite; while Kalam-Q-1 contains an increased proportion of kaolinite.

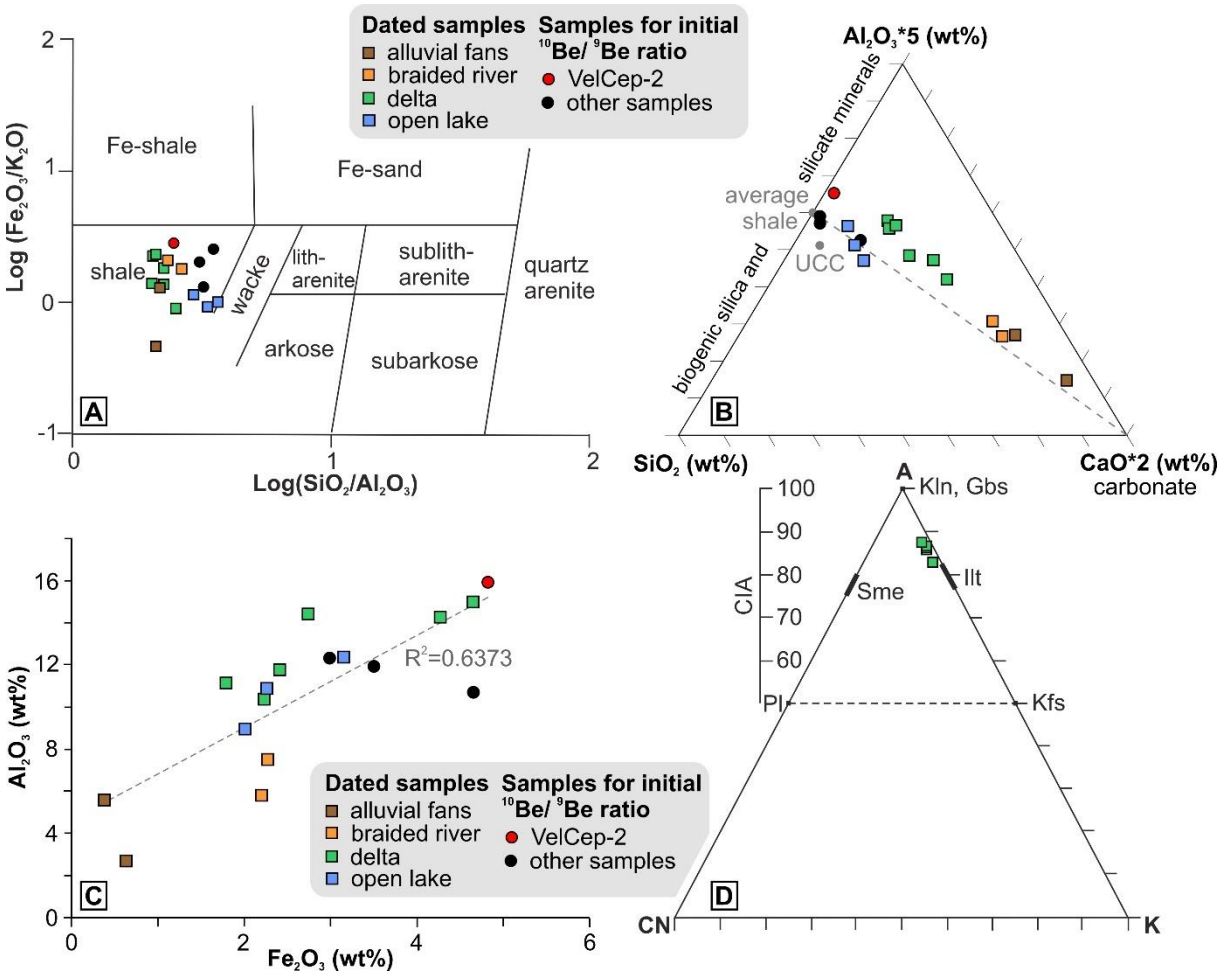

Fig. 14. Geochemical characterization of the samples selected from dated sites and sites evaluated for determination of the initial $^{10}Be/^{9}Be$ ratio. A. Classification of muddy samples according to Herron (1988). B. Composition of mud according to Brumsack (1989) shows a continuous decrease of carbonate component from alluvial fans towards the open lake environment. C. Relationship between Al_2O_3 and $Fe_2O_{3\ (tot)}$, showing an increase in Fe together with the siliciclastic fraction in the samples analysed. D. A-CN-K diagram showing degree of weathering in source area (Nesbitt and Young, 1982).

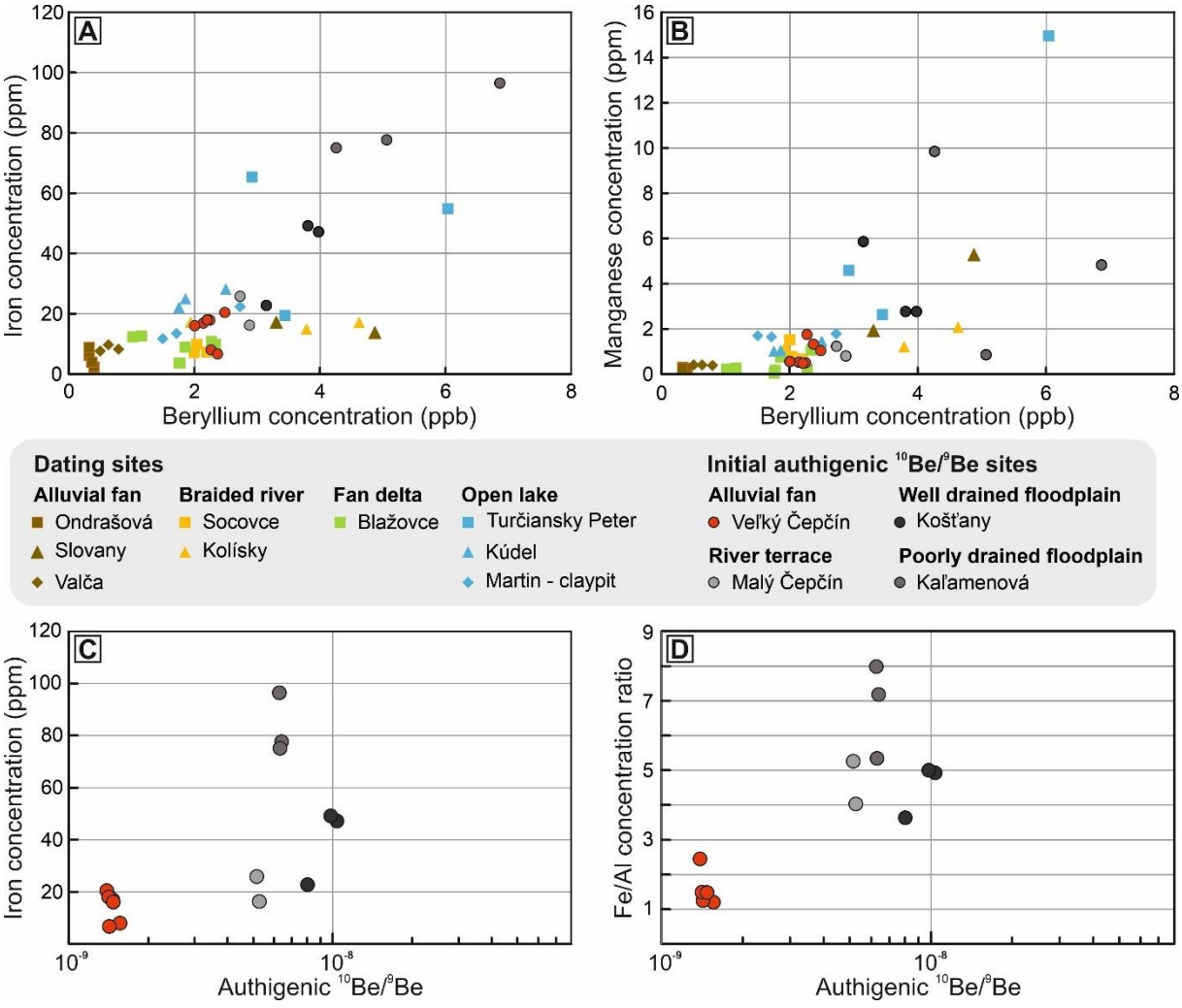

Fig. 15A,B. Concentrations of iron and manganese plotted against the beryllium concentrations in the authigenic phase for all dated samples. Note the divergence of the poorly and well drained floodplain sites (Kaľamenová and Košťany nad Turcom) from the main set of dating site samples, as well as the consistency of the Veľký Čepčín site values with the main set of dating site samples. The measured values are included in Šujan et al. (2022). C,D. Authigenic $^{10}Be/^{9}Be$ of the sites sampled for initial ratio determination plotted against the concentration of iron and Fe/Al ratio.

The increased concentration of iron in the authigenic phase generally correlates with increased authigenic $^{10}Be/^{9}Be$ (C). The different appearance of the sites is evident when concentration of iron is normalized to aluminum (D).

The ICP-MS analyzes of the authigenic phase were mainly focused on the comparison between the main batch of the dating samples of all studied sites and the samples taken from four sites selected for establishment of the authigenic $^{10}Be/^{9}Be$ initial ratio (Veľký Čepčín, Malý Čepčín, Košťany, Kaľamenová). The plots of beryllium concentrations against iron and manganese show a relatively homogeneous set of almost all samples of the dating sites (except for the Turčiansky Peter site) (Fig. 15). When taking into account the sites selected for initial $^{10}Be/^{9}Be$ ratio determination, a significant deviation of the floodplain samples taken from Kaľamenová and Košťany nad Turcom with correlating increased concentrations of Be and Fe could be established (Fig. 15A). Moreover, the values of Be against Mn concentrations show a similar but not so pronounced pattern. The Veľký Čepčín site appears to be consistent with the main set of dating samples (Fig. 15B).

4.4 Authigenic $^{10}Be/^{9}Be$ dating

4.4.1 Initial $^{10}Be/^{9}Be$ ratios

The authigenic $^{10}Be/^{9}Be$ ratios calculated for the initial ratio samples range from $143.36 \pm 1.41 \times 10^{-11}$ to $1007.56 \pm 16.78 \times 10^{-11}$ (Table 5, Fig. 16). Despite this difference of one order of magnitude, the variability of values within each site is low, except for at the Košťany nad Turcom site, where sample Kost-Q-1 was considered an outlier. Sample VelCep-1 was also considered an outlier during the calculation of weighted mean isotopic ratios using the KDX application by Spencer et al. (2017). The low degree of within-site variability allowed us to calculate weighted mean isotopic ratios for each site in the range of 143.40×10^{-11} to $1007.78 \pm 16.78 \times 10^{-11}$ (Table 5). The weighted mean values obtained from the four analyzed sites are used for age calculations as the initial authigenic $^{10}Be/^{9}Be$ ratio.

925 Table 5: Concentrations of ^{9}Be and ^{10}Be, natural $^{10}Be/^{9}Be$ ratios and weighted mean initial ratios (N_0) determined in the Turiec Basin from
926 Late Pleistocene and Holocene localities. Uncertainties are σ_1. Concentrations of ^{10}Be are corrected to the $^{10}Be/^{9}Be$ ratios of eight processing
927 blanks reaching values in the range of 6.61×10^{-15} to 9.62×10^{-15}. * - Values considered as outliers (see text).

ID	Locality	^{9}Be (at × g^{-1}) × 10^{16}	AMS $^{10}Be/^{9}Be$ (× 10^{-14})	^{10}Be (at × g^{-1}) × 10^{6}	Natural $^{10}Be/^{9}Be$ (× 10^{-11})	Weighted mean initial $^{10}Be/^{9}Be$ ratio (× 10^{-11})
VelCep-1*	Veľký Čepčín - Late Pleistocene alluvial fan	5.232 ± 0.105	265.832 ± 4.141	81.654 ± 1.272	156.071 ± 3.957	143.36 ± 1.41
VelCep-2		5.817 ± 0.116	270.068 ± 4.369	82.750 ± 1.339	142.252 ± 3.659	
VelCep-3		6.448 ± 0.129	297.820 ± 4.693	89.708 ± 1.414	139.127 ± 3.543	
VelCep-4		6.237 ± 0.128	292.480 ± 3.601	89.165 ± 1.099	142.970 ± 3.358	
VelCep-5		6.003 ± 0.123	289.256 ± 3.545	88.146 ± 1.081	146.835 ± 3.444	
VelCep-6		6.365 ± 0.131	293.137 ± 3.627	90.023 ± 1.115	141.434 ± 3.326	
VelCep-7		5.443 ± 0.111	261.065 ± 3.246	80.249 ± 0.998	147.407 ± 3.471	
MalCep-3	Malý Čepčín - Late Pleistocene river terrace	6.725 ± 0.134	1155.94 ± 14.491	354.221 ± 4.441	526.744 ± 12.433	520.92 ± 8.69
MalCep-4		6.176 ± 0.124	1038.65 ± 12.951	318.267 ± 3.969	515.355 ± 12.146	
Kost-Q-1*	Košťany - Holocene Turiec River floodplain	7.715 ± 0.154	2026.705 ± 25.274	619.064 ± 7.72	802.433 ± 18.913	1007.56 ± 16.78
Kost-Q-2		9.339 ± 0.187	3264.765 ± 40.719	968.803 ± 12.083	1037.41 ± 24.452	
Kost-Q-3		8.664 ± 0.173	2759.251 ± 34.2	849.941 ± 10.535	980.968 ± 23.082	
Kalam-Q-1	Kalamová - Holocene Turiec River floodplain	11.193 ± 0.224	2342.33 ± 29.157	715.313 ± 8.904	639.047 ± 15.054	632.81 ± 8.61
Kalam-Q-2		9.441 ± 0.189	1980.38 ± 24.796	596.148 ± 7.464	631.42 ± 14.899	
Kalam-Q-3		15.606 ± 0.312	3177.1 ± 39.294	980.336 ± 12.125	628.172 ± 14.772	

928

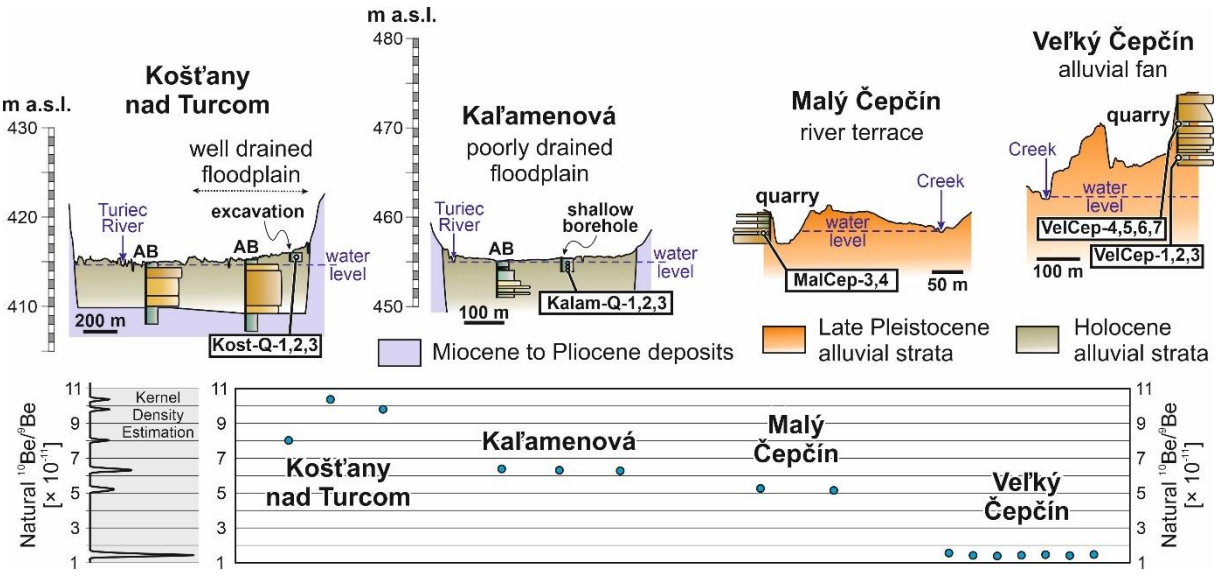

Fig. 16. Geological settings of the sites selected for determination of initial $^{10}Be/^{9}Be$ ratio, and distribution of natural $^{10}Be/^{9}Be$ values for all samples. Error bars are smaller than the symbols. The Kernel Density Estimation was produced by the KDX application (Spencer et al., 2017). Košťany nad Turcom and Kaľamová are sites on the Turiec River floodplain of Holocene age, while Malý Čepčín is a Late Pleistocene river terrace and Veľký Čepčín comprises a Late Pleistocene alluvial fan. The location of the sites may be seen in Fig. 1C. An explanation of the lithological logs is in Fig. 2 of Šujan et al. (submitted). AB – archival borehole lithological profile obtained from the Geofond archive of the State Geological Institute of Dionýz Štúr (Slovak Geological Survey).

4.4.2 Dating results

The authigenic $^{10}Be/^{9}Be$ isotopic ratios of the dating samples range from $0.87 \pm 0.06 \times 10^{-11}$ to $56.62 \pm 1.65 \times 10^{-11}$ (Table 6, Table 10 in Šujan et al., submitted). The depositional ages for all 31 samples using the four initial ratios are included in Table 10 of Šujan et al. (submitted). The age uncertainties propagate from the uncertainty of the corresponding initial ratio, analytical error of measured natural $^{10}Be/^{9}Be$ ratio, and uncertainty in the half-life of ^{10}Be. The within-site variability of $^{10}Be/^{9}Be$ isotopic ratios and calculation of weighted mean ages are further discussed in chapter 5.1, together with the reasoning for the initial ratio selection.

Table 6: Concentrations of ^{9}Be and ^{10}Be, natural $^{10}Be/^{9}Be$ ratios, authigenic $^{10}Be/^{9}Be$ ages for the analyzed samples, calculated using the Veľký Čepčín initial ratio (N_0) and weighted mean ages calculated using the KDX application (Spencer et al., 2017). Uncertainties are σ_1. Concentrations of ^{10}Be are corrected to the $^{10}Be/^{9}Be$ ratios of eight processing blanks reaching values in the range of 6.61×10^{-15} to 9.62×10^{-15}. * - Values considered as outliers (see text).

ID	Locality	Stratigraphy	^{9}Be (at × g^{-1}) × 10^{16}	AMS $^{10}Be/^{9}Be$ (× 10^{-14})	^{10}Be (at × g^{-1}) × 10^{6}	Natural $^{10}Be/^{9}Be$ (× 10^{-11})	Age (Ma) - Veľký Čepčín N_0	Weighted mean age (Ma)
Ondr-1	Ondrašová	Alluvial fan	0.999 ± 0.020	2.372 ± 0.112	0.523 ± 0.030	5.236 ± 0.321	6.624 ± 0.429	n.a.
Ondr-2			0.777 ± 0.016	3.831 ± 0.145	0.970 ± 0.041	12.481 ± 0.581	4.885 ± 0.249	
Ondr-3			0.862 ± 0.017	2.464 ± 0.102	0.548 ± 0.029	6.357 ± 0.356	6.235 ± 0.373	
Ondr-4			0.777 ± 0.016	3.493 ± 0.115	0.860 ± 0.033	11.059 ± 0.482	5.127 ± 0.248	
Slov-1	Slovany		12.743 ± 0.255	36.980 ± 0.891	11.037 ± 0.267	8.662 ± 0.272	5.616 ± 0.211	n.a.
Slov-2			7.678 ± 0.154	46.427 ± 1.224	13.848 ± 0.366	18.036 ± 0.598	4.149 ± 0.162	
ValLom-1	Valča		1.461 ± 0.029	3.866 ± 0.167	0.939 ± 0.045	6.427 ± 0.331	6.214 ± 0.345	6.394 ± 0.195
ValLom-2			1.937 ± 0.039	4.485 ± 0.150	1.114 ± 0.042	5.753 ± 0.243	6.435 ± 0.304	
ValLom-3			1.178 ± 0.024	2.846 ± 0.116	0.640 ± 0.032	5.436 ± 0.294	6.549 ± 0.379	
SocKos-1	Socovce	Braided river - Abramová Mb.	5.079 ± 0.102	9.729 ± 0.309	2.675 ± 0.087	5.267 ± 0.202	6.612 ± 0.288	6.432 ± 0.162
SocKos-2			4.708 ± 0.094	9.605 ± 0.315	2.657 ± 0.089	5.643 ± 0.221	6.474 ± 0.287	
SocKos-3			4.672 ± 0.093	10.536 ± 0.329	2.966 ± 0.095	6.349 ± 0.239	6.238 ± 0.269	
Kolisky-1	Abramová - Kolísky		4.594 ± 0.092	5.205 ± 0.165	1.364 ± 0.047	2.968 ± 0.118	7.759 ± 0.349	7.469 ± 0.231
Kolisky-2*			10.721 ± 0.214	6.790 ± 0.213	1.846 ± 0.060	1.721 ± 0.066	8.849 ± 0.384	
Kolisky-3			8.719 ± 0.174	11.685 ± 0.361	3.348 ± 0.105	3.840 ± 0.142	7.244 ± 0.308	
Blaz-1*	Blažovce	Fan delta - Blažovce Mb.	2.065 ± 0.041	7.888 ± 0.245	2.101 ± 0.068	10.176 ± 0.389	5.294 ± 0.230	6.697 ± 0.135
Blaz-2			2.716 ± 0.054	5.042 ± 0.167	1.228 ± 0.045	4.523 ± 0.190	6.917 ± 0.325	
Blaz-3			4.387 ± 0.088	9.115 ± 0.316	2.508 ± 0.089	5.717 ± 0.233	6.448 ± 0.295	
Blaz-4*			4.076 ± 0.082	75.787 ± 1.620	23.079 ± 0.494	56.622 ± 1.659	1.859 ± 0.067	
Blaz-5			5.418 ± 0.108	11.134 ± 0.391	3.105 ± 0.111	5.731 ± 0.235	6.443 ± 0.296	
Blaz-6			5.187 ± 0.104	6.836 ± 0.212	2.490 ± 0.080	4.800 ± 0.181	6.798 ± 0.293	

Blaz-7			4.097 ± 0.082	6.826 ± 0.216	1.841 ± 0.062	4.494 ± 0.175	6.929 ± 0.306	
TurPet-1	Turčiansky Peter	Open lake - Turiec Fm.	8.108 ± 0.162	5.975 ± 0.193	1.605 ± 0.054	1.980 ± 0.077	8.570 ± 0.380	8.239 ± 0.208
TurPet-2			14.001 ± 0.280	11.741 ± 0.362	3.373 ± 0.105	2.409 ± 0.089	8.177 ± 0.347	
TurPet-3			7.203 ± 0.144	7.251 ± 0.233	1.882 ± 0.064	2.613 ± 0.103	8.014 ± 0.356	
Kudel-1	Kúdel		4.105 ± 0.082	2.648 ± 0.105	0.575 ± 0.027	1.401 ± 0.072	9.261 ± 0.515	9.206 ± 0.347
Kudel-2			4.328 ± 0.087	2.843 ± 0.100	0.638 ± 0.027	1.473 ± 0.069	9.161 ± 0.470	
Kudel-3*			5.879 ± 0.118	16.734 ± 0.522	4.886 ± 0.153	8.310 ± 0.309	5.699 ± 0.243	
MarTeh-1	Martin - claypit		6.185 ± 0.124	2.691 ± 0.097	0.591 ± 0.028	0.956 ± 0.050	10.027 ± 0.561	10.000 ± 0.382
MarTeh-2			3.352 ± 0.067	1.723 ± 0.075	0.295 ± 0.023	0.880 ± 0.070	10.193 ± 0.837	
MarTeh-3			3.850 ± 0.077	2.077 ± 0.084	0.404 ± 0.025	1.049 ± 0.068	9.840 ± 0.668	

952

5. Discussion

5.1 Authigenic $^{10}Be/^{9}Be$ geochronology

The meteoric ^{10}Be concentration in an authigenic phase shows dependence with the duration of exposure of a soil profile to meteoric waters as well as with the intensity of precipitation, due to the retention of beryllium and its possible mobility in positive water balance settings (Tsai et al., 2008; Graly et al., 2010; Willenbring and von Blanckenburg, 2010; Bacon et al., 2012; Dixon et al., 2018). The rate of burial of sedimentary strata provides a possible clue to resolve the observed initial $^{10}Be/^{9}Be$ ratio variability in the Turiec Basin across one order of magnitude, since it affects duration and magnitude of pedogenesis.

The lowest ratio of $143.36 \pm 1.41 \times 10^{-11}$ was measured at the Veľký Čepčín site, a Late Pleistocene alluvial fan in its origin, and one where the sediment supply was high, and strata were buried abruptly (Table 5). The Malý Čepčín site accumulated in conditions of lower sediment supply in a Late Pleistocene river terrace and exhibited a higher isotopic ratio of $520.92 \pm 8.69 \times 10^{-11}$. The highest isotopic ratios of $632.81 \pm 8.61 \times 10^{-11}$ and $1007.56 \pm 16.78 \times 10^{-11}$ were arrived at the two sites of Holocene river floodplains (Košťany and Kaľamenová sites), sites with low sediment supply of only muddy sediment.

The four sites differ in their positions relative to the present-day groundwater level (Fig. 16), which is relevant to the intensity of pedogenesis and potential post-depositional precipitation of authigenic rims. The Veľký Čepčín alluvial fan forms a topographic elevation with reduced potential for post-depositional precipitation, in contrast to the floodplain and river terrace sites, which are within the range of the present groundwater level. Moreover, the Holocene floodplain samples contain a higher proportion of smectite and/or kaolinite at the expense of illite or illite/smectite in comparison to the Late Pleistocene ones, a phenomenon which implies a higher intensity of chemical weathering over the course of their existence. The Košťany nad Turcom

977 and Kaľamenová sites show increased concentrations of Fe and Mn in correlation with high Be
978 content in the authigenic phase (Fig. 15A,B). Finally, the increased concentration of iron in the
979 authigenic phase correlates with increase of $^{10}Be/^{9}Be$ (Fig. 15C), and even more pronounced
980 difference of the floodplain and alluvial fan sites is shown when normalizing the iron
981 concentration using low-mobility aluminum (Fig. 15D). These observations support the
982 hypothesis of different authigenic rim growth history of the floodplain environment in
983 comparison to the Veľký Čepčín alluvial fan.

984 The Veľký Čepčín site is considered to be the best fit initial $^{10}Be/^{9}Be$ ratio for the Upper
985 Miocene dated sites, since the succession accumulated in conditions of high sediment supply,
986 similar to that documented by facies analysis of the dated sites. The high rate of deposition
987 might be expected to decrease the intensity of post-depositional processes as well as the input
988 of ^{10}Be from meteoric water and groundwater precipitation, and these conditions were likely
989 similar to the Veľký Čepčín site and the dated sites. Such input of ^{10}Be enhanced by pedogenesis
990 as is shown by the floodplain initial ratio sites could not be expected in the case of the dated
991 open lacustrine strata. Moreover, it was shown that the intensity of denudation significantly
992 affects the authigenic $^{10}Be/^{9}Be$ ratio (Willenbring and von Blanckenburg, 2010; von
993 Blanckenburg and Bouchez, 2014), and the facies inventory implies similar denudation
994 conditions for sources of sediment in the Veľký Čepčín site and the dated depositional systems.

995 The Veľký Čepčín initial ratio from alluvial fan settings was selected for the age calculation of
996 all dated Upper Miocene outcrops representing open lake, fan delta, alluvial fan and the braided
997 river because only this initial ratio yielded ages in agreement with independent age proxies
998 indicating that the Martin Formation lacustrine deposits cannot be older than 11.6 Ma. These
999 proxies include ostracod biostratigraphy (Kováč et al., 2011; Pipík et al., 2012), mollusk
1000 biostratigraphy (Neubauer et al., 2015) and magnetostratigraphy (Márton et al., 2022). All
1001 remaining initial ratios provide ages older than 11.6 Ma for the Martin – the claypit site and

1002 partly also the Kúdel and Turčiansky Peter sites (Table 10 in Šujan et al., submitted), and this
1003 excludes the reliability of the latter N_0's for the age calculation of the lacustrine facies in the
1004 Turiec Basin.

1005 A common approach established for the dating of the Upper Miocene successions of the
1006 Pannonian Basin System (PBS) relies on changes in the initial $^{10}Be/^{9}Be$ ratio due to (1) sediment
1007 source proximity affecting relative ^{9}Be delivery and (2) the depositional rate driving a
1008 penecontemporary relative increase of ^{10}Be from the basinal waters (Šujan et al., 2016; Magyar
1009 et al., 2019; Joniak et al., 2020; Šujan et al., 2020). The paleoenvironmental variability is
1010 projected in the usage of riverine and lacustrine initial ratios for different environments in PBS
1011 (Šujan et al., 2016). However, Lake Turiec represented a spatially restricted water mass, much
1012 less complex than Lake Pannon, which was, after all, several orders of magnitude larger
1013 (Magyar et al., 2013). Therefore, we suggest that the degree of paleoenvironmental variability
1014 of the Late Miocene depositional systems filling the Turiec Basin was in all probability not high
1015 enough to produce significant spatial differences in the initial authigenic $^{10}Be/^{9}Be$ ratio, and
1016 that therefore the Veľký Čepčín N_0 may be taken to be representative of all dated sites.

1017 Table 6 includes the 31 ages calculated using the Veľký Čepčín initial ratio and Fig. 17 shows
1018 the distribution of these ages. The low variability within sites allowed us to calculate weighted
1019 mean ages using the KDX application (Spencer et al., 2017); this was done directly for the
1020 Valča, Socovce, Martin – claypit and Turčiansky Peter sites. Outliers appeared at the Kúdel
1021 (Kudel-3), Abramová - Kolísky (Kolisky-2) and Blažovce sites (Blaz-1 and Blaz-4), and
1022 weighted mean ages were calculated only after excluding these. The four samples from the
1023 Ondrašová site yielded ages with a wide scatter, which prevented a weighted mean age
1024 calculation and the same is valid for the two samples from the Slovany site.

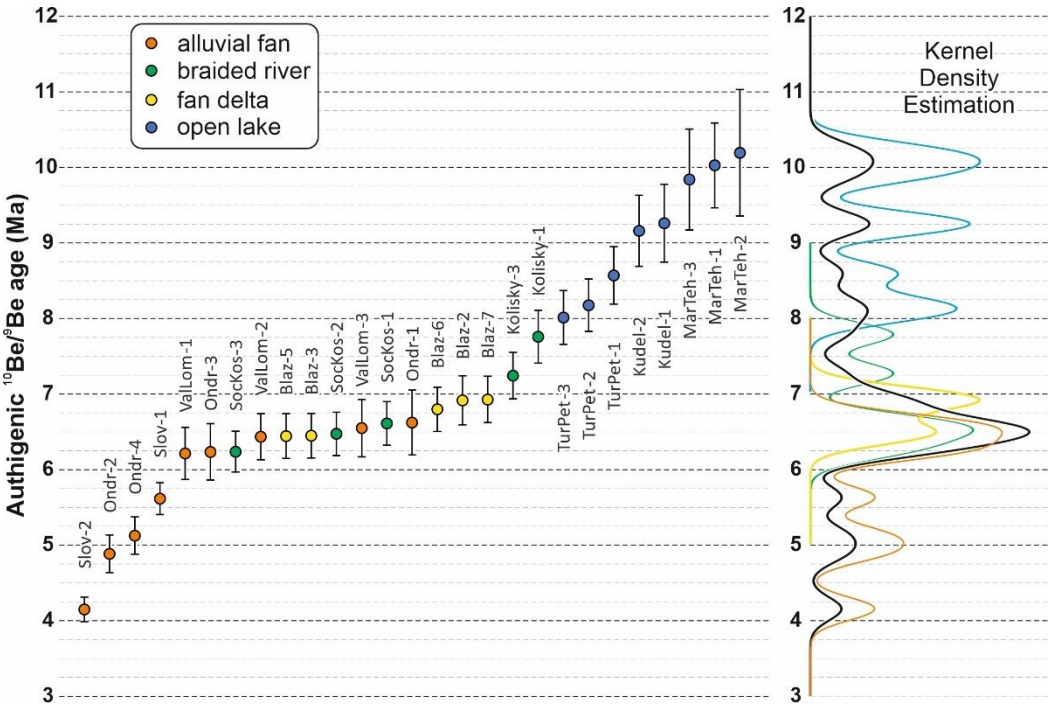

Fig. 17. Cumulative distribution of the authigenic ^{10}Be/^{9}Be ages of all dated localities with the absence/exclusion of four excluded outliers (Blaz-1, Blaz-4, Kolisky-2, Kudel-3). The distribution of values indicates the culmination of the sediment supply at ~7.1–6.0 Ma with a peak at ~6.5 Ma. Kernel Density Estimation yielded by the KDX application (Spencer et al., 2017). The black line in the KDE plot represents the distribution of all samples.

5.2 Paleoenvironmental characteristics from inorganic proxies

The alluvial and braided river mud can be described as carbonate based on the classification by Herron (1988). The Blažovce delta consists of calcareous mud, and samples from open lake sites lie on the boundary between noncalcareous and calcareous mud to wacke (Herron, 1988). It documents the decrease in carbonate content from alluvial mud trough braided river and delta muds to open lake sediments, as the sediment pass through the source-to-sink system (Fig. 14). The loss of carbonate grains with an increase in transport length is also supported by XRD. The detritic origin of carbonate grains is indicated by the presence of dolomite together with calcite in their composition, and by the dominance of the silt fraction in grain size analyses (Table 3, Table 5 in Šujan et al., submitted). Moreover, the carbonate composition of gravel layers above and below these mud intercalations supports this assumption. It should be noted that samples

1043 from a single correlated level may well contain various proportions of carbonate (lateral
1044 variation: Blaz-3 and Blaz-5 yield 17 and 24 wt. % of CO_2, respectively) (Table 9 in Šujan et
1045 al., submitted), which further supports an assumption of the detritic origin of these carbonates.

1046 On the other hand, in the case of open lake sediments, a change in provenance/source rocks
1047 needs to be considered, as it is implied by the higher Si/Al ratio in open lake mud, plus the fact
1048 that these samples are seen close to the shale/wacke boundary in a diagram on Fig. 14 according
1049 to Herron (1988). Despite the fact that open lake muds are more coarse-grained, they do contain
1050 a small proportion of carbonate grains, and this points to the presence of different, silicate
1051 source rocks during the deposition of open lake mud. This may, in turn, be explained by the
1052 spatial location of sites, in that the studied open lake outcrops are located in the northern
1053 depocenter of the Turiec Basin (Fig. 1C), while the latter are to be found in the elevated
1054 boundary area dividing the two depressions, and the difference in provenance is therefore a
1055 likely option. In the northern part of the basin, Paleozoic granitoids and gneiss, together with
1056 carbonates, build up the basin margin. The geochemical analysis also confirms that carbonate
1057 alluvial mud contains the lowest portion of Fe, and the content of Fe increases with the portion
1058 of silicate minerals which represent the primary source of Fe (Fig. 14).

1059 Concentrations of other elements such as Cu, Ni, Mo, Pb, and As are elevated in samples Blaz-
1060 1 and Blaz-2 compared to those in Blaz-3,5,7 (Table 8 in Šujan et al., submitted), but the level
1061 of organic carbon is approximately the same (0.4–0.6 %). This may be explained by the change
1062 in source, and also by the anthropogenic pollution of Blaz-1 and Blaz-2 samples. Nevertheless,
1063 this option is highly unlikely, considering the settings of the sites (Fig. 12 in Šujan et al.,
1064 submitted). A change in redox conditions during the deposition of Blaz-1,2 is implausible due
1065 to the low organic carbon content. The more detailed whole rock analyses of the Blažovce delta
1066 mud point to freshwater, oxic bottom water conditions via low values of sulfur content, TOC
1067 (total organic carbon), the C_{org}/P molar ratio and low values of the Mo and Ni enrichment factors

(Berner, 1984; Raiswell and Berner, 1986; Jones and Manning, 1994; Algeo and Liu, 2020, and references therein; Wei and Algeo, 2020). The slightly increased U content (U_{ef} 1.1–1.7) can be explained by the presence of carbonates in the composition (Table 9 in Šujan et al., submitted). The CIA index (Nesbitt and Young, 1982), following the simplification found in McLennan (1993), reaches 82–86, and this range indicates a medium to high degree of chemical weathering in the source area and/or after mud accommodation (Fig. 14). Generally, the Si/Al ratio of the Blažovce samples documents increasing grain size as we proceed upwards, consistent with increasing carbonate clastic input due to the progradation of the deltaic system.

5.3 Evolution of the Turiec Basin

The obtained weighted mean ages indicate that the open lake environment of Lake Turiec persisted at least from 10.000 ± 0.382 Ma to 6.697 ± 0.135 Ma. The disappearance of the lake is evidenced by the progradation of the alluvial fan-braided river-fan delta depositional system and appeared at 6.697 ± 0.135 Ma, according to the age of the Blažovce site. The braided river environment existed parallel to the open lake (7.469 ± 0.231 Ma, Abramová - Kolísky) or later, in a similar period to the fan deltaic environment (6.432 ± 0.162 Ma, Socovce). The alluvial fan sites are coeval with or younger than the deltaic and braided river environment, reaching 6.394 ± 0.195 Ma (Valča), or the ages in the range of 7.03–4.64 Ma (Ondrašová) and 5.83–3.98 Ma (Slovany), which fit with the notion that the general stratigraphic position of the alluvial fan deposits represent the final part of the basin fill.

The ages generally confirm the earlier lithostratigraphic concept suggested by Kováč et al. (2011). Nevertheless, the integration of authigenic $^{10}Be/^{9}Be$ dating, sedimentology, geochemistry and basin analysis using lithological borehole logs implies the concurrent existence of alluvial fan-braided river-fan delta-open lake sedimentary environments as an

1091 interconnected source-to-sink system. This conception differs from the originally expectation
1092 of the isolated nature of the phases of persistence of these environments.

1093 Despite the very restricted scale of Lake Turiec (~10 × 40 km), its environment persisted for at
1094 least ~3.25 Myr, and likely for an even longer period, since this study provides only ages of the
1095 surface exposure of the Martin Formation. These lacustrine deposits reach a thickness of up to
1096 900 m, hence, the accommodation rate reached the order of ~200–300 m/Myr. Although
1097 subsidence was relatively high, the surrounding subaerially exposed blocks did not yield
1098 enough sediment supply to cause regression of the lake during the period ~10.0–6.7 Ma. This
1099 then implies that the base level was balanced on the marginal blocks without significant incision
1100 and streams flowing to the Turiec Basin did not form large alluvial fans (Fig. 18). The
1101 floodplains of small rivers likely entered the lake as shoal-water deltas (García-García et al.,
1102 2006; Ghinassi, 2007), but these were not observed in the exposed depositional record. The
1103 assumption of moderate topography around the lake is also supported by paleoecological
1104 proxies, which indicate the existence of marshes, coastal wetlands, and humid forests (Chapter
1105 2.2).

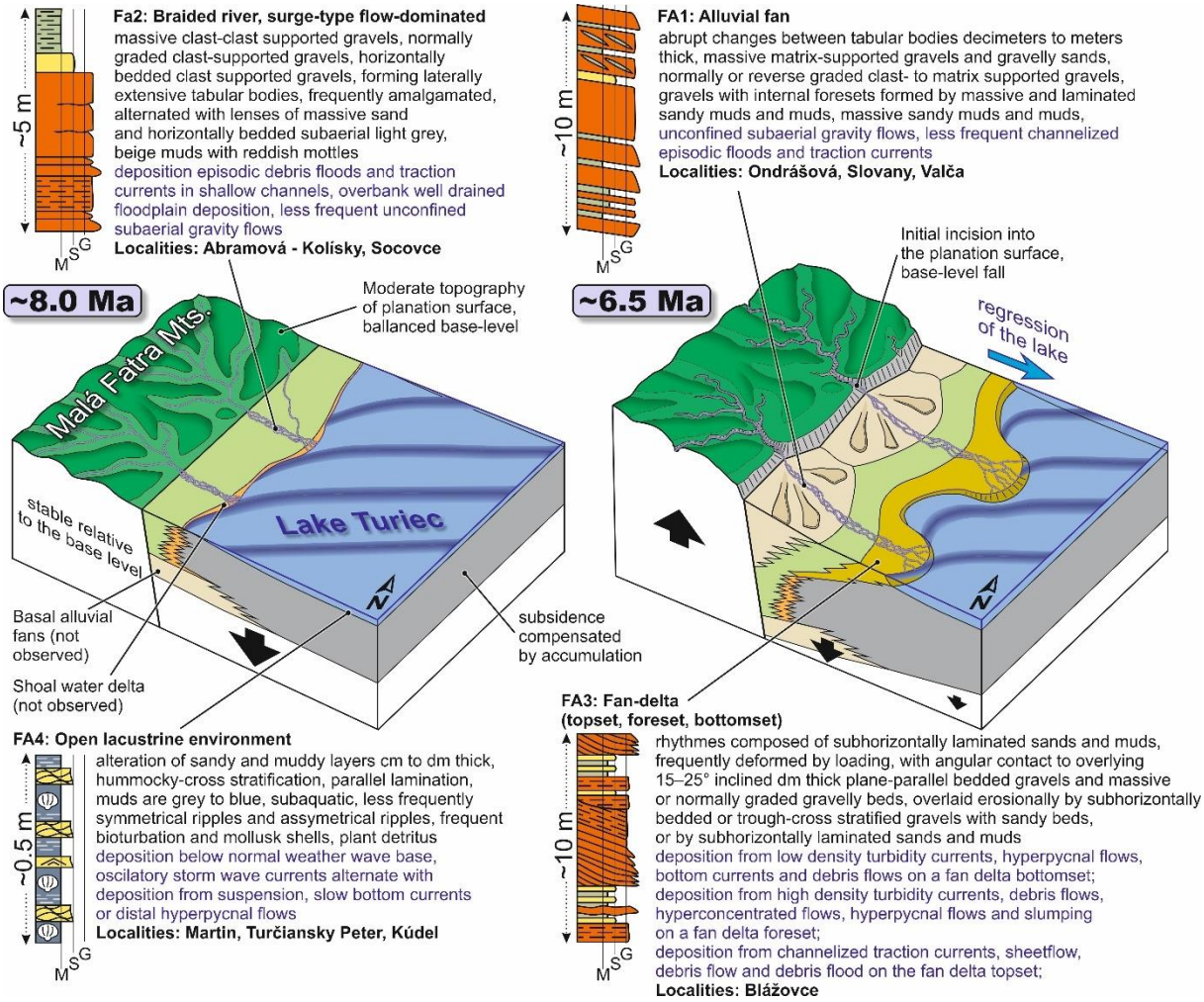

Fig. 18. Block diagrams showing the distribution of facies associations in the Turiec Basin concerning accommodation rate and sediment supply driven mainly by vertical motions. The period of balanced accommodation and sediment supply lasted during the existence of Lake Turiec (left), when endemic fauna evolved and the surrounding mountains formed only a moderate hilly landscape without intense incision. The changed tectonic regime led to an increased rate of uplift of the mountains on the western margin of the basin and a consequent increase in the ratio of sediment supply to accommodation rate, which caused the regression and disappearance of Lake Turiec and the extinction of the endemic fauna.

The situation changed significantly at ~6.7 Ma (Blažovce site), or ~6.5 Ma (peak of the KDE distribution, Fig. 17), when sediment supply from the western margin of the basin (Malá Fatra Mts.) significantly increased. A system of alluvial fans started to feed the rivers, which entered the lake as sandy-gravelly fan deltas (Fig. 18). Turiec Lake was shallow from the sedimentological point of view, likely far less than 100 m, hence, only delta-scale clinoforms

prograded across its water body (Patruno and Helland-Hansen, 2018). The regression therefore appeared relatively abruptly, in <100 kyr, as a result of increased sediment supply (sensu Catuneanu, 2006), despite the delta progradation being affected by flooding events of a high order of cyclicity (Fig. 10). The increase in sediment supply must have been caused by the uplift of the Malá Fatra Mts. and incision of rivers into the massif due to the relative base level fall. The prevailing direction of the delta progradation towards the southwest at the Blažovce site corresponds generally with the orientation to the main depocenter of the southern Turiec Basin (Fig. 13 in Šujan et al., submitted). Nevertheless, the course of the fan delta lobe progradation is mainly moderated by autogenic processes (Van Dijk et al., 2009). The demand for a more spatially distributed dataset to underpin robustness of the paleotransport assumption is limited by absence of further exposures of the deltaic succession.

An alluvial fan environment likely covered most of the studied area in the period following the regression of Lake Turiec, as is indicated by the distribution of this facies association across the basin (Fig. 13). However, subsequent basin inversion (Kováč et al., 2011) and erosion of the basin fill caused surface exposure of 6–10 Ma old successions, and the specific history of the basin just after the regression of Lake Turiec is a conundrum because of the missing depositional record.

5.4 Implications for geodynamic processes and paleogeography

The timing of the major change in the accommodation rate to sediment supply ratio in the Turiec Basin is similar to the timing of the inversion of the Pannonian Basin System (PBS), which happened time transgressively across the region at ~8–4 Ma (Fodor et al., 2005; Horváth et al., 2006; Bada et al., 2007; Ruszkiczay-Rüdiger et al., 2007; Uhrin et al., 2009) and around 6 Ma in its northwesternmost part, the Danube Basin (Šujan et al., 2021b). The basin inversion of the PBS was related to several processes, such as the push of the Adria lithospheric microplate,

topography-induced gravitational stress, differential loading of syn-inversion sediments that caused the elastic flexure of a weakened lithosphere, as well as the general heterogeneous contraction of the rheologically layered lithosphere exposed to temporal thermomechanical changes after rifting (Burov and Cloetingh, 1997; Bada et al., 2001; Jarosinski et al., 2011; Ruszkiczay-Rüdiger et al., 2020; Tari et al., 2020). This resulted in lithospheric-scale folding associated with a major reduction in accommodation of the affected basins, their uplift, and the denudation of basin fill.

The coincidence in the timing of the PBS inversion with the termination of Lake Turiec's existence by a rapid increase of sediment supply from the uplifting mountains is likely linked to a common geodynamic cause. The regional change in the geodynamic regime would be expected to affect the local stress field and kinematics of the faults, which were driving the subsidence of the Turiec Basin (Kováč et al., 2011). It is a matter for future research to implement the new geochronological data obtained in this study to resolve changes in the of the basin formation regime.

The thermochronological data obtained from the Malá Fatra Mts. (Kráľ et al., 2007; Danišík et al., 2010; Králiková et al., 2014b) (Fig. 1C) imply that a phase of intense exhumation appeared within the time constraints ~15–7 Ma. It was associated with the tectonic escape of the ALCAPA microplate towards the northeast and its collision with the European platform (Ratschbacher et al., 1991; Kováč et al., 2017b). This evolutionary stage likely preceded the period of relative tectonic quiescence documented by the low intensity of denudation of the morphostructures surrounding Lake Turiec, and formation of the so called “Mid-mountain level” planation surface (Mazúr, 1963; Minár et al., 2011).

Given the moderate humidity expected in the region during the Late Miocene (van Dam, 2006; Böhme et al., 2008; Kováčová et al., 2011; Utescher et al., 2017), the long-lived lake might have persisted only in an endorheic basin, since outflowing streams would have broken

topographic barriers and disrupted its landlocked storage (Bridgland et al., 2020). The authigenic $^{10}Be/^{9}Be$ dating and distribution of facies indicate the endorheic character of the Turiec basin in the period of ~10.0–6.7 Ma. Hence, the drainage of the Váh river in its present extent, draining a significant part of the Western Carpathians, and flowing through the Turiec Basin (Fig. 19), might have been formed only after ~6.7 Ma. However, a stream providing major coarse-sediment supply with the characteristics of a distant provenance appeared in the northern Danube Basin at ~9 Ma, forming the fluvial fan of the Piešťany Member (Šujan et al., 2017). Despite the fact that it was considered an equivalent of the present Váh river, the extent of this stream paleo-drainage network was restricted by Lake Turiec and remains to be fully uncovered.

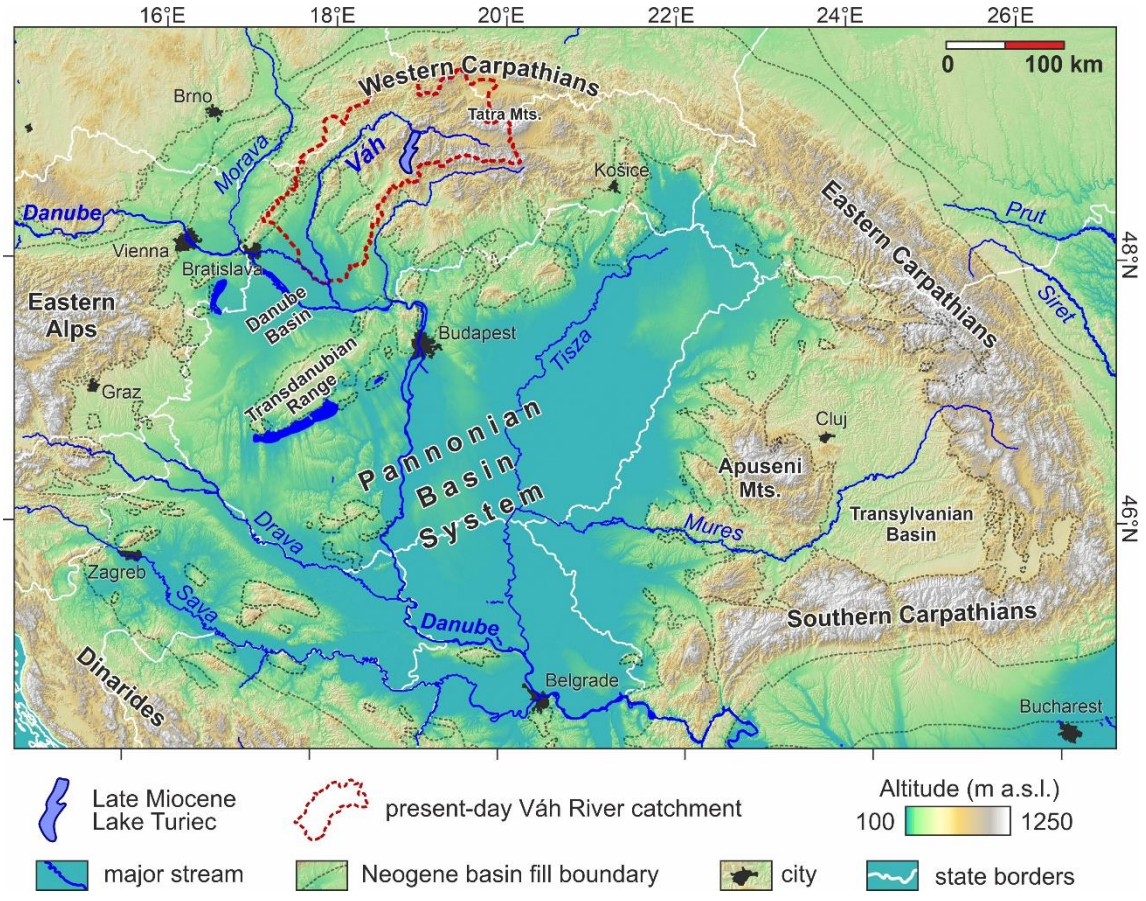

Fig. 19. Location of the present-day Váh River catchment within the Carpathian-Pannonian source-to-sink-system, which ultimately fills the Black Sea Basin at the Danube delta. Lake Turiec acted as a transient storage for the sediment denudated

upstream during its endorheic period at ~10.0–6.7 Ma, and system connectivity was established only later. The upstream area includes the recently most topographically exposed mountains of the Western Carpathians, like the Tatra Mts.

The most exposed morphostructures of the Western Carpathians, like the Tatra Mts., are presently located upstream of the Turiec Basin, and sediment delivery within the source-to-sink system towards the Pannonian Basin might have been established only after the regression and disappearance of Lake Turiec (Fig. 19). This implies a limited sediment supply from these parts of the orogenic belt during the period ~10.0–6.7 Ma. The thermochronological estimate of accelerated uplift of the Tatra Mts. after ~7 Ma (Králiková et al., 2014c) is in agreement with the inferred low input of sediment towards Lake Turiec from this area.

The endorheic Turiec Basin formed a transient storage for sediment eroded from surrounding mountains. The establishment of drainage network connectivity by the overfilling of the basin after the lake regression likely led to an incision, and to a decrease in accommodation rates (Schildgen et al., 2016; Geurts et al., 2018). Loading by the ~1000 m thick Upper Miocene succession related to the existence of Lake Turiec would be expected to have enhanced the accommodation rates, and the termination of the endorheic period further amplified incision by unloading the area of the basin (Ballato et al., 2019). These processes correspond to the stratigraphic architecture of the Turiec Basin, since the post-Late Miocene incision led to the surficial exposure of sediments up to ~10 Ma old (Fig. 2). Future dating of the Pliocene-Quaternary successions overlying the Lake Turiec tectonic sequence (*sensu* Matenco and Haq, 2020), e.g., the Diviaky Member (Fig. 2) may help to resolve whether younger periods of endorheic basin character did indeed appear, and will reveal a younger history of base-level variations.

6. Conclusions

This study provides a complex analysis of the Upper Miocene tectonic sequence (*sensu* Matenco and Haq, 2019) in the Turiec Basin, Western Carpathians (Central Europe), in order to reveal the timing and mode of regression of the long-lived Lake Turiec in this intermontane basin. The sedimentological analysis of nine outcrops served to identify alluvial fan, braided river, fan delta and open lake facies associations, which were correlated across the basin using borehole profiles. Authigenic $^{10}Be/^{9}Be$ dating implies that a period of relatively rapid subsidence and low sediment supply from surrounding morphostructures to Lake Turiec occurred between ~10.0–6.7 Ma. The lake persisted until it was filled by a significant increase in sediment supply to accommodation rate ratio at ~6.7 Ma, when extensive alluvial fans associated with fan deltas appeared. The newly formed depositional systems were fed by the uplifted Malá Fatra Mts. from the west. The lake regression after ~6.7 Ma led to the termination of the endorheic period of the Turiec Basin, allowing the establishment of drainage network connectivity within the Western Carpathians and the formation of the present-day Váh river drainage, which delivers sediment from the most topographically exposed mountains of the orogenic belt towards the Pannonian Basin and the Danube watershed. Hence, the established model of the Turiec Basin evolution significantly contributes to the overall understanding of the temporal evolution of the Carpathian-Pannonian-Black Sea source-to-sink system (Matenco et al., 2016).

The analysis of Late Pleistocene to Holocene alluvial strata uncovered a one order of magnitude variation in initial authigenic $^{10}Be/^{9}Be$ ratios, and this is relevant to the applicability of this dating method. Sedimentological, geochemical and mineralogical proxies indicate that the analyzed sites differ in accommodation rates, in the pace of burial of the sampled strata, and in the connectivity to groundwater. These differences affect the intensity of ^{10}Be input from meteoric waters before a bed is buried and the preserved authigenic $^{10}Be/^{9}Be$ ratio is attained.

Therefore, the alluvial fan site with highest rate of sediment supply and strata burial, and lowest degree of connectivity to groundwater level was selected as representative for the purposes of age calculations, since its depositional conditions were similar to those of the dated sites. Moreover, other initial ratios yielded ages of open lake strata which proved to be inconsistent with independent age constraints.

The study implies that fills of intermontane basins with relatively high accommodation rates might serve as targets suitable for the application of authigenic $^{10}Be/^{9}Be$ dating. The favorable factors in these settings are the low probability of post-depositional alteration of the authigenic $^{10}Be/^{9}Be$ record and the limited recycling of the basin fill by redeposition of mud with an older $^{10}Be/^{9}Be$ signature, similar to that observed in the back-arc settings of the Danube Basin (Šujan et al., 2020; Šujan et al., 2023).

Acknowledgement

The study was supported by the Slovak Research and Development Agency (APVV) under contracts Nos. APVV-16-0121, APVV-20-0120 and APVV-21-0281, and by the Scientific Grant Agency of the Ministry of Education, Science, Research and Sport of the Slovak Republic and the Slovak Academy of Sciences (VEGA) under the contract No. 1/0346/20. The free availability of the Lidar DEM data owned by the Geodesy, Cartography and Cadaster Authority of the Slovak Republic (ÚGKK SR) and distributed by the Geodetic and Cartographic Institute, Bratislava (GKÚ) is acknowledged with gratitude. The ASTER AMS national facility (CEREGE, Aix-en-Provence, France) is supported by the INSU/CNRS, the ANR through the "Projets thématiques d'excellence" program for the "Equipements d'excellence" ASTER-CEREGE action, and IRD. Paul Thatcher is thanked for his efforts made during the language correction.

References

Algeo, T.J. and Liu, J., 2020. A re-assessment of elemental proxies for paleoredox analysis. Chemical Geology, 540, 119549.

Allen, J.R.L., 1982. Sedimentary Structures: Their Character and Physical Basis. Elsevier, Amsterdam, 593 pp.

Amoudry, L.O., Bell, P.S., Thorne, P.D. and Souza, A.J., 2013. Toward representing wave-induced sediment suspension over sand ripples in RANS models. Journal of Geophysical Research: Oceans, 118(5), 2378-2392.

Aslan, A. and Autin, W.J., 1999. Evolution of the Holocene Mississippi River floodplain, Ferriday, Louisiana: Insights on the origin of fine-grained floodplains. Journal of Sedimentary Research, 69(4), 800-815.

Baas, J.H., Best, J.L. and Peakall, J., 2016. Predicting bedforms and primary current stratification in cohesive mixtures of mud and sand. Journal of the Geological Society, 173(1), 12-45.

Bacon, A.R., Richter, D.d., Bierman, P.R. and Rood, D.H., 2012. Coupling meteoric ^{10}Be with pedogenic losses of ^{9}Be to improve soil residence time estimates on an ancient North American interfluve. Geology, 40(9), 847-850.

Bada, G., Horváth, F., Cloetingh, S., Coblentz, D.D. and Tóth, T., 2001. Role of topography-induced gravitational stresses in basin inversion: The case study of Pannonian basin. Tectonics, 20(3), 343-363.

Bada, G., Horváth, F., Dövényi, P., Szafián, P., Windhoffer, G. and Cloetingh, S., 2007. Present-day stress field and tectonic inversion in the Pannonian basin. Global and Planetary Change, 58(1–4), 165-180.

Ballato, P., Brune, S. and Strecker, M.R., 2019. Sedimentary loading–unloading cycles and faulting in intermontane basins: Insights from numerical modeling and field observations in the NW Argentine Andes. Earth and Planetary Science Letters, 506, 388-396.

Benvenuti, M., 2003. Facies analysis and tectonic significance of lacustrine fan-deltaic successions in the Pliocene-Pleistocene Mugello Basin, Central Italy. Sedimentary Geology, 157(3-4), 197-234.

Berner, R.A., 1984. Sedimentary pyrite formation: An update. Geochimica et Cosmochimica Acta, 48, 605-615.

Bielik, M., Krajňák, M., Makarenko, I., Legostaeva, O., Starostenko, V.I., Bošanský, M., Grinč, M. and Hók, J., 2013. 3D gravity interpretation of the pre-Tertiary basement in the intramontane depressions of the Western Carpathians: A case study from the Turiec Basin. Geologica Carpathica, 64(5), 399-408.

Blikra, L.H. and Nemec, W., 1998. Postglacial colluvium in western Norway: depositional processes, facies and palaeoclimatic record. Sedimentology, 45(5), 909-959.

Böhme, M., Ilg, A. and Winklhofer, M., 2008. Late Miocene "washhouse" climate in Europe. Earth and Planetary Science Letters, 275(3–4), 393-401.

Boothroyd, J.C. and Ashley, G.M., 1975. Processes, Bar Morphology, and Sedimentary Structures on Braided Outwash Fans, Northeastern Gulf of Alaska. In: A.V. Jopling and B.C. McDonald (Eds.), Glaciofluvial and Glaciolacustrine Sedimentation. SEPM Society for Sedimentary Geology, pp. 193-222.

Boulesteix, K., Poyatos-Moré, M., Flint, S.S., Taylor, K.G., Hodgson, D.M. and Hasiotis, S.T., 2019. Transport and deposition of mud in deep-water environments: Processes and stratigraphic implications. Sedimentology, 66(7), 2894-2925.

Bourles, D., Raisbeck, G. and Yiou, F., 1989. ^{10}Be and ^{9}Be in marine sediments and their potential for dating. Geochimica et Cosmochimica Acta, 53(2), 443-452.

Braucher, R., Guillou, V., Bourlès, D.L., Arnold, M., Aumaître, G., Keddadouche, K. and Nottoli, E., 2015. Preparation of ASTER in-house $^{10}Be/^{9}Be$ standard solutions. Nuclear Instruments and Methods in Physics Research Section B: Beam Interactions with Materials and Atoms, 361, 335-340.

Brenna, A., Surian, N., Ghinassi, M. and Marchi, L., 2020. Sediment–water flows in mountain streams: Recognition and classification based on field evidence. Geomorphology, 371, 107413.

Bridgland, D.R., Westaway, R. and Hu, Z., 2020. Basin inversion: A worldwide Late Cenozoic phenomenon. Global and Planetary Change, 193, 103260.

Brown, E.T., Measures, C.I., Edmond, J.M., Bourlès, D.L., Raisbeck, G.M. and Yiou, F., 1992. Continental inputs of beryllium to the oceans. Earth and planetary science letters, 114(1), 101-111.

Brumsack, H.J., 1989. Geochemistry of recent TOC-rich sediments from the Gulf of California and the Black Sea. Geologische Rundschau, 78, 851- 882.

Budai, S., Colombera, L. and Mountney, N.P., 2021. Quantitative characterization of the sedimentary architecture of Gilbert-type deltas. Sedimentary Geology, 426, 106022.

Buday, T., 1962. Neogene of the Turiec Basin. Sborník Ústředního Ústavu Geologického – Geológia, 27, 475-502 (in Slovak).

Burbank, D.W., 1983. The chronology of intermontane-basin development in the northwestern Himalaya and the evolution of the Northwest Syntaxis. Earth and Planetary Science Letters, 64(1), 77-92.

Burov, E. and Cloetingh, S., 1997. Erosion and rift dynamics: new thermomechanical aspects of post-rift evolution of extensional basins. Earth and Planetary Science Letters, 150(1–2), 7-26.

Carcaillet, J., Bourlès, D.L., Thouveny, N. and Arnold, M., 2004. A high resolution authigenic $^{10}Be/^{9}Be$ record of geomagnetic moment variations over the last 300 ka from sedimentary cores of the Portuguese margin. Earth and Planetary Science Letters, 219(3–4), 397-412.

Cartigny, M.J.B., Ventra, D., Postma, G. and van Den Berg, J.H., 2014. Morphodynamics and sedimentary structures of bedforms under supercritical-flow conditions: New insights from flume experiments. Sedimentology, 61(3), 712-748.

Catuneanu, O., 2006. Principles of Sequence Stratigraphy. Elsevier, Amsterdam, 375 pp.

Danišík, M., Kohút, M., Broska, I. and Frisch, W., 2010. Thermal evolution of the Malá Fatra Mountains (Central Western Carpathians): Insights from zircon and apatite fission track thermochronology. Geologica Carpathica, 61(1), 19-27.

International Centre for Diffraction Data, 2022. PDF-4/Minerals, SN: MIND 220124-5612, https://www.icdd.com/pdf-4-minerals/.

Dixon, J.L., Chadwick, O.A. and Pavich, M.J., 2018. Climatically controlled delivery and retention of meteoric ^{10}Be in soils. Geology, 46(10), 899-902.

Dumas, S. and Arnott, R.W.C., 2006. Origin of hummocky and swaley cross-stratification - The controlling influence of unidirectional current strength and aggradation rate. Geology, 34(12), 1073-1076.

Dumas, S., Arnott, R.W.C. and Southard, J.B., 2005. Experiments on oscillatory-flow and combined-flow bed forms: Implications for interpreting parts of the shallow-marine sedimentary record. Journal of Sedimentary Research, 75(3), 501-513.

Fendek, M., Gašparik, J., Gross, P., Janči, J., Kohút, M., Kráľ, J., Kullmanová, A., Planderová, E., Raková, J., Rakús, M., Snopková, P., Tuba, Ľ., Vass, D. and Vozárová, A., 1990. Technical report on geothermal borehole ZGT-3 Turiec in Martin and prognostic resources of geothermal energy in the area of Martin. Manuscript, Geofond Nr.: 75501, 86 pp. available online: https://da.geology.sk/navigator/?desktop=Public.

Fielding, C.R., 2006. Upper flow regime sheets, lenses and scour fills: Extending the range of architectural elements for fluvial sediment bodies. Sedimentary Geology, 190(1-4), 227-240.
Fielding, C.R., Alexander, J. and Allen, J.P., 2018. The role of discharge variability in the formation and preservation of alluvial sediment bodies. Sedimentary Geology, 365, 1-20.
Fodor, L., Bada, G., Csillag, G., Horváth, E., Ruszkiczay-Rüdiger, Z., Palotás, K., Síkhegyi, F., Timár, G., Cloetingh, S. and Horváth, F., 2005. An outline of neotectonic structures and morphotectonics of the western and central Pannonian Basin. Tectonophysics, 410(1–4), 15-41.
Folk, R.L. and Ward, W.C., 1957. A Study in the Significance of Grain-Size Parameters. Journal of Sedimentary Petrology, 27, 3-26.
Froitzheim, N., Plašienka, D. and Schuster, R., 2008. Alpine tectonics of the Alps and Western Carpathians. In: T. McCann (Ed.), The Geology of Central Europe Volume 2: Mesozoic and Cenozoic. Geological Society of London, pp. 1141-1232.
García-García, F., Fernández, J., Viseras, C. and Soria, J.M., 2006. Architecture and sedimentary facies evolution in a delta stack controlled by fault growth (Betic Cordillera, southern Spain, late Tortonian). Sedimentary Geology, 185(1-2), 79-92.
Gašparik, J., 1972. Záverečná správa o vyhodnotení štruktúrneho vrtu GHŠ-1 Horná Štubňa. Manuscript, Geofond Nr: 31218, 57 pp. Available online: https://da.geology.sk/navigator/?desktop=Public.
Gašparík, J. and Halouzka, R., 1993. Explanatory notes to the geological map of the Turiec Basin, scale 1 : 50 000. State Geological Institute of Dionýz Štúr, Bratislava, 196 pp.
Geurts, A.H., Cowie, P.A., Duclaux, G., Gawthorpe, R.L., Huismans, R.S., Pedersen, V.K. and Wedmore, L.N.J., 2018. Drainage integration and sediment dispersal in active continental rifts: A numerical modelling study of the central Italian Apennines. Basin Research, 30(5), 965-989.
Ghinassi, M., 2007. The effects of differential subsidence and coastal topography on high-order transgressive-regressive cycles: Pliocene nearshore deposits of the Val d'Orcia Basin, Northern Apennines, Italy. Sedimentary Geology, 202(4), 677-701.
Gibling, M.R., Ukakimaphan, Y. and Srisuk, S., 1985. Oil shale and coal in intermontane basins of Thailand. American Association of Petroleum Geologists Bulletin, 69(5), 760-766.
Gobo, K., Ghinassi, M. and Nemec, W., 2015. Gilbert-type deltas recording short-term base-level changes: Delta-brink morphodynamics and related foreset facies. Sedimentology.
Graham, I., Ditchburn, R. and Whitehead, N., 2001. Be isotope analysis of a 0–500 ka loess–paleosol sequence from Rangitatau East, New Zealand. Quaternary International, 76, 29-42.
Graly, J.A., Bierman, P.R., Reusser, L.J. and Pavich, M.J., 2010. Meteoric ^{10}Be in soil profiles – A global meta-analysis. Geochimica et Cosmochimica Acta, 74(23), 6814-6829.
Hajek, E.A. and Straub, K.M., 2017. Autogenic Sedimentation in Clastic Stratigraphy. Annual Review of Earth and Planetary Sciences, 45(1), 681-709.
Harzhauser, M. and Mandic, O., 2008. Neogene lake systems of Central and South-Eastern Europe: Faunal diversity, gradients and interrelations. Palaeogeography, Palaeoclimatology, Palaeoecology, 260(3–4), 417-434.
Havrila, M., 2011. Hronikum: paleogeografia a stratigrafia (vrchný pelsón – tuval), štrukturalizácia a stavba. Geologické práce, Správy, 117, 7-103 (in Slovak).
Henken-Mellies, W., Beer, J., Heller, F., Hsü, K., Shen, C., Bonani, G., Hofmann, H., Suter, M. and Wölfli, W., 1990. ^{10}Be and ^{9}Be in South Atlantic DSDP Site 519: Relation to geomagnetic reversals and to sediment composition. Earth and Planetary Science Letters, 98(3-4), 267-276.

Herron, M.M., 1988. Geochemical classification of terrigenous sands and shales from core or log data. Journal of Sedimentary Petrology, 58, 820-829.
Hók, J., Šujan, M. and Šipka, F., 2014. Tectonic division of the Western Carpathians: An overview and a new approach. Acta Geologica Slovaca, 6(2), 135-143.
Holec, J. and Braucher, R., 2014. Cosmogenic chlorine dating of alluvial fan (Veľký Čepčín, Turčianska kotlina basin). In: J. Novotný (Ed.), Geomorfológia a environmentálne výzvy. Zborník abstraktov Bratislava, SAV, 2014, pp. 20.
Horváth, F., Bada, G., Szafián, P., Tari, G., Ádám, A. and Cloetingh, S., 2006. Formation and deformation of the Pannonian Basin: Constraints from observational data, Geological Society Memoir, pp. 191-206.
Chaimov, T.A., Barazangi, M., Al-Saad, D., Sawaf, T. and Gebran, A., 1992. Mesozoic and Cenozoic deformation inferred from seismic stratigraphy in the southwestern intracontinental Palmyride fold-thrust belt, Syria. Geological Society of America Bulletin, 104(6), 704-715.
Chernyshev, I.V., Konečný, V., Lexa, J., Kovalenker, V.A., Jeleň, S., Lebedev, V.A. and Goltsman, Y.V., 2013. K-Ar and Rb-Sr geochronology and evolution of the Štiavnica Stratovolcano (Central Slovakia). Geologica Carpathica, 64(4), 327-351.
Church, M. and Jakob, M., 2020. What Is a Debris Flood? Water Resources Research, 56(8), e2020WR027144.
Inoue, T., Huang, Z.-Y., Imamura, M., Tanaka, S. and Usui, A., 1983. ^{10}Be and ^{10}Be/^{9}Be in manganese nodules. Geochemical Journal, 17(6), 307-312.
Jarosinski, M., Beekman, F., Matenco, L. and Cloetingh, S., 2011. Mechanics of basin inversion: Finite element modelling of the Pannonian Basin System. Tectonophysics, 502(1–2), 121-145.
Jelby, M.E., Grundvåg, S.A., Helland-Hansen, W., Olaussen, S. and Stemmerik, L., 2020. Tempestite facies variability and storm-depositional processes across a wide ramp: Towards a polygenetic model for hummocky cross-stratification. Sedimentology, 67(2), 742-781.
Jones, B. and Manning, D.A.C., 1994. Comparison of geochemical indices used for the interpretation of palaeoredox conditions in ancient mudstones. Chemical Geology, 111(1), 111-129.
Joniak, P., Šujan, M., Fordinál, K., Braucher, R., Rybár, S., Kováčová, M., Kováč, M., Aumaître, G., Bourlès, D.L. and Keddadouche, K., 2020. The age and paleoenvironment of a late Miocene floodplain alongside Lake Pannon: Rodent and mollusk biostratigraphy coupled with authigenic ^{10}Be/^{9}Be dating in the northern Danube Basin of Slovakia. Palaeogeography, Palaeoclimatology, Palaeoecology, 538.
Kilényi, E. and Šefara, J., 1991. Pre-Tertiary basement contour map of the Carpathian Basin Beneath Austria, Czechoslovakia and Hungary. Geophysical Transactions, 36(1-2), 15-36.
Konečný, V., Kováč, M., Lexa, J. and Šefara, J., 2002. Neogene evolution of the Carpatho-Pannonian region: an interplay of subduction and back-arc diapiric uprise in the mantle. EGS Stephan Mueller Special Publication, 1, 105-123.
Konečný, V., Lexa, J. and Hojstričová, V., 1995. The Central Slovakia Neogene volcanic field: a review. Acta Volcanologica, 7, 63-78.
Konečný, V., Lexa, J. and Planderová, E., 1983. Stratigraphy of the Central Slovakia volcanic field. Západné Karpaty, Séria Geológia, 9, 1-203 (in Slovak with English summary).
Kong, W., Zhou, L. and AsterTeam, 2021. Tracing Water Masses and Assessing Boundary Scavenging Intensity With Beryllium Isotopes in the Northern South China Sea. Journal of Geophysical Research: Oceans, 126(7), e2021JC017236.

Kováč, M., Halásová, E., Hudáčková, N., Holcová, K., Hyžný, M., Jamrich, M. and Ruman, A., 2018. Towards better correlation of the Central Paratethys regional time scale with the standard geological time scale of the Miocene Epoch. Geologica Carpathica, 69(3), 283-300.

Kováč, M., Hók, J., Minár, J., Vojtko, R., Bielik, M., Pipík, R., Rakús, M., Kráå, J., Åujan, M. and Králiková, S., 2011. Neogene and Quaternary development of the Turiec Basin and landscape in its catchment: A tentative mass balance model. Geologica Carpathica, 62(4), 361-379.

Kováč, M., Hudáčková, N., Halásová, E., Kováčová, M., Holcová, K., Oszczypko-Clowes, M., Báldi, K., Less, G., Nagymarosy, A., Ruman, A., Klučiar, T. and Jamrich, M., 2017a. The Central Paratethys palaeoceanography: A water circulation model based on microfossil proxies, climate, and changes of depositional environment. Acta Geologica Slovaca, 9(2), 75-114.

Kováč, M., Márton, E., Oszczypko, N., Vojtko, R., Hók, J., Králiková, S., Plašienka, D., Klučiar, T., Hudáčková, N. and Oszczypko-Clowes, M., 2017b. Neogene palaeogeography and basin evolution of the Western Carpathians, Northern Pannonian domain and adjoining areas. Global and Planetary Change, 155, 133-154.

Kováč, M., Plašienka, D., Soták, J., Vojtko, R., Oszczypko, N., Less, G., Ćosović, V., Fügenschuh, B. and Králiková, S., 2016. Paleogene palaeogeography and basin evolution of the Western Carpathians, Northern Pannonian domain and adjoining areas. Global and Planetary Change, 140, 9-27.

Kováč, P. and Hók, J., 1993. The Central Slovak Fault System - the field evidence of a strike slip. Geologica Carpathica, 44(3), 155-159.

Kováčová, M., Doláková, N. and Kováč, M., 2011. Miocene vegetation pattern and climate change in the northwestern Central Paratethys domain (Czech and Slovak Republic). Geologica Carpathica, 62(3), 251-256.

Kráľ, J., Hók, J., Kotulová, J. and Rakús, M., 2007. Apatite fission-track data interpretation from the Lúčanská Fatra Mts. (Western Carpathians). Mineralia Slovaca, Geovestník, 39(4), 5-6.

Králiková, S., Vojtko, R., Andriessen, P., Kováč, M., Fuegenschuh, B., Hók, J. and Minár, J., 2014a. Late Cretaceous-Cenozoic thermal evolution of the northern part of the Central Western Carpathians (Slovakia): revealed by zircon and apatite fission track thermochronology. Tectonophysics, 615, 142-153.

Králiková, S., Vojtko, R., Andriessen, P., Kováč, M., Fügenschuh, B., Hók, J. and Minár, J., 2014b. Late Cretaceous-Cenozoic thermal evolution of the northern part of the Central Western Carpathians (Slovakia): Revealed by zircon and apatite fission track thermochronology. Tectonophysics, 615-616, 142-153.

Králiková, S., Vojtko, R., Sliva, L., Minár, J., Fuegenschuh, B., Kováč, M. and Hók, J., 2014c. Cretaceous-Quaternary tectonic evolution of the Tatra Mts (Western Carpathians): constraints from structural, sedimentary, geomorphological, and fission track data. Geologica Carpathica, 65(4), 307-326.

Krishnaswami, S., Mangini, A., Thomas, J., Sharma, P., Cochran, J., Turekian, K. and Parker, P., 1982. ^{10}Be and Th isotopes in manganese nodules and adjacent sediments: nodule growth histories and nuclide behavior. Earth and Planetary Science Letters, 59(2), 217-234.

Krumm, S., 1994. Centrifuge, Erlangen. http://www.ccp14.ac.uk/ccp/web-mirrors/krumm/html/software/winsoft.html.

Ku, T., Kusakabe, M., Measures, C., Southon, J., Cusimano, G., Vogel, J., Nelson, D. and Nakaya, S., 1990. Beryllium isotope distribution in the western North Atlantic: a

comparison to the Pacific. Deep Sea Research Part A. Oceanographic Research Papers, 37(5), 795-808.
Ku, T., Kusakabe, M., Nelson, D., Southern, J., Korteling, R., Vogel, J. and Nowikow, I., 1982. Constancy of oceanic deposition of ^{10}Be as recorded in manganese crusts. Nature, 299(5880), 240-242.
Kusakabe, M., Ku, T., Southon, J., Liu, S., Vogel, J., Nelson, D., Nakaya, S. and Cusimano, G., 1991. Be isotopes in rivers/estuaries and their oceanic budgets. Earth and Planetary Science Letters, 102(3-4), 265-276.
Kusakabe, M., Ku, T., Southon, J., Vogel, J., Nelson, D., Measures, C. and Nozaki, Y., 1987. Distribution of ^{10}Be and ^{9}Be in the Pacific Ocean. Earth and Planetary Science Letters, 82(3-4), 231-240.
Lachner, J., Christl, M., Synal, H.-A., Frank, M. and Jakobsson, M., 2013. Carrier free ^{10}Be/^{9}Be measurements with low-energy AMS: Determination of sedimentation rates in the Arctic Ocean. Nuclear Instruments and Methods in Physics Research Section B: Beam Interactions with Materials and Atoms, 294, 67-71.
Langereis, G., Krijgsman, W., Muttoni, G. and Menning, M., 2010. Magnetostratigraphy-concepts, definitions, and applications. Newsletters on Stratigraphy, 43(3), 207-233.
Lebatard, A.-E., Bourlès, D.L., Braucher, R., Arnold, M., Duringer, P., Jolivet, M., Moussa, A., Deschamps, P., Roquin, C. and Carcaillet, J., 2010. Application of the authigenic ^{10}Be/^{9}Be dating method to continental sediments: reconstruction of the Mio-Pleistocene sedimentary sequence in the early hominid fossiliferous areas of the northern Chad Basin. Earth and Planetary Science Letters, 297(1-2), 57-70.
Lebatard, A.-E., Bourlès, D.L., Duringer, P., Jolivet, M., Braucher, R., Carcaillet, J., Schuster, M., Arnaud, N., Monié, P. and Lihoreau, F., 2008. Cosmogenic nuclide dating of Sahelanthropus tchadensis and Australopithecus bahrelghazali: Mio-Pliocene hominids from Chad. Proceedings of the National Academy of Sciences, 105(9), 3226-3231.
Leclair, S.F. and Bridge, J.S., 2001. Quantitative interpretation of sedimentary structures formed by river dunes. Journal of Sedimentary Research, 71(5), 713-716.
Lexa, J., Halouzka, R., Havrila, M., Hanzel, V., Kubeš, P., Liščák, P. and Hojstričová, V., 1998. Explanatory notes to the geological map of the Kremnické Vrchy Hills, scale 1 : 50 000. State Geological Institute of Dionýz Štúr, Bratiaslava, 308 pp.
Longhitano, S.G., 2008. Sedimentary facies and sequence stratigraphy of coarse-grained Gilbert-type deltas within the Pliocene thrust-top Potenza Basin (Southern Apennines, Italy). Sedimentary Geology, 210(3–4), 87-110.
Lowe, D.R., 1976. Grain flow and grain flow deposits. Journal of Sedimentary Research, 46, 188-199.
Lukniš, M., 1962. Die Reliefentwicklung der Westkarpaten. Wissenschaftliche Zeitschrift der Martin–Luther–Universit¨at Halle–Wittenberg. Mathematik–Naturwissenschaften, 11, 1235-1244.
Magyar, I., 2021. Chronostratigraphy of clinothem-filled non-marine basins: Dating the Pannonian Stage. Global and Planetary Change, 205, 103609.
Magyar, I., Radivojevic, D., Sztano, O., Synak, R., Ujszaszi, K. and Pocsik, M., 2013. Progradation of the paleo-Danube shelf margin across the Pannonian Basin during the Late Miocene and Early Pliocene. Global and Planetary Change, 103, 168-173.
Magyar, I., Sztanó, O., Sebe, K., Katona, L., Csoma, V., Görög, Á., Tóth, E., Szuromi-Korecz, A., Šujan, M., Braucher, R., Ruszkiczay-Rüdiger, Z., Koroknai, B., Wórum, G., Sant, K., Kelder, N. and Krijgsman, W., 2019. Towards a high-resolution chronostratigraphy and geochronology for the Pannonian stage: Significance of the Paks cores (central Pannonian basin). Foldtani Kozlony, 149(3-4), 351-370.

Manville, V. and White, J.D.L., 2003. Incipient granular mass flows at the base of sediment-laden floods, and the roles of flow competence and flow capacity in the deposition of stratified bouldery sands. Sedimentary Geology, 155(1), 157-173.
Martini, I., Ambrosetti, E. and Sandrelli, F., 2017. The role of sediment supply in large-scale stratigraphic architecture of ancient Gilbert-type deltas (Pliocene Siena-Radicofani Basin, Italy). Sedimentary Geology, 350, 23-41.
Márton, E., Pipík, R., Starek, D., Kovács, E., Vidhya, M., Świerczewska, A., Tokarski, A.K., Vojtko, R. and Schlögl, S., 2022. Enhancing the reliability of the magnetostratigraphic age assignment of azimuthally nonoriented drill cores by the integrated application of palaeomagnetic analysis, field tests, anisotropy of magnetic susceptibility, and the evolution of the endemic fauna as documented on the upper Miocene limnic deposits of the Turiec Basin (Western Carpathians). AAPG Bulletin, 106(4), 803-827.
Matenco, L., Munteanu, I., ter Borgh, M., Stanica, A., Tilita, M., Lericolais, G., Dinu, C. and Oaie, G., 2016. The interplay between tectonics, sediment dynamics and gateways evolution in the Danube system from the Pannonian Basin to the western Black Sea. Science of The Total Environment, 543, 807-827.
Matenco, L.C. and Haq, B.U., 2020. Multi-scale depositional successions in tectonic settings. Earth-Science Reviews, 200, 102991.
Mazúr, E., 1963. Žilinská Kotlina Basin and Adjacent Mountains. Vydavateľstvo SAV, Bratislava.
McConnico, T.S. and Bassett, K.N., 2007. Gravelly Gilbert-type fan delta on the Conway Coast, New Zealand: Foreset depositional processes and clast imbrications. Sedimentary Geology, 198(3), 147-166.
McLennan, S.M., 1993. Weathering and global denudation. Journal of Geology, 101(2), 295-303.
McLennan, S.M., 2001. Relationships between the trace element composition of sedimentary rocks and upper continental crust. Geochemistry, Geophysics, Geosystems, 2(4).
Measures, C. and Edmond, J., 1982. Beryllium in the water column of the central North Pacific. Nature, 297(5861), 51-53.
Measures, C. and Edmond, J., 1983. The geochemical cycle of ^{9}Be: A reconnaissance. Earth and Planetary Science Letters, 66, 101-110.
Measures, C., Ku, T., Luo, S., Southon, J., Xu, X. and Kusakabe, M., 1996. The distribution of ^{10}Be and ^{9}Be in the South Atlantic. Deep Sea Research Part I: Oceanographic Research Papers, 43(7), 987-1009.
Merchel, S., Beutner, S., Opel, T., Rugel, G., Scharf, A., Tiessen, C., Weiß, S. and Wetterich, S., 2019. Attempts to understand potential deficiencies in chemical procedures for AMS. Nuclear Instruments and Methods in Physics Research Section B: Beam Interactions with Materials and Atoms, 456, 186-192.
Merchel, S., Braucher, R., Lachner, J. and Rugel, G., 2021. Which is the best ^{9}Be carrier for ^{10}Be/^{9}Be accelerator mass spectrometry? MethodsX, 8, 101486.
Merchel, S. and Herpers, U., 1999. An update on radiochemical separation techniques for the determination of long-lived radionuclides via accelerator mass spectrometry. Radiochimica acta, 84(4), 215-220.
Miall, A.D., 2006. The geology of fluvial deposits: Sedimentary facies, basin analysis, and petroleum geology. Springier, Berlin, 582 pp.
Minár, J., 2003. Midmountain level in the West Carpathians as tectoplain: outline of the work hypothesis. Geografický Časopis, 55(2), 141-158 (in Slovak).
Minár, J., Bielik, M., Kováč, M., Plašienka, D., Barka, I., Stankoviansky, M. and Zeyen, H., 2011. New morphostructural subdivision of the Western Carpathians: An approach

integrating geodynamics into targeted morphometric analysis. Tectonophysics, 502(1–2), 158-174.
Minár, J. and Bizubová, M., 1994. Georelief evolution in southern part of Turčianska kotlina (Basin). Acta Facultatis Rerum Naturalium Universitatis Comenianae, Geographica, 35, 25-33 (in Slovak).
Moore, D.M. and Reynolds, R.C., 1997. X-ray diffraction and the identification and analysis of clay Minerals. Oxford University Press, Oxford, 1-378.
Mulder, T. and Alexander, J., 2001. The physical character of subaqueous sedimentary density flow and their deposits. Sedimentology, 48(2), 269-299.
Mulder, T., Syvitski, J.P.M., Migeon, S., Faugeres, J.C. and Savoye, B., 2003. Marine hyperpycnal flows: initiation, behavior and related deposits. A review. Marine and Petroleum Geology, 20(6-8), 861-882.
Nemčok, M. and Lexa, J., 1990. Evolution of the basin and range structure around the Žiar mountain range. Geologica Carpathica, 41, 229-258.
Nemec, W. and Kazanci, N., 1999. Quaternary colluvium in west-central Anatolia: sedimentary facies and palaeoclimatic significance. Sedimentology, 46(1), 139-170.
Nemec, W. and Postma, G., 1993. Quaternary alluvial fans in southwestern Crete: sedimentation processes and geomorphic evolution. Alluvial sedimentation, 235-276.
Nemec, W. and Steel, R.J., 1984. Alluvial and coastal conglomerates: their signifcant features and some comments on gravelly mass flow deposits. In: E.H. Koster and R.J. Steel (Eds.), Sedimentology of Gravels and Conglomerates. Memories of the Canadian Society of Petroleum Geologists, pp. 1-30.
Nesbitt, H.W. and Young, G.M., 1982. Early proterozoic climates and plate motions inferred from major element chemistry of lutites. Nature, 299(5885), 715-717.
Neubauer, T.A., Harzhauser, M. and Pipík, R., 2015. Upper Miocene endemic lacustrine gastropod fauna of the Turiec Basin: Addressing taxonomic, paleobiogeographic and stratigraphic issues. Geologica Carpathica, 66(2), 139-156.
North, C.P. and Davidson, S.K., 2012. Unconfined alluvial flow processes: Recognition and interpretation of their deposits, and the significance for palaeogeographic reconstruction. Earth-Science Reviews, 111(1), 199-223.
Novello, A., Lebatard, A.E., Moussa, A., Barboni, D., Sylvestre, F., Bourlès, D.L., Paillès, C., Buchet, G., Decarreau, A., Duringer, P., Ghienne, J.F., Maley, J., Mazur, J.C., Roquin, C., Schuster, M. and Vignaud, P., 2015. Diatom, phytolith, and pollen records from a 10 Be/ 9 Be dated lacustrine succession in the chad basin: Insight on the miocene-pliocene paleoenvironmental changes in Central Africa. Palaeogeography, Palaeoclimatology, Palaeoecology, 430, 85-103.
Ognjanova-Rumenova, N. and Pipík, R., 2015. Stratigraphic and taxonomic significance of siliceous microfossils collected from the Turiec Basin, Western Carpathians (Slovakia). Acta Botanica Croatica, 74, 345–361.
Olariu, C., Steel, R.J. and Petter, A.L., 2010. Delta-front hyperpycnal bed geometry and implications for reservoir modeling: Cretaceous Panther Tongue delta, Book Cliffs, Utah. Aapg Bulletin, 94(6), 819-845.
Paknia, M., Ballato, P., Heidarzadeh, G., Cifelli, F., Hassanzadeh, J., Vezzoli, G., Mirzaie Ataabadi, M., Ghassemi, M.R. and Mattei, M., 2021. Neogene Tectono-Stratigraphic Evolution of the Intermontane Tarom Basin: Insights Into Basin Filling and Plateau Building Processes Along the Northern Margin of the Iranian Plateau (Arabia-Eurasia Collision Zone). Tectonics, 40(3).
PANalytical, B.V., 2016. X-Pert High Score Plus Software, The Netherlands.
Paola, C., 2016. A Mind of Their Own: Recent Advances in Autogenic Dynamics in Rivers and Deltas. In: D.A. Budd, E.A. Hajek and S.J. Purkis (Eds.), Autogenic Dynamics and Self-

Organization in Sedimentary Systems. SEPM Society for Sedimentary Geology, pp. 5-17.
Paseban, E., Khodabakhsh, S., Gharibreza, M., Bahiraei, N., Maleki, M. and HosseiniAsgarabadi, Z., 2018. A sedimentary model of mountainous rivers with application to Alamutrud and Shahrud rivers, N Qazvin, Iran. Arabian Journal of Geosciences, 11(24), 788.
Patruno, S. and Helland-Hansen, W., 2018. Clinoforms and clinoform systems: Review and dynamic classification scheme for shorelines, subaqueous deltas, shelf edges and continental margins. Earth-Science Reviews, 185, 202-233.
Pécskay, Z., Lexa, J., Szakács, A., Seghedi, I., Balogh, K., Konečný, V., Zelenka, T., Kovacs, M., Póka, T., Fülöp, A., Márton, E., Panaiotu, C. and Cvetković, V., 2006. Geochronology of Neogene magmatism in the Carpathian arc and intra-Carpathian area. Geologica Carpathica, 57(6), 511-530.
Pierson, T.C., 2005. Distinguishing between debris flows and floods from field evidence in small watersheds. US Geological Survey, Fact Sheet 2004-3142, DOI: 10.3133/fs20043142.
Pierson, T.C. and Costa, J.E., 1987. A rheologic classification of subaerial sediment-water flows. In: J.E. Costa and G.F. Wieczorek (Eds.), Debris Flows/Avalanches: Process, Recognition, and Mitigation. Reviews in Engineering Geology. Geological Society of America, pp. 1-12.
Pipík, R., 2002. Ostracod fauna of the Blažovce and Martin Formations (Turiec Basin). Mineralia Slovaca, 34, 105-112 (in Slovak with English abstract).
Pipík, R., 2004. Freshwater ostracods (Ostracoda) and Upper Miocene paleobiotopes of the northern part of the Turiec Depression (Slovakia). Mineralia Slovaca, 87-100 (in Slovak with English abstract).
Pipík, R., 2005. Upper Miocene freshwater ostracods (Ostracoda) of the littoral deposits of the Turiec Formation). Mineralia Slovaca, 37, 27-40.
Pipík, R. and Bodergat, A.-M., 2007. Candoninae trapézoïdales (Crustacea, Ostracoda) du Bassin de Turiec (Slovaquie) du Miocène supérieur : systématique, écologie et évolution. Geobios, 40(5), 645-676.
Pipík, R., Bodergat, A.M., Briot, D., Kováč, M., Král, J. and Zielinski, G., 2012. Physical and biological properties of the late Miocene, long-lived Turiec Basin, Western Carpathians (Slovakia) and its paleobiotopes. Journal of Paleolimnology, 47(2), 233-249.
Plašienka, D., 2003. Development of basement-involved fold and thrust structures exemplified by the Tatric–Fatric–Veporic nappe system of the Western Carpathians (Slovakia). Geodinamica Acta, 16(1), 21-38.
Plašienka, D., 2018. Continuity and Episodicity in the Early Alpine Tectonic Evolution of the Western Carpathians: How Large-Scale Processes Are Expressed by the Orogenic Architecture and Rock Record Data. Tectonics, 37(7), 2029-2079.
Plašienka, D., Grecula, P., Putiš, M., Kováč, M. and Hovorka, D., 1997. Evolution and structure of the Western Carpathians: an overview. Geological evolution of the Western Carpathians, 1-24.
Plink-Björklund, P., 2021. Distributive Fluvial Systems: Fluvial and Alluvial Fans. In: D. Alderton and S.A. Elias (Eds.), Encyclopedia of Geology (Second Edition). Academic Press, Oxford, pp. 745-758.
Postma, G., 1984. Slumps and their deposits in fan delta front and slope. Geology, 12(1), 27-30.
Postma, G. and Cartigny, M.J.B., 2014. Supercritical and subcritical turbidity currents and their deposits - A synthesis. Geology, 42(11), 987-990.

Potter, P.E., Maynard, J. and Pryor, W.A., 1980. Sedimentology of Shale. Springer Verlag, New York.
Potter, P.E., Maynard, J.B. and Depetris, P.J., 2005. Mud and Mudstones: Introduction and Overview. Springer Verlag, New York.
Pulišová, Z. and Hók, J., 2015. The palaeostress analysis of the fault rupture of the Žiarska kotlina Basin. Acta Geologica Slovaca, 7(2), 103-111.
Raisbeck, G., Yiou, F., Fruneau, M., Loiseaux, J., Lieuvin, M. and Ravel, J., 1981. Cosmogenic $^{10}Be/^{7}Be$ as a probe of atmospheric transport processes. Geophysical Research Letters, 8(9), 1015-1018.
Raiswell, R. and Berner, R.A., 1986. Pyrite and organic matter in Phanerozoic normal marine shales. Geochimica et Cosmochimica Acta, 50, 1967-1976.
Ratschbacher, L., Frisch, W., Linzer, H.G. and Merle, O., 1991. Lateral extrusion in the eastern Alps, PArt 2: Structural analysis. Tectonics, 10(2), 257-271.
Ruszkiczay-Rüdiger, Z., Balázs, A., Csillag, G., Drijkoningen, G. and Fodor, L., 2020. Uplift of the Transdanubian Range, Pannonian Basin: How fast and why? Global and Planetary Change, 192, 103263.
Ruszkiczay-Rüdiger, Z., Fodor, L.I. and Horváth, E., 2007. Neotectonics and Quaternary landscape evolution of the Gödöllő Hills, Central Pannonian Basin, Hungary. Global and Planetary Change, 58(1–4), 181-196.
Sharma, P., Mahannah, R., Moore, W., Ku, T. and Southon, J., 1987. Transport of ^{10}Be and ^{9}Be in the ocean. Earth and Planetary Science Letters, 86(1), 69-76.
Sharma, P. and Somayajulu, B., 1982. ^{10}Be dating of large manganese nodules from world oceans. Earth and Planetary Science Letters, 59(2), 235-244.
Schildgen, T.F., Robinson, R.A.J., Savi, S., Phillips, W.M., Spencer, J.Q.G., Bookhagen, B., Scherler, D., Tofelde, S., Alonso, R.N., Kubik, P.W., Binnie, S.A. and Strecker, M.R., 2016. Landscape response to late Pleistocene climate change in NW Argentina: Sediment flux modulated by basin geometry and connectivity. Journal of Geophysical Research: Earth Surface, 121(2), 392-414.
Schmid, S.M., Bernoulli, D., Fügenschuh, B., Matenco, L., Schefer, S., Schuster, R., Tischler, M. and Ustaszewski, K., 2008. The Alpine-Carpathian-Dinaridic orogenic system: Correlation and evolution of tectonic units. Swiss Journal of Geosciences, 101(1), 139-183.
Simon, Q., Ledru, M.P., Sawakuchi, A.O., Favier, C., Mineli, T.D., Grohmann, C.H., Guedes, M., Bard, E., Thouveny, N., Garcia, M., Tachikawa, K. and Rodríguez-Zorro, P.A., 2020. Chronostratigraphy of a 1.5±0.1 Ma composite sedimentary record from Colônia basin (SE Brazil): Bayesian modeling based on paleomagnetic, authigenic $^{10}Be/^{9}Be$, radiocarbon and luminescence dating. Quaternary Geochronology, 58.
Sládek, J., Vitovič, L., Holec, J. and Hók, J., 2022. Results of the Morphotectonics and Fluvial Activity of Intramountain Basins: The Turčianska Kotlina and Žiarska Kotlina Basins, World Geomorphological Landscapes, pp. 207-233.
Sobel, E.R., Hilley, G.E. and Strecker, M.R., 2003. Formation of internally drained contractional basins by aridity-limited bedrock incision. Journal of Geophysical Research: Solid Earth, 108(7), 6-23.
Spencer, C.J., Yakymchuk, C. and Ghaznavi, M., 2017. Visualising data distributions with kernel density estimation and reduced chi-squared statistic. Geoscience Frontiers, 8(6), 1247-1252.
Starkey, H.C., Blackmon, P.D. and Hauff, P.L., 1984. The Routine Mineralogical Analysis of Clay-Bearing Samples. U. S. Geological Survey Bulletin 1563, 1-31.
Stow, D.A., 2005. Sedimentary Rocks in the Field. A Colour Guide. Manson Publishing, London, 320 pp.

Streit, R.L., Burbank, D.W., Strecker, M.R., Alonso, R.N., Cottle, J.M. and Kylander-Clark, A.R.C., 2017. Controls on intermontane basin filling, isolation and incision on the margin of the Puna Plateau, NW Argentina (~23°S). Basin Research, 29, 131-155.

Šujan, M., 2021. Klastická sedimentológia: procesy ukladania a analýza fácií. Univerzita Komenského v Bratislave, Bratislava.

Šujan, M., Aherwar, K., Braucher, R., Šarinová, K., Chyba, A., Lalinská-Voleková, B. and Vojtko, R., 2022. Data for granulometric, geochemical and authigenic $^{10}Be/^{9}Be$ geochronological analysis of Upper Miocene outcrops in the Turiec Basin, Western Carpathians (Central Europe). Mendeley Data, doi: 10.17632/sdvpm9mf6m.

Šujan, M., Aherwar, K., Vojtko, R., Braucher, R., Šarinová, K., Chyba, A., Hók, J., Grizelj, A., Kyška-Pipík, R., Voleková, B., Rózsová, B. and AsterTeam, submitted. Stratigraphic, sedimentological, geochemical, mineralogical and geochronological data characterizing the Upper Miocene sequence of the Turiec Basin, Western Carpathians (Central Europe). Data in Brief.

Šujan, M., Braucher, R. and ASTER, T., 2018. A test of reproducibility of authigenic beryllium extraction from clay sediment in the facility of the Dept. of Geology and Palaeontology, Comenius University in Bratislava (Slovakia). Acta Geologica Slovaca, 10(2), 165-169.

Šujan, M., Braucher, R., Chyba, A., Vlačiky, M., Aherwar, K., Rózsová, B., Fordinál, K., Maglay, J., Nagy, A., Moravcová, M. and AsterTeam, 2023. Mud redeposition during river incision as a factor affecting authigenic $^{10}Be/^{9}Be$ dating: Early Pleistocene large mammal fossil-bearing site Nová Vieska, eastern Danube Basin. Journal of Quaternary Science, https://doi.org/10.1002/jqs.3482.

Šujan, M., Braucher, R., Kováč, M., Bourlès, D.L., Rybár, S., Guillou, V. and Hudáčková, N., 2016. Application of the authigenic $^{10}Be/^{9}Be$ dating method to Late Miocene–Pliocene sequences in the northern Danube Basin (Pannonian Basin System): Confirmation of heterochronous evolution of sedimentary environments. Global and Planetary Change, 137, 35-53.

Šujan, M., Braucher, R., Tibenský, M., Fordinál, K., Rybár, S. and Kováč, M., 2020. Effects of spatially variable accommodation rate on channel belt distribution in an alluvial sequence: Authigenic $^{10}Be/^{9}Be$-based Bayesian age-depth models applied to the upper Miocene Volkovce Fm. (northern Pannonian Basin System, Slovakia). Sedimentary Geology, 397.

Šujan, M., Fordinál, K., Šarinová, K., Rybár, S. and Pelech, O., 2021a. Upper Miocene colluvial and alluvial fan deposits of the Modrová Mb.: A window to palaeogeography of the Považský Inovec Mts. (Western Carpathians). Acta Geologica Slovaca, 13(1), 27-47.

Šujan, M., Kováč, M., Hók, J., Šujan, M., Braucher, R., Rybár, S. and de Leeuw, A., 2017. Late Miocene fluvial distributary system in the northern Danube Basin (Pannonian Basin System): Depositional processes, stratigraphic architecture and controlling factors of the Piešťany Member (Volkovce Formation). Geological Quarterly, 61(3), 521-548.

Šujan, M., Rybár, S., Kováč, M., Bielik, M., Majcin, D., Minár, J., Plašienka, D., Nováková, P. and Kotulová, J., 2021b. The polyphase rifting and inversion of the Danube Basin revised. Global and Planetary Change, 196, 103375.

Talling, P.J., Masson, D.G., Sumner, E.J. and Malgesini, G., 2012. Subaqueous sediment density flows: Depositional processes and deposit types. Sedimentology, 59(7), 1937-2003.

Tan, S.H. and Horlick, G., 1987. Matrix-effect observations in inductively coupled plasma mass spectrometry. Journal of Analytical Atomic Spectrometry, 2(8), 745-763.

Tari, G., Arbouille, D., Schléder, Z. and Tóth, T., 2020. Inversion tectonics: A brief petroleum industry perspective. Solid Earth, 11(5), 1865-1889.

Trexler, J., Cashman, P. and Cosca, M., 2012. Constraints on the history and topography of the northeastern Sierra Nevada from a Neogene sedimentary basin in the Reno-Verdi area, Western Nevada. Geosphere, 8(3), 548-561.

Tsai, H., Maejima, Y. and Hseu, Z.-Y., 2008. Meteoric ^{10}Be dating of highly weathered soils from fluvial terraces in Taiwan. Quaternary International, 188(1), 185-196.

Uhrin, A., Magyar, I. and Sztanó, O., 2009. Control of the Late Neogene (Pannonian s.l.) sedimentation by basement deformation in the Zala Basin. Foldtani Kozlony, 139(3), 273-282.

Utescher, T., Erdei, B., Hably, L. and Mosbrugger, V., 2017. Late Miocene vegetation of the Pannonian Basin. Palaeogeography, Palaeoclimatology, Palaeoecology, 467, 131-148.

van Dam, J.A., 2006. Geographic and temporal patterns in the late Neogene (12–3 Ma) aridification of Europe: The use of small mammals as paleoprecipitation proxies. Palaeogeography, Palaeoclimatology, Palaeoecology, 238(1–4), 190-218.

Van Dijk, M., Postma, G. and Kleinhans, M.G., 2009. Autocyclic behaviour of fan deltas: an analogue experimental study. Sedimentology, 56(5), 1569-1589.

Van Dine, D.F., 1985. Debris flows and debris torrents in the Southern Canadian Cordillera. Canadian Geotechnical Journal, 22(1), 44-68.

von Blanckenburg, F. and Bouchez, J., 2014. River fluxes to the sea from the ocean's ^{10}Be/^{9}Be ratio. Earth and Planetary Science Letters, 387, 34-43.

von Blanckenburg, F., O'nions, R., Belshaw, N., Gibb, A. and Hein, J., 1996. Global distribution of beryllium isotopes in deep ocean water as derived from Fe-Mn crusts. Earth and Planetary Science Letters, 141(1-4), 213-226.

Wei, W. and Algeo, T.J., 2020. Elemental proxies for paleosalinity analysis of ancient shales and mudrocks. Geochimica et Cosmochimica Acta, 287, 341-366.

Willenbring, J.K. and von Blanckenburg, F., 2010. Meteoric cosmogenic Beryllium-10 adsorbed to river sediment and soil: Applications for Earth-surface dynamics. Earth-Science Reviews, 98(1-2), 105-122.

Wittmann, H., von Blanckenburg, F., Bouchez, J., Dannhaus, N., Naumann, R., Christl, M. and Gaillardet, J., 2012. The dependence of meteoric ^{10}Be concentrations on particle size in Amazon River bed sediment and the extraction of reactive ^{10}Be/^{9}Be ratios. Chemical Geology, 318, 126-138.

Wysocka, A., Łoziński, M., Śmigielski, M., Czarniecka, U. and Bojanowski, M., 2018. New data on the age of the sedimentary infill of the Orava-Nowy targ basin - A case study of the Bystry stream succession (Middle/upper Miocene, Western Carpathians). Geological Quarterly, 62(2), 327-343.

Yawar, Z. and Schieber, J., 2017. On the origin of silt laminae in laminated shales. Sedimentary Geology, 360, 22-34.

Yokoyama, Y., Guichard, F., Reyss, J.-L. and Van, N.H., 1978. Oceanic residence times of dissolved beryllium and aluminum deduced from cosmogenic tracers ^{10}Be and ^{26}Al. Science, 201(4360), 1016-1017.

Zbořil, L., Šefara, J. and Halmešová, S., 1985. Geofyzikálny výskum Turčianskej kotliny, čiastková záverečná správa. Manuscript, Geofond Nr.: 60638, pp. 29 (in Slovak). Available online at: https://da.geology.sk/navigator/?desktop=Public.

Research Data

Click here to download Research Data
https://data.mendeley.com/datasets/sdvpm9mf6m/